

DEVELOPMENT OF NON-DESTRUCTIVE TECHNIQUE
TO DETECT CORROSION IN AUTOMOBILE TIRES

by

Omar AlChaar

Submitted in partial fulfilment of the requirements
for the degree of Master of Applied Sciences

at

Dalhousie University
Halifax, Nova Scotia
November 2021

© Copyright by Omar AlChaar, 2021

DEDICATED TO MY BELOVED PARENTS

TABLE OF CONTENT

TABLE OF CONTENT	iii
LIST OF TABLES.....	v
LIST OF FIGURES.....	vi
ABSTRACT	viii
LIST OF ABBREVIATIONS & SYMBOLS USED	ix
ACKNOWLEDGEMENTS	xi
CHAPTER 1 INTRODUCTION.....	1
1. BACKGROUND AND OBJECTIVES.....	1
CHAPTER 2 LITERATURE REVIEW	3
2.1. TIRES - OVERVIEW	3
2.1.1. BODY SECTION	4
2.1.2. TREAD SECTION	7
2.1.3. ASSEMBLING & CURING	7
2.1.4. END-PRODUCT INSPECTION	9
2.2. TIRE BEAD	10
2.2.1. BEAD WIRES.....	10
2.2.2. DESCRIPTION OF THE TIRE BEAD AND ITS COMPONENTS.....	10
2.2.3. DIFFERENT TYPES OF TIRE BEAD REINFORCEMENTS	10
2.2.4. TIRE BEAD FAILURE	12
2.2.5. CORROSION UNDER INSULATION.....	12
2.3. MECHANISM OF CORROSION UNDER INSULATION	13
2.4. STUDY CASE & OBJECTIVE	15
2.5. CORROSION INSPECTION	15
2.5.1. INFRARED THERMOGRAPHY	17
2.5.2. INDUCTION THERMOGRAPHY.....	20
2.5.3. THERMAL EMISSIVITY BACKGROUND.....	25
2.5.4. IMAGING SYSTEMS	27
2.5.5. CORROSION DETECTION & HEAT TRANSFER.....	29
2.6. THERMAL IMAGE PROCESSING	32

2.7. RECENT RELATED WORK.....	36
CHAPTER 3 METHODOLOGY.....	39
3.1. INFRARED IMAGE CALIBRATION.....	39
3.2. SAMPLES' DESIGN.....	43
3.3. EXPERIMENTAL PREPARATION.....	46
3.4. TESTING APPARATUSES.....	52
3.4.1. PLANAR INDUCTION COIL.....	52
3.4.2. HELMHOLTZ COILS.....	53
3.4.3. TESLA COILS.....	53
3.5. SYSTEM SETUP.....	54
CHAPTER 4 RESULTS AND DISCUSSION.....	55
4.1. PLANAR COIL.....	55
4.1.1. PILOTING RESULTS.....	55
4.1.2. SAMPLES' TESTING - HORIZONTAL DIRECTION.....	57
4.3. HELMHOLTZ COIL.....	61
4.4. TESLA COIL.....	62
4.4.1. THE ALGORITHM.....	62
4.4.2. TESTING USING TESLA COIL.....	64
4.4.3. DETECTION ON BARE WIRES.....	65
4.4.4. DETECTION ON EMBEDDED WIRES.....	68
4.4.5. DETECTION ON EMBEDDED TRINGLES.....	80
CHAPTER 5 CONCLUSION.....	83
5.1. CONCLUSIONS.....	83
5.2. RECOMMENDATIONS.....	84
5.3. FUTURE WORK.....	84
REFERENCES.....	86
APPENDIX B.....	90

LIST OF TABLES

TABLE 1: MAIN CHARACTERISTICS OF CORROSION MEASUREMENT TECHNIQUES	16
TABLE 2: BEAD WIRE CHEMICAL COMPOSITION.....	44
TABLE 3: RAW MATERIALS OF RUBBER COMPOUND	44
TABLE 4: CORROSION SEVERITY BETWEEN ZINC-ON AND ZINC-REMOVED SAMPLES	51
TABLE 5: OBJECT PARAMETERS, SETTING INSTRUCTION AND UNIT OF MEASUREMENT	63
TABLE 6: TESLA COIL SETUP PARAMETERS.....	64

LIST OF FIGURES

FIGURE 1: RADIAL TIRE MANUFACTURING PROCESS	4
FIGURE 2: CARCASS PLY MANUFACTURING PROCESS (1/2)	5
FIGURE 3: CARCASS PLY MANUFACTURING PROCESS (2/2)	6
FIGURE 4: TREAD SECTION MANUFACTURING PROCESS	7
FIGURE 5: CURING MOLD IN PROCESS	8
FIGURE 6: BEFORE AND AFTER TIRE CURING	8
FIGURE 7: STRUCTURE OF A TYPICAL RADIAL TIRE (MICHELINMAN.COM)	9
FIGURE 8: DIFFERENT TYPES OF TIRE BEAD REINFORCEMENTS (BURTON, 1954).....	11
FIGURE 9: CABLE BEAD- TRINGLE TRESSE (TT).....	11
FIGURE 10: LOCALIZED CORROSION SPOT ON BEAD STRAND	14
FIGURE 11: ILLUSTRATION OF PROTECTION DISTANCE (PD) DURING CATHODIC PROTECTION	14
FIGURE 12: CROSS SECTIONAL AREA OF TIRE BEAD	15
FIGURE 13: PRINCIPLE OF THE PASSIVE THERMOGRAPHY	18
FIGURE 14: PRINCIPLE OF THE ACTIVE THERMOGRAPHY	18
FIGURE 15: CLASSIFICATION OF THERMOGRAPHY TESTING METHODS (IBARRA-CASTANEDO ET AL., 2009)	19
FIGURE 16: INDUCTION THERMOGRAPHY ELECTROMAGNETIC OPERATIONAL MODE	20
FIGURE 17: INDUCTION THERMOGRAPHY TYPICAL SETUP	21
FIGURE 18: CAUSE OF THE SKIN EFFECT (WIKIPEDIA).....	22
FIGURE 19: DISTRIBUTION OF CURRENT FLOW IN A CYLINDRICAL CONDUCTOR (WIKIPEDIA)	22
FIGURE 20: THERMAL CONDUCTIVITY PLOTTED AGAINST THERMAL DIFFUSIVITY.	24
FIGURE 21: CONVENTIONAL ECPT WITH DIFFERENT CONFIGURATIONS.	25
FIGURE 22: ECPT CONFIGURATIONS FOR UNIFORM HEATING.....	25
FIGURE 23: ELECTROMAGNETIC SPECTRUM.	26
FIGURE 24: GREYBODY SURFACE BEHAVIOR	28
FIGURE 25: CLASSICAL MODELS OF HEAT CONDUCTION IN SOLIDS	30
FIGURE 26: TEMPERATURE CONTRAST AND DERIVATIVES VARIATIONS FOR DIFFERENT THICKNESSES.	31
FIGURE 27: LINEAR SPATIAL FILTERING APPLICATION.	33
FIGURE 28: A) ORIGINAL IMAGE B) CORRESPONDENT HISTOGRAM C) ENHANCED IMAGE D) CORRESPONDENT HISTOGRAM	34
FIGURE 29: 1ST DERIVATIVE ON INTENSITY FUNCTIONS FOR 2 TYPES OF EDGES.....	35
FIGURE 30: FIRST AND SECOND DERIVATIVES OVER EDGE INTENSITY FUNCTION	36
FIGURE 31: TEMPERATURE PROFILE OF CORRODED REBAR AFTER 10 S. OF INDUCTIVE HEATING	37
FIGURE 32: (A) REBAR WITH LOCALIZED SIGNIFICANT (TOP), AND LIGHT CORROSION (BOTTOM). THERMAL IMAGE OF REBAR WITH (B) LIGHT CORROSION, AND (C) LOCALIZED CORROSION.....	38
FIGURE 33: FIRST SIMULATION FOR THE BASELINE SAMPLE	40
FIGURE 34: CALIBRATING SIMULATION: A) SMALL 45° B) LARGE 45° C) HORIZONTAL D) VERTICAL	40
FIGURE 35: CALIBRATION SIMULATION - CORRELATION COEFFICIENT	42
FIGURE 36: CALIBRATING SIMULATION: A) LAPLACIAN FILTER B) ROBERT’S FILTER	42
FIGURE 37: ISOMETRIC, TOP, FRONT, AND RIGHT SIDE FOR THE DESIGNED SAMPLE	43
FIGURE 38: ANIMATED SAMPLE TYPES.....	45
FIGURE 39: TRINGLE WIRES DIPPED IN WATER FOR VARIOUS PERIOD.....	46
FIGURE 41: FULL CORROSION PROCEDURE.....	46
FIGURE 42: FULL CORROSION PROCEDURE.....	47
FIGURE 43: PATTERN CORROSION PROCEDURE.....	48
FIGURE 44: LOWER SIDE STRIP OF GREEN RUBBER INSIDE THE JIG MOLD BEFORE CURING.....	49
FIGURE 45: SAMPLE TOP VIEW.....	49
FIGURE 46: SAMPLE SIDE VIEW.....	49

FIGURE 47: TIRE BEAD SAMPLE	50
FIGURE 48: SAMPLES FLOW CHART ACCORDING TO SHAPE AND CORROSION TYPE.....	50
FIGURE 49: PREPARED SAMPLES FOR TESTING.....	51
FIGURE 50: BEAD SECTION- WAVE SHAPE.....	51
FIGURE 51: PLANAR INDUCTION THERMOGRAPHY BASIC SETUP	52
FIGURE 52: HAND-MADE HELMHOLTZ INDUCTION COIL	53
FIGURE 53: SMITHERMA- IH 1000 TESLA INDUCTION COIL	54
FIGURE 54: PILOTING SAMPLES CATEGORIZED BASED ON TYPE AND SURFACE CONDITIONS.	55
FIGURE 55: THIN AND THICK BLACK PAINTED NAILS.	56
FIGURE 56: NAILS SURFACE TEMPERATURE AFTER BEING SUBJECTED TO ELECTROMAGNETIC WAVES.....	56
FIGURE 57: REFERENCE SAMPLE	57
FIGURE 58: PATTERN SAMPLE #5.....	58
FIGURE 59: PATTERN SAMPLE #6.....	58
FIGURE 60: PATTERN SAMPLE #7.....	59
FIGURE 61: PATTERN SAMPLE #8.....	59
FIGURE 62: SIDE 1- TOP WIRE VS BOTTOM WIRE.	60
FIGURE 63: 2M OF CORRODED CIRCUMFERENCE OF BEAD WIRE	61
FIGURE 64: CORROSION DETECTION USING HANDMADE HELMHOLTZ SETUP.....	61
FIGURE 65: AVERAGING THE ACQUISITION ASSOCIATED WITH 20 PRISTINE AREAS OF A BARE STEEL WIRE.....	66
FIGURE 66: TEMPERATURE EVOLUTION WITH RESPECT OF TIME FOR A BARE STEEL WIRE, FREE OF CORROSION: A) HEATING CYCLE #1; B) HEATING CYCLE #2.....	66
FIGURE 67: AVERAGING THE ACQUISITION ASSOCIATED WITH A PRISTINE AND ONE STEEL WIRE	67
FIGURE 68: TEMPERATURE EVOLUTION WITH RESPECT OF TIME FOR A MIX OF PRISTINE OF CORRODED AREAS OF A BARE STEEL WIRE, FREE OF CORROSION: A) HEATING CYCLE #1; B) HEATING CYCLE #2.....	67
FIGURE 69: THERMAL IMAGE SEQUENCE OF THE REFERENCE SAMPLE RIGHT AFTER HEATING A) RIGHT AFTER HEATING IS REMOVED, B	68
FIGURE 70: THERMAL IMAGE SEQUENCE OF THE REFERENCE SAMPLE IN COOLING MODE	69
FIGURE 71: RESPECTIVE COMPARATIVE POINTS OF TEMPERATURE: A) FRONT; B) BACK	70
FIGURE 72: AVERAGE TEMPERATURE	72
FIGURE 73: VARIANCE	72
FIGURE 74: SKEWNESS.....	73
FIGURE 75: KURTOSIS.....	73
FIGURE 76: CORRELATION COEFFICIENT ASSOCIATED WITH THE 40 ACQUISITION POINTS	74
FIGURE 77: THERMAL IMAGE OF SAMPLE 7 PROCESSED USING A SIMPLE TEMPERATURE ANALYZING ALGORITHM (A) RIGHT AFTER HEATING, (B) 100 S AFTER HEATING, (C) 300 S AFTER HEATING (CORRODED WIRE ON THE LEFT)	75
FIGURE 78: PROCESSING THE DATA USING THE PROPOSED ALGORITHM (CORRODED WIRE ON THE LEFT)	76
FIGURE 79: CORRELATION COEFFICIENT ASSOCIATED WITH THE ACQUISITION POINTS ON SAMPLE 7	77
FIGURE 79: THERMAL IMAGE OF SAMPLE 8 PROCESSED USING A SIMPLE TEMPERATURE ANALYZING ALGORITHM (A) RIGHT AFTER HEATING, (B) 100 S AFTER HEATING, (C) 300 S AFTER HEATING (CORRODED WIRE ON THE LEFT)	78
FIGURE 80: CORRELATION COEFFICIENT ASSOCIATED WITH THE ACQUISITION POINTS ON SAMPLE 8	79
FIGURE 81: PROCESSING THE DATA USING THE PROPOSED ALGORITHM (CORRODED WIRE ON THE LEFT)	79
FIGURE 82: EMBEDDED TRINGLE, CORRODED IN TAP WATER (A) RIGHT AFTER HEATING, (B) AFTER 500S COOLING PROCESSED WITH FLIR ALGORITHM, (C) RIGHT AFTER HEATING, (D) AFTER 500S COOLING PROCESSED BY THE IN-HOUSE ALGORITHM.	81
FIGURE 83: EMBEDDED TRINGLE, CORRODED IN SALINE SOLUTION (A) RIGHT AFTER HEATING, (B) AFTER 500S COOLING PROCESSED WITH FLIR ALGORITHM, (C) RIGHT AFTER HEATING, (D) AFTER 500S COOLING PROCESSED BY THE IN-HOUSE ALGORITHM.	82
FIGURE 84: MAGNETIC FIELD IN HELMHOLTZ SETUP.....	85

ABSTRACT

In the present work, various induction thermographic techniques have been tested to detect corrosion traces over embedded steel wire in cooked rubber (simulating bead wires condition in automobile tires).

Accordingly, samples have been created, and 3 types of induction coils have been used: Planar coil, Helmholtz coil and Tesla coil. Results showed that planar coil provided general distinguishment between corroded and pristine wire; however, it failed to show the location corrosion traces. Helmholtz failed to provide uniform heating maybe due to poor coils design. Finally, the Tesla coil showed the best performance in providing higher induction energy, more uniform heating, and more temperature difference between the pristine and corroded wire. However, results showed that using simple temperature analyzing algorithms cannot be relied upon to produce accurate results when in comes to located corrosion in metallic objects.

We also showed that depending on the complexity of the object being analyzed, the in-house algorithm gave promising results at pinpointing areas where corrosion occurred. In general, the correlation coefficient was a good indicator of where corrosion might be present. However, the algorithm produced some false positives when the object's geometry became more complex, or some precipitate might have formed. Nonetheless, the algorithm was able to show where corrosion occurred in most cases. More studies must be conducted to better optimize the image processing step and the amount of data acquired.

Key Words:

Tringles, Corrosion, Non-Destructive Testing, Induction Thermography, Image Processing

LIST OF ABBREVIATIONS & SYMBOLS USED

$\bar{\alpha}$	total absorbance (-)
α	thermal diffusivity (m ² /s)
ε	emissivity (-)
λ	the radiation wavelength (m)
μ	thermal diffusion length (m)
$\bar{\rho}$	total reflectance (-)
ρ	Density (kg/m ³)
$\bar{\sigma}$	Stefan-Boltzmann's constant = 5.67×10^8 (W/m ² K ⁴)
$\bar{\tau}$	total transmittance (-)
σ_e	electrical conductivity
μ_0	free space permeability
c	light speed (m/s),
d	defect depth (m)
e	thermal effusivity (Ws ^{1/2} /m ² K)
f	excitation wave frequency (Hz)
h	the Planck's constant (Js),
k	thermal conductivity (W/mK);
k_b	the Boltzmann constant (1.38×10^{-23} J/K),
t	time (s)
z	distance from the midpoint of the circular coils
C	specific heat (J/kg K).
D	defect diameter/lateral extension (J/kg K)
E	energy emitted from object (W/m ²)
F_o	Fourier number (-)
I	current intensity
L	material thickness (m)
N	number of loops,

Q	absorbed energy density (J/m ²)
R	bobbin diameter
T	temperature (K)
T_0	the initial (ambient) temperature,
T_{s-inf}	temperature evolution in the semi-infinite body,
obj	parameters related to object (greybody)
refl	parameters related to the object reflection
s	parameters related to sound area
tot	tot total parameter
ϕB	magnetic flux (weber)
CB	carbon black
ECPT	Eddy current pulsed thermography
EMF	electromotive force
IRT	Infrared thermography
NHSTA	National Highway Traffic Safety Administration
NDT	Non-destructive testing
TT	Tringle Tresse

ACKNOWLEDGEMENTS

I would like to express my feelings of gratitude to my supervisor Dr. George Jarjoura for his immense guidance and support throughout my Master's Program at Dalhousie University. Also, I would like to thank my supervisors at Michelin Group, Eng. Francis Babineau and Bob Milos for their support throughout my internship term. Finally, I would like to acknowledge the priceless support and tremendous patience of my family members during this research program.

This research study would not have been possible without the generous grant of MITACS (The Mathematics of Information Technology and Complex Systems) Canada.

Omar AlChaar

September 2021

CHAPTER 1

INTRODUCTION

1. BACKGROUND AND OBJECTIVES

Corrosion has always been a significant threat to the manufacturing industry and is responsible for countless dollars due to damaging and maintaining costs (Ahmad, 2006). Thus, steel-reinforced products are more susceptible to losing their property to withstand harsh operating environments when corrosion attacks their incorporated steel. One example in this context can be depicted in the transportation sector, where steel bead wires represent a fundamental component in manufacturing high-quality automobile radial tires. These wires are the crucial link through which the vehicle load is transferred from the rim to the tire through a firm hold/attach and high resistance against excessive pressure. Once these tringles get exposed to corrosion, the adhesion property will deteriorate; hence, the steel-rubber bond will break down and affect the tire's safety, strength, and durability. It is, therefore, essential to have access to a credible corrosion inspection apparatus that can detect early warning of corrosion signs. Such an apparatus can improve safety and quality measures as an ultimate goal. For this reason, the main objective of this research is to research and adjust an effective non-destructive testing (NDT) tool to detect any potential corrosion defect in the embedded tringles of automobile tires.

After being tried by the Michelin Group quality assurance team, the search for a suitable technique started with the assumption that X-ray and ultrasound techniques are not successful in detecting corrosion beneath the rubber. Hence, the two most promised techniques were Terahertz thermography and induction thermography. Terahertz thermography was adopted at first; however, after preparing a piece of vulcanized rubber to be tested using this technique, the results showed that the sample absorbed all the emitted energy without reflecting any radiation. These results agree with Hirakawa's (Hirakawa et al., 2020) recent paper on rubber

evaluation when it is condensed with carbon black material(CB), which has an extremely large apparent THz absorbance. Eventually, induction thermography was adopted as it holds a lot of promises, especially if a proper image processing algorithm is adopted.

In this context, Chapter 2 will start with an overview of the tire manufacturing process as an introduction to define the tire bead section and its related bead wire. After that, a corrosion mechanism under insulation will be proposed along with its inspection techniques, with a specific focus on induction thermography.

Chapter 3 will present the various experimental procedures that took place before starting the inspection trials, such as images calibration, samples' design and preparation. Finally, relevant equipment, system setup and operating conditions were presented.

Chapter 4 will present the results from the various inspection experiments along with their adjustment attempts. The chapter will offer the possible reasoning for the failure of some experiments and how the improvement took place.

Finally, Chapter 5 will present the final conclusions for the current study.

CHAPTER 2

LITERATURE REVIEW

2.1. TIRES - OVERVIEW

Historically, tires were made of leather and iron/steel mounted on wheels made of wood, which were used on carts and wagons. Later, the vulcanization process was invented by Charles Goodyear and Thomson in 1839 (Bertman,2005), which gave the mounted rubber on tires enough durability to survive road use. In 1847, Robert Thomson proposed the concept of pneumatic tires (US Patent No. 5104); however, it was never implemented and people kept using iron and wooden wheels (Du Cros, 1938). It was not until 1888 that the pneumatic tire gained popularity when John Dunlop produced the first tire with high efficiency in absorbing shocks from potholes and bumps.

In 1895, pneumatic tires made their debut in race tournaments, where they were skinny and tall but not efficient for heavier, larger, and more powerful vehicles. For this reason, treaded tires were introduced in 1905 to provide a stiffer and more durable outer edge. Furthermore, starting from the 1920s, Bayer's laboratories were working on producing synthetic rubber; however, it was until 1931 when Du Pont company produced the first synthetic rubber on an industrialized scale. (Carothers, 1931)

In 1946, Michelin company came up with the radial tire design that became later an industry standard for tire producers. This design relies on arranging the ply cords at a 90-degree angle with respect to the travel direction, increasing gas mileage, tread life span, and improving steering performance. Since then, radial tire technology has been the standard design for all automotive tires. Although other design methods have been adopted in the tire manufacturing industry, like bias tire (or cross ply) or belted bias tire (Gent and Walter, 2005). (Kovac and Rodgers, 1994), radial tires showed the best performance for longer tread life, fewer blowouts, better steering

control, and lower rolling resistance. A radial tire manufacturing process can be summarized by the assembly of 2 main complex components, Body and Tread, to form a “green tire” and cure it in a later stage (fig.1).

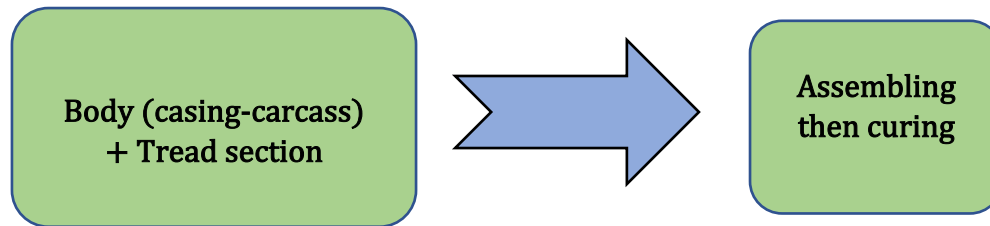


Figure 1: radial tire manufacturing process

2.1.1. BODY SECTION

Tires are manufactured on a rotating drum with an inflatable centre section (fig.2) (fig. 3), according to the following steps:

- The first layer applied to the drum is a sheet of airtight synthetic rubber called the inner liner and is used to seal the air (hold high-pressure air) inside the tire.
- In the second stage, additional plies can be added to reinforce the sidewalls, and a ply made of textile is added, this network of cables will form the reinforcement around the tire. It is the radial carcass.
- Two strips of profiled rubber then form a tight seat for the bead **bead wires** which are large steel cords wound together to form a cable or ribbon-type configuration. The casing plies are looped around the beads bundles to anchor and hold them in place.
- Another ply is then added to increase rigidity, followed by a rubber set of plies to protect bead wires from the toughening tools and reinforce sidewall from lateral damage.
- Finally, edges are wrapped around to further seal the middle hoops. The completed body carcass can be removed and taken to the second stage machine. This completes the inner part skeleton of the tire.

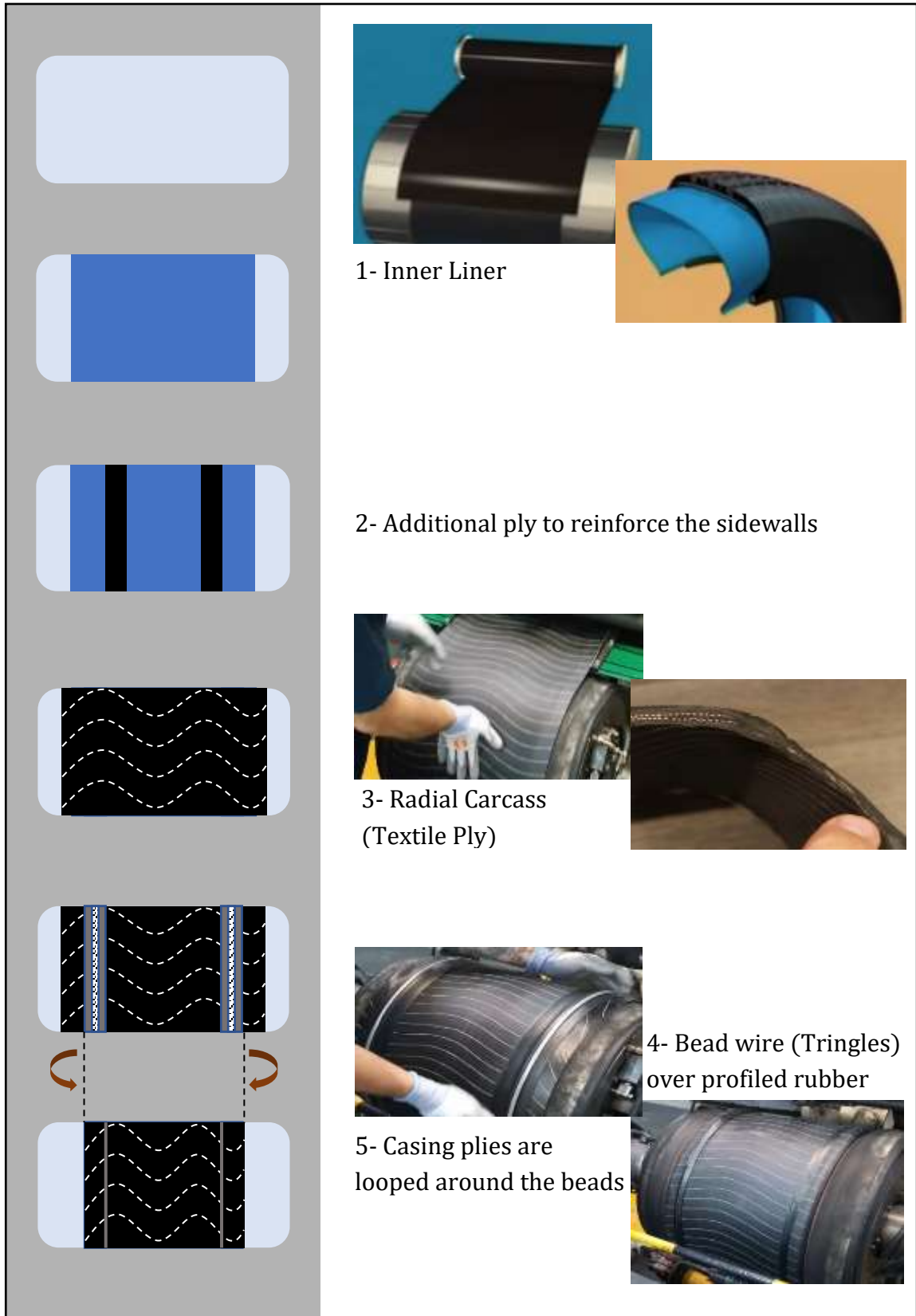


FIGURE 2: CARCASS PLY MANUFACTURING PROCESS (1/2)

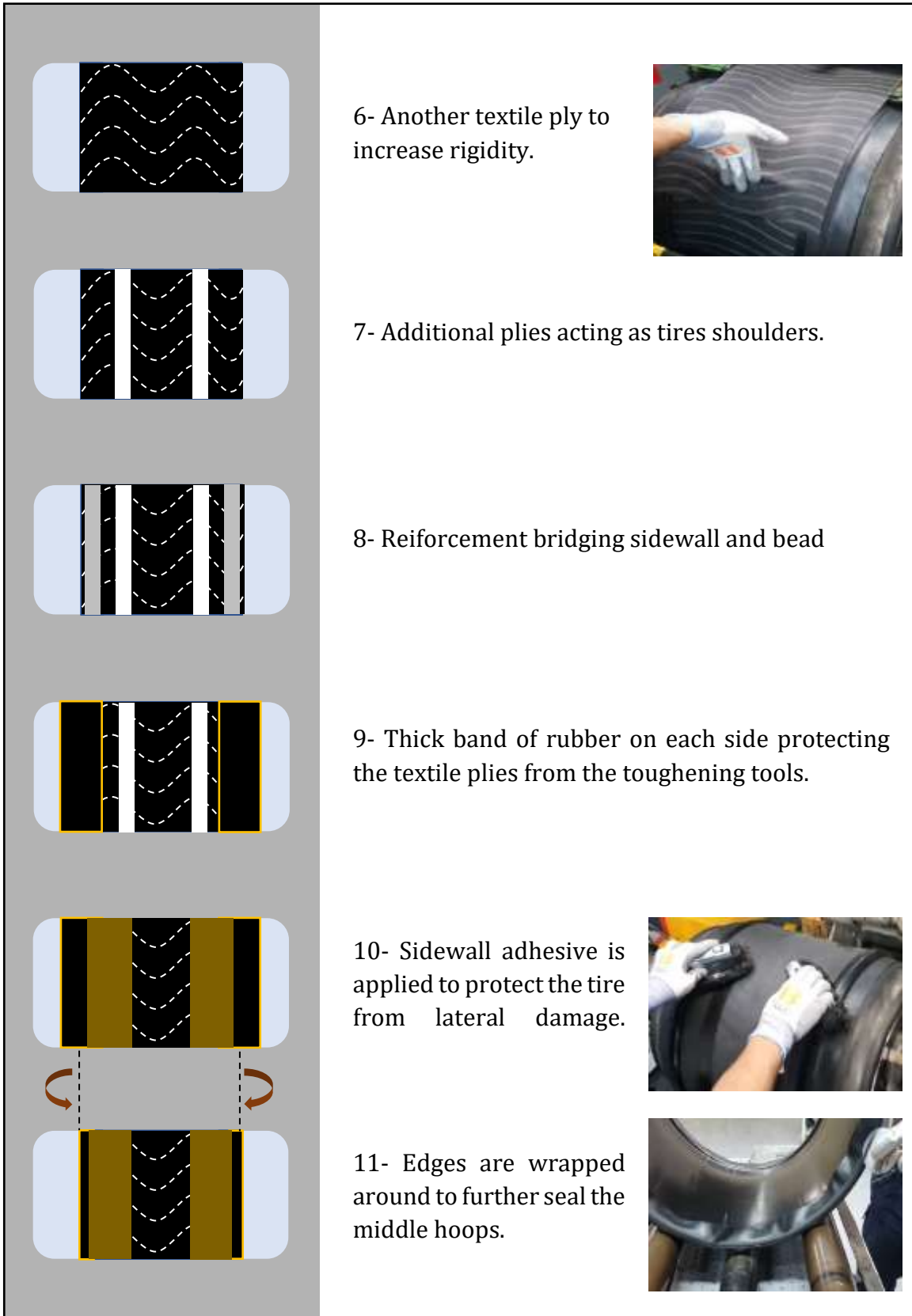


Figure 3: Carcass ply manufacturing process (2/2)

2.1.2. TREAD SECTION

The tread section is also done on a drum according to the following steps (fig.4):

- Two strips of rubber embedded with steel cords are wrapped obliquely against the drum. These are called belts, and they help make the tire relatively immune to punctures along with the optimum level of flatness.
- Next, narrow strips of rubber plie are added, the computerized system winds them with the right amount of tension.
- And finally, for the last layer, the tread rubber machinery applies it to the plie.



Figure 4: Tread section manufacturing process

2.1.3. ASSEMBLING & CURING

Assembling and curing are done according to the following steps

- A transfer ring collects the tread section and transfers it to the inner part.
- Compressed air inflates the tire to shape it, and all the layers stick together.
- The machine rolls the edge of the tread rubber over the sidewalls.

We now have what is known as a green tire, a non-cured tire without a tread pattern.

In the centre of the curing mould (fig. 5), a bladder is pressurized with steam at 170 °C, pushing the still malleable material into the tread parts and the recognizable sidewall markings; The heat from the steam surrounding the mould causes the curing to begin. This rise in temperature causes the vulcanization of the rubber, a chemical reaction that transforms it from a weakened sticky substance to one that is stronger and more elastic.

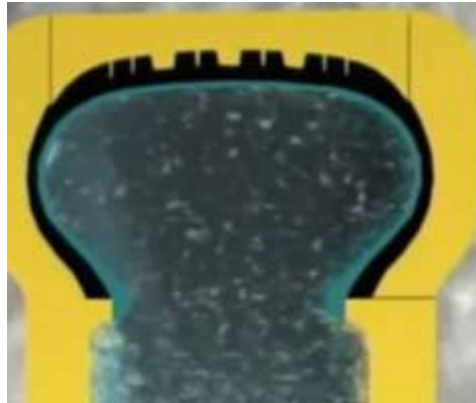


Figure 5: Curing mold in process.

The sulfur incorporated with the rubber compounds forms bonds between the polymer chains. At this point, the rubber switches from a plastic state to an elastic state and the tire acquires its final form and properties (fig. 6).

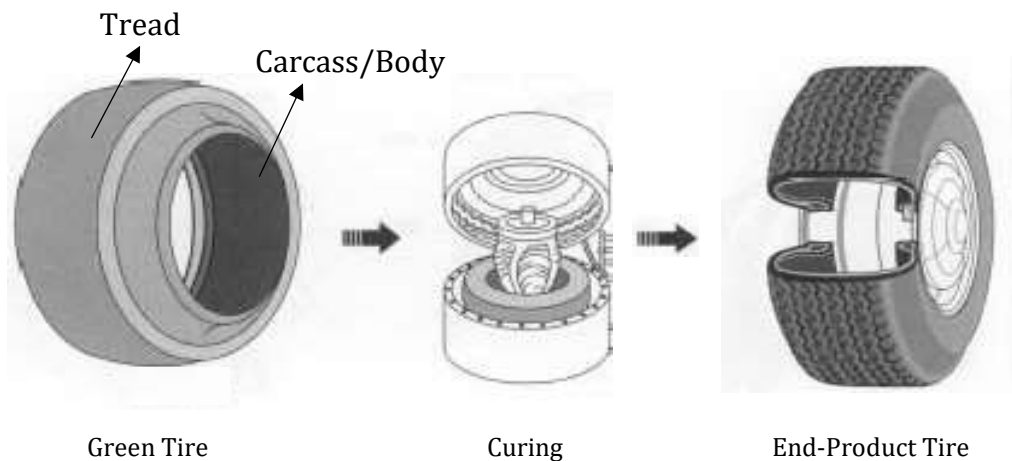


Figure 6: Before and After tire curing

2.1.4. END-PRODUCT INSPECTION

Quality assurance is the final stage in the manufacturing process. Here the product is inspected to ensure customer satisfaction. These checks include:

1. Buffing and trimming off mould flash from the tire.
2. Visual investigation of each tire for defects.
3. X-ray inspection for possible ply cord spacing and belt layup.
4. Statistical sampling to test uniformity, durability, and dynamic balancing. This testing includes many development tests reviewed earlier, such as conicity, radial runout, and lateral force variation(Kovac and Rodgers, 1994).

Although manufactured tires pass through a complex inspection process to ensure that they are meeting specific standards related to safety, quality, and performance, these inspections do not cover the detection of corrosion defects under rubber around the wire bead section.

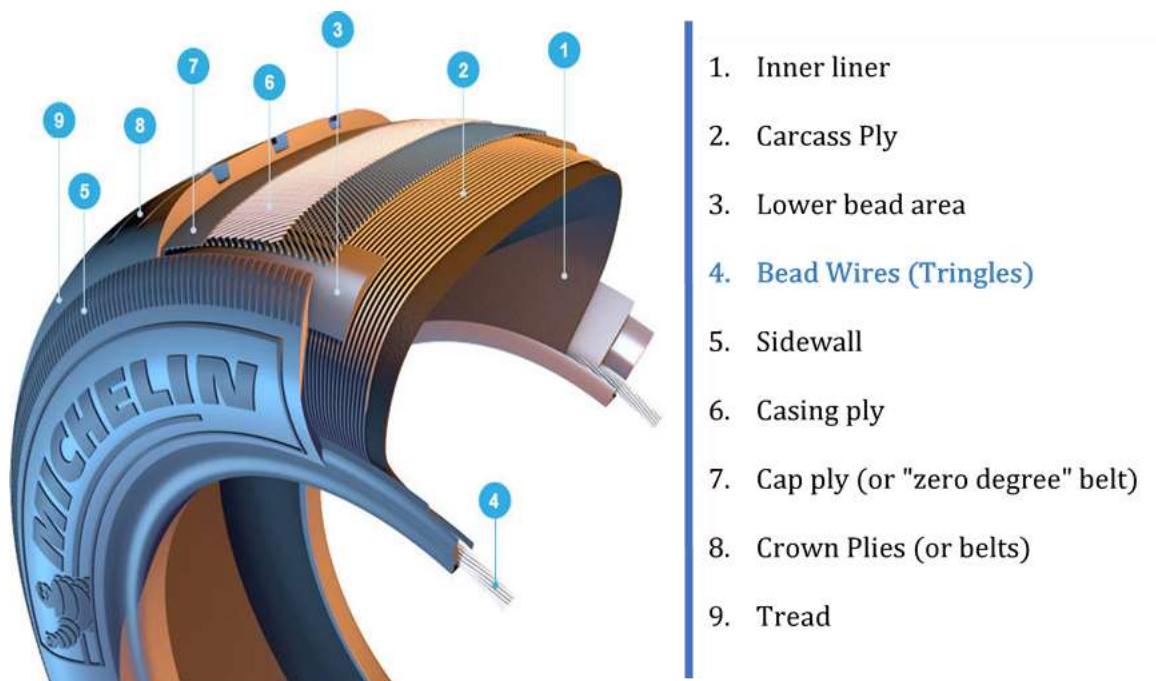


Figure 7: Structure of a typical radial tire (michelinman.com)

2.2. TIRE BEAD

2.2.1. BEAD WIRES

Bead wires play two significant roles. They are essential for a vehicle weight to be transferred from the rim to the tire and for various other forces (such as steering, traction, acceleration, braking, and directional forces) to be transferred from the tire to the rim. These wires are coated with special alloys of bronze, brass, or zinc to protect the steel from corrosion. During vulcanization, this coating and the sulfur in the rubber cross-link together to produce copper sulfide or zinc oxide, which improves the bead bonding to the rubber. Moreover, these beads prevent vibration during driving and significantly affect tires' safety, strength, and durability. Failure of the bead can lead to the separation of the inner tubeless part from the wheel, leading to deadly accidents.

2.2.2. DESCRIPTION OF THE TIRE BEAD AND ITS COMPONENTS

Based on The National Highway Traffic Safety Administration, an agency of the U.S. federal government (NHSTA) (Harris et al., 2013), a “bead” is described as part of the tire that includes all the materials below the sidewalls (fig. 7) in the rim contact area, including:

- Rubber components in the bead area.
- Bead bundle and rubber coating if present.
- The body ply and its turn-up, including the rubber coating.
- Rubber, fabric, or metallic bead reinforcing materials.
- The inner liner under the bead area.

2.2.3. DIFFERENT TYPES OF TIRE BEAD REINFORCEMENTS

Over time, various plies and materials were used to design practical bead reinforcement, and they are summarized in the following (fig. 8) (fig. 9):

- Weftless Bead: Parallel steel wires coated with rubber.
- Tape Bead: Parallel steel wires held in the form of a flat tape by a fine filler.
- Braid Bead: Parallel steel wire braided together to form a flat band.
- Single Wire Bead: A single wire covered with rubber.
- **Cable Bead- Tringle Tresse (TT) (Michelin Beads):** One or two strands of the steel wires are tightly intertwined around a flexible heavy cord called core, forming a cable bead

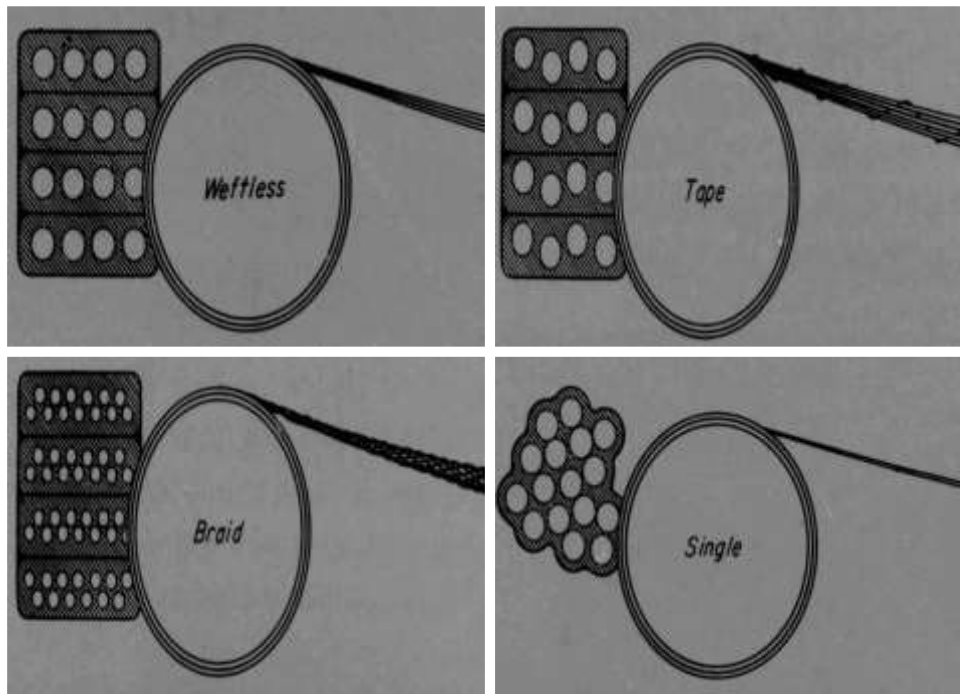


Figure 8: Different types of tire bead reinforcements (Burton, 1954).

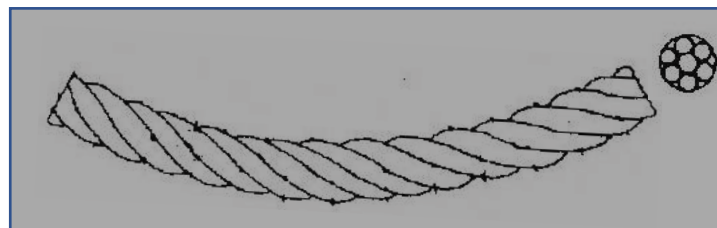


Figure 9: Cable Bead- Tringle Tresse (TT)

2.2.4. TIRE BEAD FAILURE

Several factors can lead to tire beads deterioration and these are listed below (Burton, 1954):

Bead Stresses: stresses can be created by bead due to several factors such as tire inflation, road anomalies, brakes, centrifugal forces, cornering, and travel waves developing in a tire.

Improper Mounting Procedures: Bead kinking, distortion and other types of damage can occur during mounting and changing procedures.

Bead Manufacturing: A bead grommet that is too small can break during the tire curing stage. When the bead grommet is too large, the forces used during tire manufacturing can cause the bead to become kinked or wavy, resulting in the separation between the turns of the wire.

Bead Vibration: Poor adhesion between bead wire and rubber is a principal reason for vibration, creating fatigue-related failure. Once it happens, the separation between the wire and the surrounding wire will be followed by moisture ingress and corrosion eventually.

Handling and Storage: Improper handling and storage methods of bead wire initiate a failure in bead wire. For instance, falling contaminants from roof tops, grease and fretting during wire drawing processes and moisture are all direct causes for tringles' corrosion initiation before getting sleeved.

2.2.5. CORROSION UNDER INSULATION

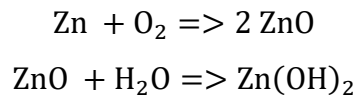
Bead wires can suffer from corrosion attacks before being inserted into tires due to poor storage conditions or mishandling. They can also suffer from corrosion at the end-product level, where the bead wire is inserted inside a tight and thick rubber layer. At that stage, there is still a possibility that discontinuities, gaps, contaminants, inadequate design or installation in the production line makes the bead wire susceptible to corrosion attack. Furthermore, rubber ages when it's exposed to

oxygen; this can lead to poor sealing, which increases the potential for corrosion defects (Hodgins, 2017). Under these conditions, an aggressive corrosive environment can form under the insulation, and corrosion can progress hidden under the rubber until failure occurs.

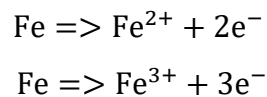
For this reason, corrosion under insulation (CUI) is considered one of the costliest problems in the industry today. For example, studies carried out between 1999 and 2001 showed that the corrosion cost in the United States was estimated in the range of \$276 billion a year, and \$121 billion were spent on preventive maintenance. (Ahmad, 2006) (Doshvarpassand et al., 2019).

2.3. MECHANISM OF CORROSION UNDER INSULATION

Considering that bead wires are zinc coated, white rust (Sziraki, 2001) appears at the onset of corrosion action. This chalky substance appears when zinc is exposed to oxygen and hydrogen (in contact with water or humid environment) to form its related oxide and hydroxide instead of iron oxide, which is the common form of corrosion.



Contrary to zinc oxides, zinc hydroxides have low adherence over metals. As such, they have a high potential to flake off and leave the base material exposed to the common iron oxidation. (fig.11):



Later on, and in the presence of oxygen, OH^- anions form and react with Fe^{2+} and Fe^{3+} to form Fe(OH)_2 and Fe(OH)_3 .



Figure 10: Localized corrosion spot on bead strand

However, even with the exposed surface, iron oxidation can be slowed down by sacrificial zinc protection, which depends on three principal factors (Zhang and Xing, 2004):

- The width of the damaged area - For instance, the maximum protection distance for an exposed area was found to be slightly greater than 7mm.
- Zinc surface activity - In terms of activity, it was found that the protection distance decreases when the zinc activity decreases and vice versa. Therefore, a passivated zinc surface will decrease the protection distance provided by the cathodic zinc protection.
- The electrolyte - The protection distance increases as the electrolyte resistance decreases. For example, a saltwater environment will increase the protection distance; however, it will sacrifice the zinc surface at a higher rate.

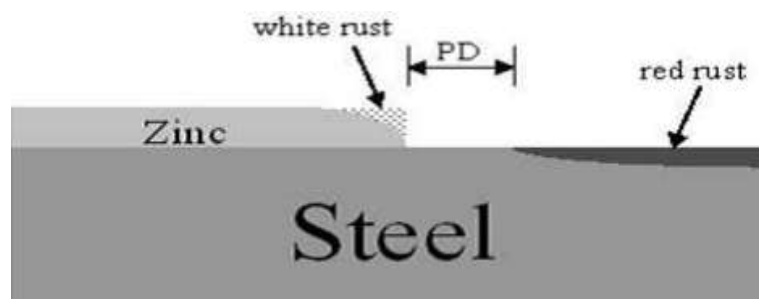


Figure 11: Illustration of Protection Distance (PD) during cathodic protection

2.4. STUDY CASE & OBJECTIVE

In the case of tires' bead wires, it is known that corrosion identification on steel surfaces is not a significant challenge, as can be seen in Fig. 10. However, the problem starts when corroded steel tringles are embedded inside the cooked rubber or when corrosion is initiated on tringles, already embedded under 5 to 7 mm of vulcanized rubber. (fig.12). Thus, the primary purpose of this research is to find a suitable inspection technique to detect any potential corrosion defects inside the tire without damaging it, hence providing better end-product quality, higher safety measures, and economic feasibility.



Figure 12: Cross sectional area of tire bead

2.5. CORROSION INSPECTION

The real issue with CUI is the fact that the only certain way to detect corrosion defects over tringles is to remove the rubber cover. However, such an approach is very expensive and hence avoided. As a result, the required techniques must be non-destructive, where corrosion can be detected using non-invasive means. Some of the proven NDT techniques, such as ultrasonic and X-ray, have been tried before. However, and according to the Michelin Quality Insurance Office, no beneficial data resulted from these inspections. This was due to the complicated composition of the vulcanized rubber that wraps the tringles, which makes it difficult to investigate underneath the corrosion-if it exists. In this context, the next prospected technique

to be used to tackle this problem should acquire a combination of four main characteristics illustrated in table 1.

Accordingly, one ambitious technique to provide successful results is Infrared Thermography (IRT) due to the following reasons:

- IRT is a non-contact technique, which means high temperatures can be monitored safely (Usamentiaga et al., 2014).
- IRT is a non-invasive and non-intrusive technique meaning it does not affect the target or disrupt its operation in any way (Bagavathiappan et al., 2013).
- IRT is an online (real-time) technique that enables large-field monitoring with the immediate result (with the aid of advanced image processing techniques) (Ibarra-Castanedo, 2013).
- IRT does not radiate harmful radiations in comparison to X-ray imaging. Thus, it is suitable for long-term and repetitive use (Usamentiaga et al., 2014).
- IRT based condition monitoring techniques require minimal and fairly inexpensive instrumentations (Bagavathiappan et al., 2013).
- The training hours for IRT inspectors (i.e. level I certification) is less than the required training hours for other NDT techniques e.g. ultrasounds and x-rays (Ibarra-Castanedo, 2013).

Corrosion Measurement Techniques Characteristics			
Direct/ Indirect	On-line/ Off-line	Intrusive/Non- Intrusive	Contact/ Non-contact
Direct measure of metal loss or corrosion rate	Real-time measurement with immediate results.	Constantly exposed to the process steam	Equipment and personnel in contact with the object
Vs.	Vs	Vs.	Vs.
Infer that a corrosion environment may exist	Off-line measurement in a laboratory analysis	No disruption for the plant or process	remote monitoring and measurement

Table 1: Main characteristics of corrosion measurement techniques.

However, despite the various advantages of the technique, thermography has its drawbacks since the inspection efficiency is related to different factors like the nature of the heating source, its location, and heating duration. Also, the camera quality and the surrounding conditions significantly impact the captured image. Furthermore, it might be challenging to detect corrosion under thick non-conductive coatings like rubber. Finally, each configuration (see 2.5.2) has its own parameters and should be considered separately.

2.5.1. INFRARED THERMOGRAPHY

Thermography is a non-destructive detection technique that is used in various applications (medical, industrial, aerospace, etc.). It relies on the object's emitted thermal radiation to collect surface and sub-surface defects information. It can be used over various materials like plastics, composites, wood, metals, etc. These emissions, in their turn, depend on the heat diffusion that occurs in the material; Accordingly, we can distinguish two types of imaging systems, passive and active. In passive thermography (fig.13), the inspection process does not require an external energy source to apply the excitation. The thermal emissions are observed when the object has a different temperature than its surrounding. This application can be seen in night-vision goggles or metal-working processes when hot finished products are inspected as they cool down. The various cooling behaviours of the surface can provide beneficial information related to any potential defects. The defected surface

will generally assume lower temperature because heat diffuses at a lower rate in the defected medium than the intact medium. (Meinlschmidt and Aderhold, 2006)

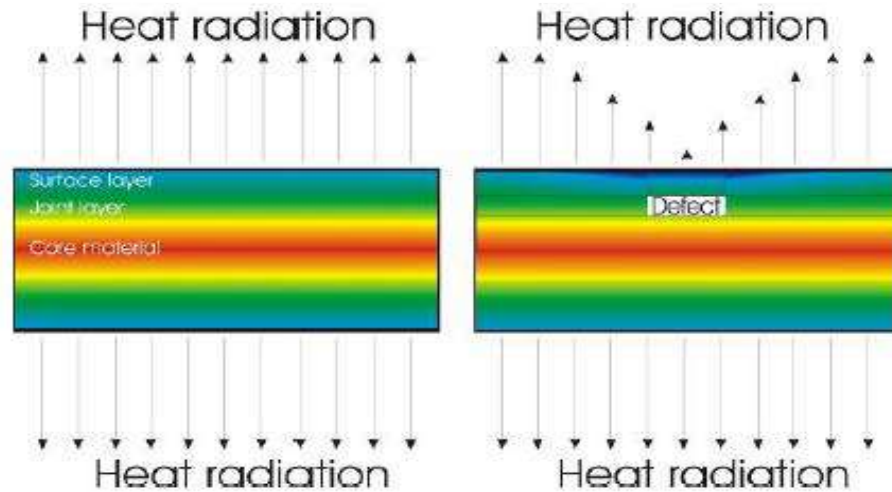


Figure 13: Principle of the passive thermography

In contrast, active techniques require an external source of heat excitation to stimulate the heat inside the object to be inspected, and the heat transfer in its turn will be governed by the material's physical properties like density, thermal conductivity and diffusivity. As shown in Figure 14, the defected surface will assume a higher temperature due to the fact that defected gaps act as a heat insulators, hence heat emissivity shows a higher value with respect to the intact area. (Meinlschmidt, 2005)

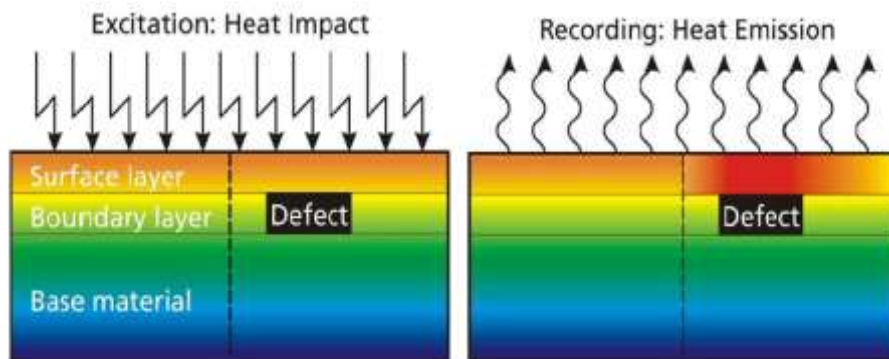


Figure 14: Principle of the active thermography

In terms of classifications, methods can be divided based on the position of the IR camera and the source with respect to the test piece; if they are on the same side, it will be noted as reflection mode; otherwise, it is transmission mode. Furthermore, it can be classified based on the heat stimulation technique as it can be seen in fig. 15 (Ibarra-Castanedo et al., 2009):

- 1- Optical in terms of photoelectric flash or laser as an excitation source.
- 2- Vibro-thermography using an ultrasonic transducer.
- 3- Induction using electromagnetic coils (our case study).

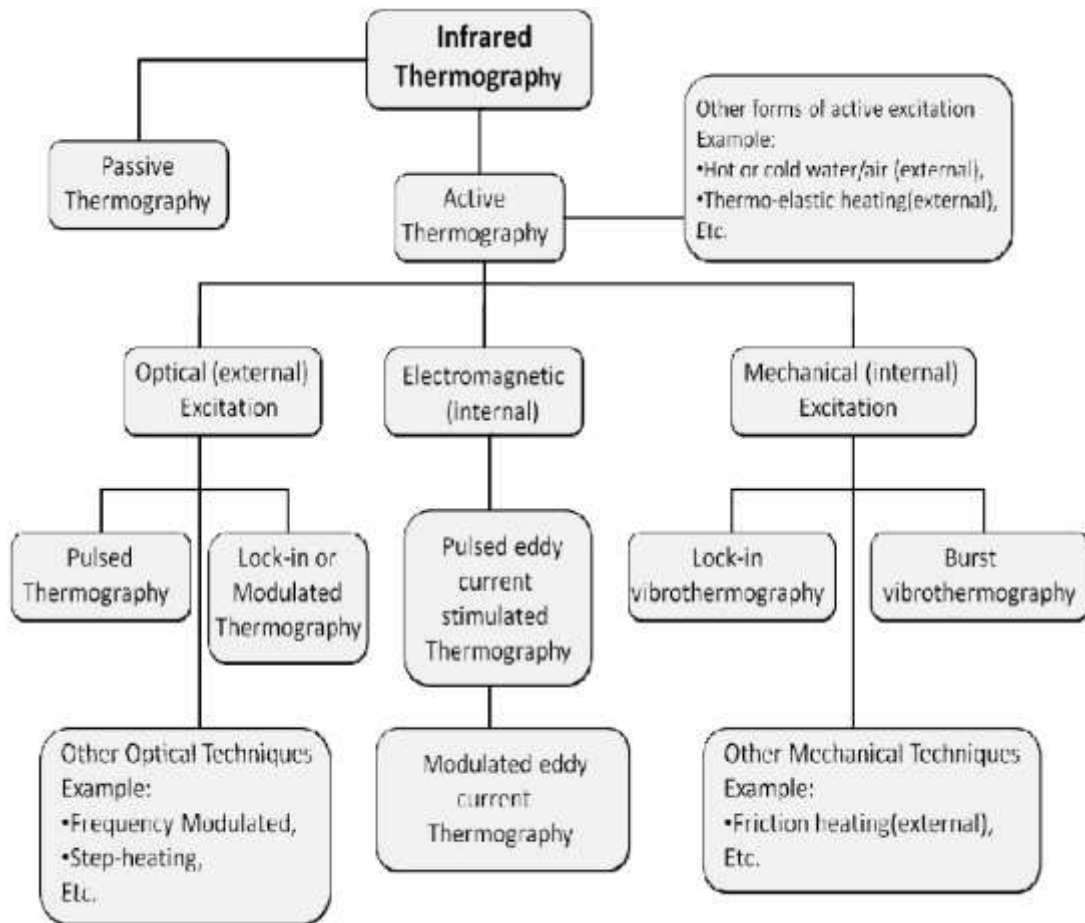


Figure 15: Classification of thermography testing methods (Ibarra-Castanedo et al., 2009)

In this context, each of these techniques has its own advantages and drawbacks. For example, the optical technique proved its efficiency when inspecting planar defects

like wide corrosion layers. (Shuohan et al., 2013). However, it suffers from operational complexity, cost, and poor practicality in industrial fields. In a similar case, vibro-thermal techniques are characterized by uniform heating; however, its limited practicality makes it unpopular when working on vibration soaking samples using mechanical excitation (e.g., rubber-coated sample.). Induction or pulsed thermography (fig.16) may have promising potentials over the inspection limitations related to other techniques. For instance, it is simple, affordable, and easier to operate. Moreover, it is safe and has proved its efficiency in detecting extended and fine defects over the surface (e.g., cracks, corrosion).

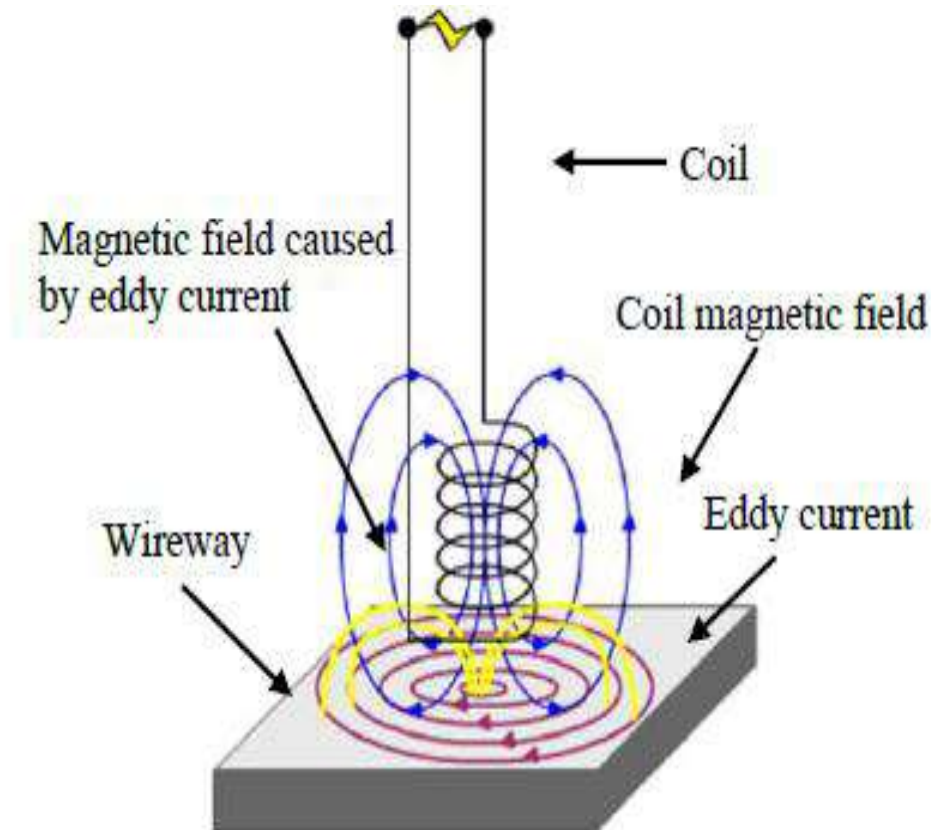


Figure 16: Induction thermography electromagnetic operational mode

2.5.2. INDUCTION THERMOGRAPHY

Known also as eddy current pulsed thermography (ECPT) since it integrates thermography with eddy current technique. Accordingly, a circular coil is connected to an alternating current source to generate electromagnetic pulses hitting the

surface of the sample to be inspected (fig. 17) (Xu et al., 2020). The alternating magnetic pulses will then create an eddy current inside the metallic sample, which heats it by resistive losses and as such, releases heat. Magnetic flux is governed throughout the following equation: $EMF = -\frac{d\phi B}{dt}$

Where EMF is the electromotive force and ϕB is the magnetic flux through the circuit (in Weber). Finally, and based on the defects' severity along with the investigated sample, electrical current densities will be disturbed, hence the generated heat quantity as well. The latter will be the key parameter to identify the intact surfaces from the defective ones through thermographic image processing and analysis produced by the infrared camera (Russ and Neal. Brent F, 2017). In terms of corrosion, which is a series of iron oxides and hydroxides (de la Fuente et al., 2011), it will generate a higher temperature than sound steel according to previous work (He et al., 2014). As a result, the variation in conductivity will lead to a change in the thermal response. Furthermore, steel emissivity range between 0.2 and 0.3, on the other hand, corrosion emissivity goes from 0.65 to 0.7, hence this difference in emissivity will play a significant role in distinguishing any potential corroded areas.

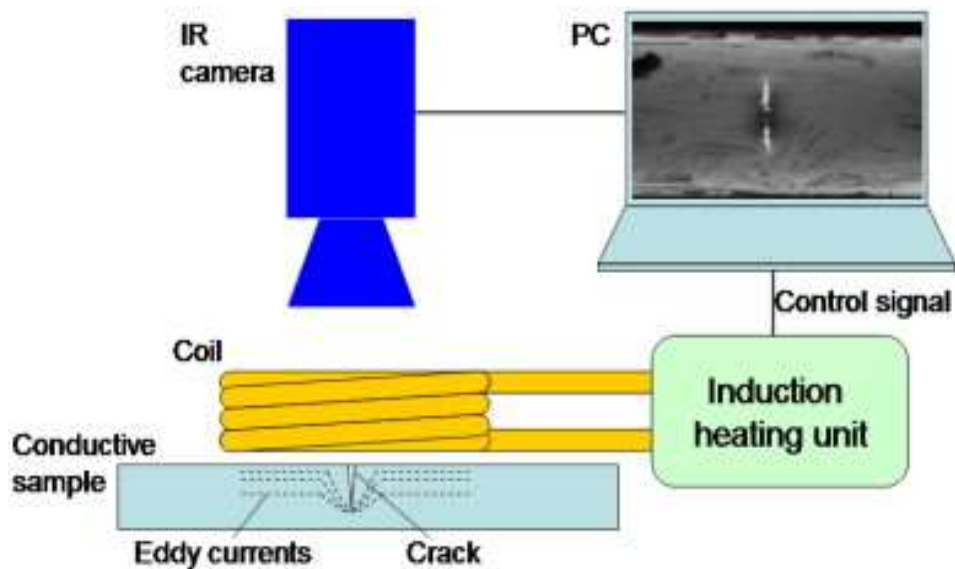


Figure 17: Induction thermography typical setup

2.5.2.1. CHARACTERISTIC LENGTHS IN INDUCTION HEATING

As the eddy current testing uses the conductive aspects to detect corrosion and other defects, induction thermography relies on the thermal and electromagnetic aspects of the material (Netzelmann et al., 2015).

For instance, to well exploit the induction thermography technique, one must take into consideration the electromagnetic skin effect created on the surface of the inspected material. Skin effect is when the alternating current distributes throughout a conductor so that the largest portion of the current density is running on the conductor's surface, and low density or no current passes through the core of the conductor (fig.18).

The cause of the skin effect can be explained as a current "I" flowing throughout the conductor creates a magnetic field. As a result, Eddy current will be induced within the conductor, opposing the current flow in the center and reinforcing the total current near the surface, resulting in the skin effect (fig. 19). In physical expression, skin effect can be expressed as the following:

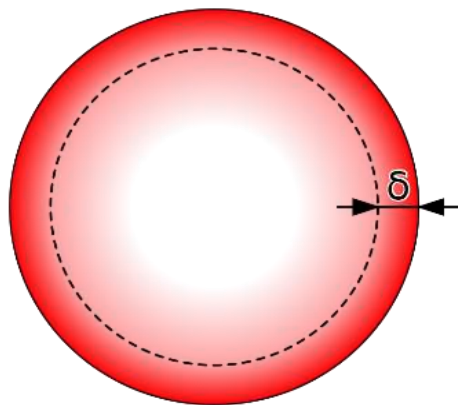


Figure 19: Distribution of current flow in a cylindrical conductor (Wikipedia)

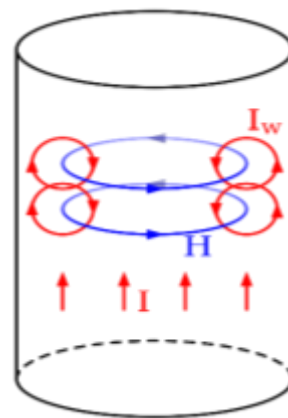


Figure 18: Cause of the skin effect (Wikipedia)

$$\sigma = \sqrt{\frac{1}{\pi f \sigma_e \mu} \frac{\partial T}{\partial t}} = \alpha \nabla^2 T \quad (1)$$

σ_e is the electrical conductivity,

μ the magnetic permeability

f is the current frequency.

Where σ represents the depth below the surface of the conductive material, at which the current density will be reduced to 1/e or 37% of the current density on the surface. Skin depth is inversely proportional to electrical conductivity, magnetic permeability, and frequency which is the only parameter that can be controlled if there is a need to increase or decrease the skin depth. For instance, a low penetration depth (low frequency) is preferable when light superficial corrosion is targeted, since a large portion of passing current will condense on the surface. Hence any minor defect can be detected due to the current/heat disturbance. On the other hand, high frequency is employed when high penetration depth is required to reach sub-surface defects. Usually, induction devices provide frequencies ranging from 3 kHz–3 MHz, which allows for detecting most defects in metallic materials. (Zenzinger, 2007). Another vital material property is diffusivity α (m²/s), which represents the rate at which heat can diffuse through a sample, taking in consideration its thermal conductivity and heat capacity as the follows:

$$\alpha = k/\rho C \quad (2)$$

k is thermal conductivity (W/mK);

ρ is density (kg/m³)

C is specific heat (J/kg K).

As shown in figure 20 (Ashby, 2011), materials like aluminum conduct heat at high rates, making it challenging to record temperature history. As a result, the inspection will require advanced camera properties to achieve the inspection properly. On the other hand, rubber has a low diffusivity rate ($0.9\text{-}1.3 \times 10^{-7} \text{ m}^2/\text{s}$) which might make it difficult to detect diffused heat easily.

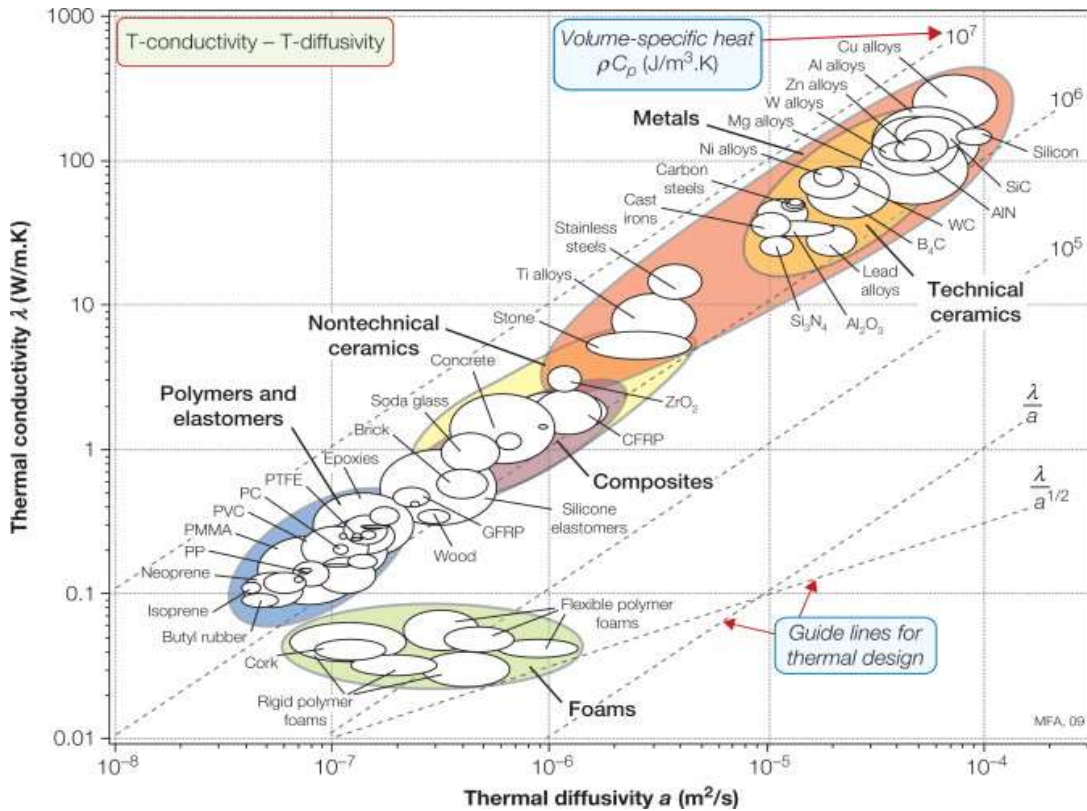


Figure 20: Thermal conductivity plotted against thermal diffusivity.

2.5.2.2. DESIGN & CONFIGURATIONS

The configuration of eddy current pulsed thermography (ECPT) is one of the predominant factors that can affect the assessment of the tested piece. Various models can be represented in this context (fig. 21). For instance, line-coil excitation represents the most straightforward design and has been used to inspect fatigue crack-related defects (Wilson et al., 2011). Circular/rectangular single or multi turns coils were also used to evaluate the contact fatigue of gear and carbon-fiber-reinforced plastic materials (Liu et al., 2015) (Wu et al., 2014). Although these

configurations were beneficial in some applications, they have limitations such as non-uniform heating and view blockage when using the reflection mode.

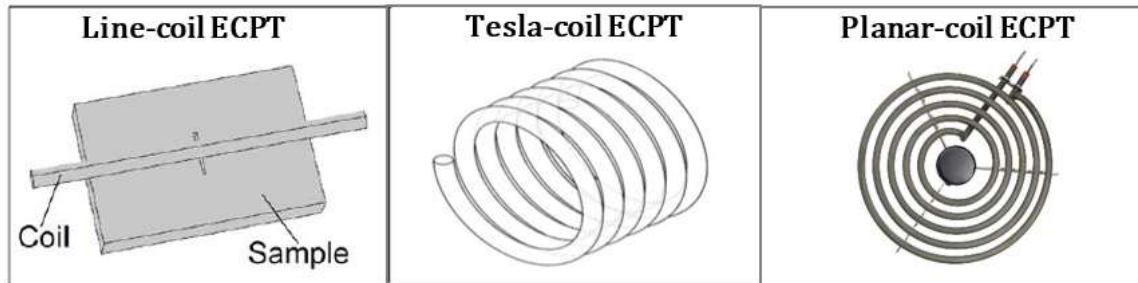


Figure 21: Conventional ECPT with different configurations.

However, Helmholtz and Yoke configuration were popular due to their ability to provide uniform heating and open view imaging between the two coils (fig. 22) (Tian et al., 2016).

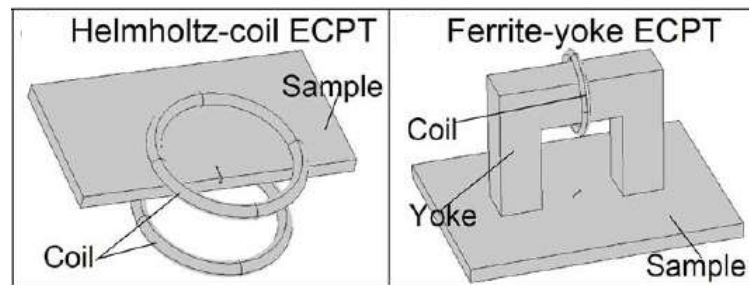


Figure 22: ECPT configurations for uniform heating.

2.5.3. THERMAL EMISSIVITY BACKGROUND

Considered a non-destructive technique, Infrared Thermography relies on the objects' temperature to detect anomalies on or below the inspected surface. Each surface temperature radiates different electromagnetic wavelength ranging between 0.75–1000 μm (fig. 23) (Meola, 2012).

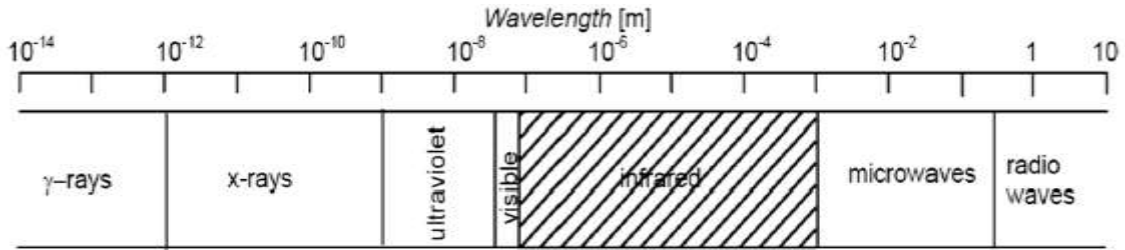


Figure 23: Electromagnetic spectrum.

In 1860, the blackbody concept was introduced by Gustav Kirchhoff as an ideal surface absorber and emitter for radiations (ϵ : total emittance= 1, α : total absorbance= 1) while neither transmits ($\bar{\tau}$: total transmittance= 0), nor reflects (ρ : total reflectance= 0) any exposed radiation (Meola, 2012). One important parameter here is emissivity, which describes the material's ability to emit energy from its surface to the surrounding environment in the form of heat. Emissivity is expressed as a ratio between the thermal radiation from the surface of the material and the thermal radiation of a black body which is unity. Between 1879 and 1884, it was found that the emitted energy from a black body can be obtained by integrating Planck's law and it will be proportional to T^4 along with taking into consideration Stefan-Boltzmann's constant (Meola, 2012). However, for the real object case, this law does not approach the typical body behaviour in the same precise manner.

$$E_b = \int_0^{\infty} \frac{2\pi hc^2}{\lambda^5 (e^{hc/\lambda k_b T} - 1)} d\lambda = \bar{\sigma} T^4 \quad (3)$$

$\bar{\sigma}$ as the Stefan-Boltzmann's constant ($\bar{\sigma} = 5.67 \times 10^{-8} \text{ W/m}^2 \text{ K}^4$),

h is the Planck's constant ($h = 6.6 \times 10^{-34} \text{ Js}$),

c is the light speed ($c = 3 \times 10^8 \text{ m/s}$),

k_b is the Boltzmann constant ($k_b = 1.38 \times 10^{-23} \text{ J/K}$),

λ is the radiation wavelength,

T is the absolute temperature of blackbody.

Accordingly, for temperatures that are close to room temperature, this thermal radiation is within the infrared spectrum, while in case of much hotter objects, this range of radiation extends towards the visible spectrum. Hence it becomes visible by the naked eye.

2.5.4. IMAGING SYSTEMS

To analyze the generated heat from the inspected sample, the concept of thermal energy diffusion must be clearly understood. Heat transfer in a system is achieved by three means: convection, radiation, and conduction. In convection, heat is transferred from one place to another throughout the surrounding fluids (gas included) movements. Thermal radiation and heat energy are emitted from the object in the form of electromagnetic waves, so no medium is required for heat diffusion. Conduction is when heat transfer takes place within the solid itself. Accordingly, the thermal conductivity of a body or a material represents its ability to conduct heat flux through its volume. It is expressed as a quantity of heat conducted over a specific time through a slab of material of a specific area and thickness when there is a temperature differential between the two faces of a slab (Dinwoodie, 2000). When it comes to radiometry, emissivity ϵ represents a significant parameter for accurate inspection. However, other parameters also contribute to the overall detection mechanism, such as object reflectance ($\bar{\rho}_{obj}$), absorbance ($\bar{\alpha}_{obj}$) and the surrounding transmittance $\bar{\tau}_{atm}$ (Maldague, 2001), hence the total amount of electromagnetic energy, E_{tot} received by a thermal camera is measured based on Stefan-Boltzmann's law (fig.24.):

$$E_{tot} = E_{obj} + E_{refl} + E_{atm} \quad (4)$$

Given that E_{obj} is the energy emitted by the object, E_{refl} corresponds to the reflected energy from the surroundings emitted by the object and E_{atm} is the energy emitted from the atmosphere.

However, a real object is treated as a greybody (whose absorptivity of surface does not vary with variation in temperature and wavelength of incident radiation). Thus,

its reflectance can be assumed as $\bar{\rho}_{obj} = 1 - \varepsilon_{obj}$, its absorbance, $\bar{\alpha}_{grey} \approx 0$. And, the atmosphere emittance, $\varepsilon_{atm} = 1 - \bar{\tau}_{atm}$ where the atmosphere reflectivity is $\bar{\rho}_{obj} \approx 0$. Accordingly, equation (3) and (4) can be drawn as the following:

$$E_{tot} = \bar{\tau}_{atm} \cdot \varepsilon_{obj} \cdot \bar{\sigma} \cdot T_{obj}^4 + \bar{\rho}_{obj} \cdot \bar{\tau}_{atm} \cdot \bar{\sigma} \cdot (T_{refl})^4 + \varepsilon_{atm} \cdot \bar{\sigma} \cdot (T_{atm})^4$$

$$E_{tot} = \bar{\tau}_{atm} \cdot \varepsilon_{obj} \cdot \bar{\sigma} \cdot T_{obj}^4 + (1 - \varepsilon_{obj}) \cdot \bar{\tau}_{atm} \cdot \bar{\sigma} \cdot (T_{refl})^4 + (1 - \bar{\tau}_{atm}) \cdot \bar{\sigma} \cdot (T_{atm})^4$$

$$T_{obj} = \sqrt[4]{\frac{E_{tot} - (1 - \varepsilon_{obj}) \cdot \bar{\tau}_{atm} \cdot \bar{\sigma} \cdot (T_{refl})^4 - (1 - \bar{\tau}_{atm}) \cdot \bar{\sigma} \cdot (T_{atm})^4}{\varepsilon_{obj} \cdot \bar{\tau}_{atm} \cdot \bar{\sigma}}} \quad (5)$$

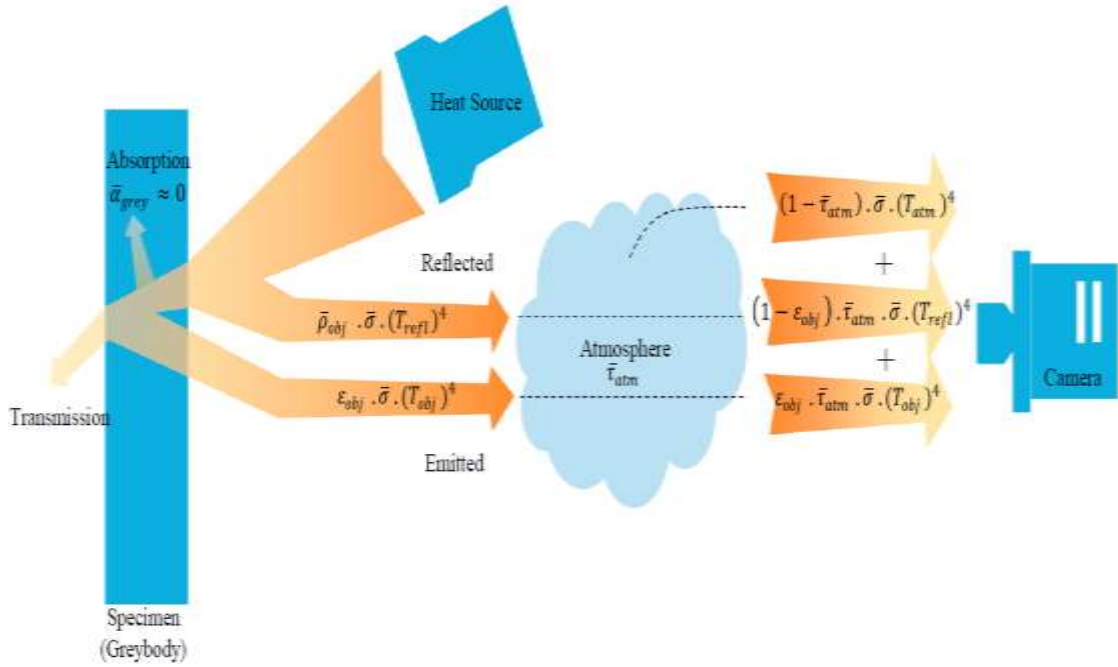


Figure 24: Greybody surface behavior

2.5.5. CORROSION DETECTION & HEAT TRANSFER

Along with relying on radiation energy to be detected using thermal cameras, defects under coatings and surfaces are analyzed based on the heat conduction theories in materials. For instance, heat flow equation is solved to uncover the trend of propagation with respect to time. Such model of presentation is known as Fourier equation and was introduced by Carslaw and Jaeger (Carslaw and Jaeger, 1959):

$$\frac{\partial T}{\partial t} = \alpha \nabla^2 T \quad (6)$$

With α representing the thermal diffusivity (see 2.5.1), which governs the speed of heat conduction of an object over its ability to store thermal energy. Taking into consideration that heat propagates in one-dimensional heat flow and the surface is heated uniformly. The previous equation can be further developed into equation (7):

$$\frac{\partial T}{\partial t} = \alpha \frac{\partial^2 T}{\partial z^2} \quad (7)$$

Where z corresponds to the direction parallel to the body thickness. Furthermore, this equation can be extended to provide explicit meaning when using Dirac pulse plane source excited from the surface of the medium (equation 8)

$$T_{s-inf}(z, t) == T_0 + \frac{Q}{e\sqrt{\pi t}} \Big|_{z=0} \quad (8)$$

T_{s-inf} is the temperature evolution in the semi-infinite body,

T_0 is the initial (ambient) temperature,

$\frac{Q}{e\sqrt{\pi t}} \Big|_{z=0}$ is the boundary condition,

$e = \sqrt{\rho KC}$ is the thermal effusivity ($Ws^{1/2}/m$)

From the previous equation, the surface temperature of the given semi-infinite body (assumed homogenous and opaque) decays with the slope of $1/\sqrt{t}$. This observation comes in congruence with fig. 25, as it can be noticed that the more L increases, the more diffusion takes place as well, and as a result, the lower level of temperature stabilization will occur.

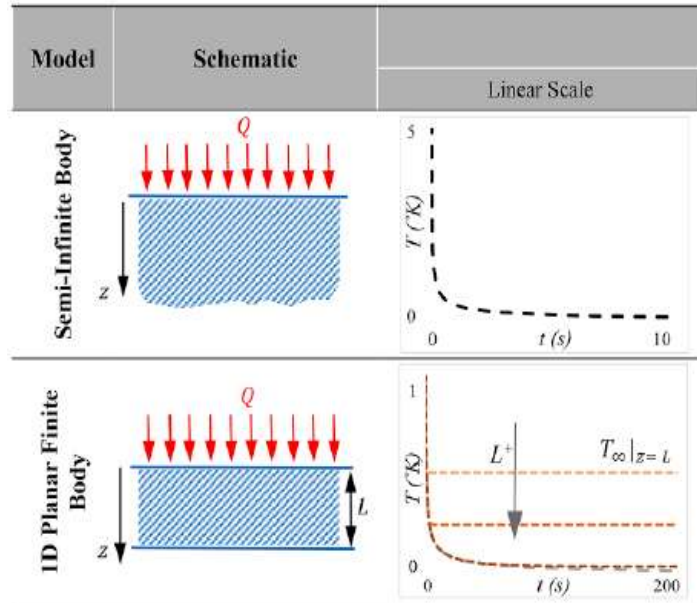


Figure 25: classical models of heat conduction in solids

In a similar manner, equations for finite planar bodies were developed as well to simulate real case corrosion defect scenarios. For instance, worked on finding the equation for the surface temperature of a fixed thickness plate L prompted by a Dirac pulse equation.

$$T_{\text{plate}}(z, t)|_{z=0} = T_0 + \frac{Q}{\rho CL} \left[1 + 2 \sum_{n=1}^{\infty} \exp(-n^2 \pi^2 F_0) \right] \quad (9)$$

$F_0 = \alpha t/L^2$ is known as Fourier number

Based on this relation, the term inside the brackets represents the reflected heat from the surface. In other words, as the heat propagates inside the body, there will be a moment where the heat will accumulate to a constant temperature equivalent to $\frac{Q}{\rho CL}$.

For further clarification, a corrosion defect can be illustrated by an air gap located beneath the surface of a single-layered body by a distance L (fig. 26) (Vavilov et al., 1996). Hence the air gap defect is characterized by a higher thermal resistivity and it will reflect most of the incident thermal energy, back towards the surface (Lau et al., 1991). Accordingly, any modification to this property will generate intensity distinction through reflecting regions containing sub-surface defects. These defects will disrupt (reduce) the diffusion rate of heat front, inside the object. Consequently, the defects will appear in the image with distinct intensity with respect to the sound area. Figure 26 shows the temperature evolution over time for a point over the center of defect at the surface of the specimen. For a constant defect depth (d), the increase in defect diameter (D), the heat diffusion converges toward the 3D diffusional regime. As a result, temperature line will shift upward from a finite plane with thickness (L) to a finite plane with thickness ($L-d$). This behavior can repeat also when defect diameter is fixed whereas the defect upper-thickness is variable. For instance, when the upper thickness is relatively small, the divergence between the defected and intact area lines is large. However, as going toward larger thickness above the defect, this divergence becomes smaller and hence much difficult to detect.

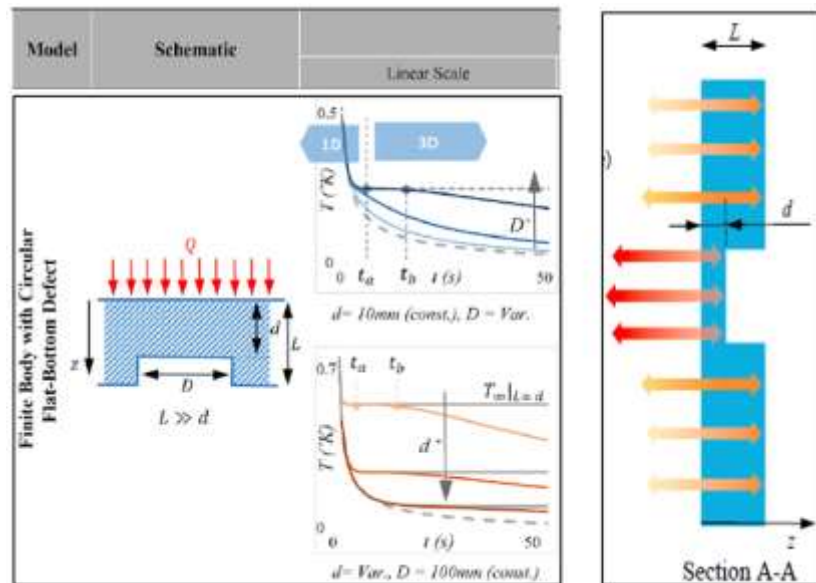


Figure 26: Temperature contrast and derivatives variations for different thicknesses.

2.6. THERMAL IMAGE PROCESSING

During an inspection, thermographic images may face challenges to provide precise detection for defective areas. These zones of interest may show up as subtle marks due to various reasons that include, but not limited to pixels count, IR camera quality and non-uniform properties of the inspected surface where data are collected from. Moreover, as liberated photonic energy W is directly proportional to the frequency of the oscillating radiations, some details can be missed or misinterpreted in case the received photons have very low energy. An example of such situation is usually found with long-wavelength radiation, which is the case of far-infrared radiations. For this reason, raw images require additional processing techniques using qualitative analysis to retrieve further details or peculiar marks.

Several methods of data analysis in infrared NDT have been developed (Ibarra-Castanedo et al., 2004). Some of them require human intervention, others do not. The most common techniques are summarized in the following:

- Noise reduction: to reduce the noise effect over the received signal.
- Contrast balance: to highlight subtle details in the original picture.
- Edge detection: to define discontinuities in the tested sample.

In noise reduction, the most common procedure is the subtraction technique. In this context, two techniques can be applied, either spatial reference technique -where subtraction applies between two acquired images at the same time from two different experiments or through temporal reference technique where images are recorded closely to remove noise obtained due to non-uniform heating for example (Bolu et al., 2010). Noise reduction can also be applied through linear and non-linear filters (Bolu et al., 2010). In linear filtering, each pixel of the original image goes through computational convolution by a square matrix - having an odd number of elements - called a kernel. Accordingly, a centered kernel $(n+1 \times n+1)$ is introduced and multiplied by the matching pixel. The values of the resulting smaller matrix (which has the same size as the original kernel) are averaged, and the initial pixel value p is substituted with the new value p_0 computed as the following:

$$p_0 = B(a_1p_1 + a_2p_2 + \dots a_{(n+1)^2}p_{(n+1)^2}) \quad (10)$$

Where a_i is considered as the kernel weight, B is scaling factor, and p_i are the $n+1$ -pixel values within the kernel centered on p (Ibarra-Castanedo et al., 2004). An example of such mechanism is illustrated in figure 27. On the other hand, nonlinear filters follow a similar algorithm as the linear ones except that the relation between the value of the central pixel p and its replacing value p_0 is not linear, which means, it may change its value from one-pixel color to the other.

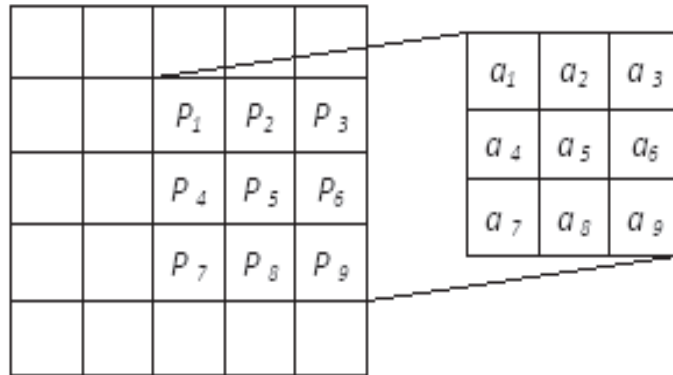


Figure 27: Linear spatial filtering application.

On another scale, image correction can be applied over histograms and contrasts. In this technique, the procedure will deal with the greyscale images. For instance, each pixel can acquire one of 256 possible values: a value equal to zero corresponds to the black color, and 255 corresponds to the white color. Hence, adjusting the tonal distribution and subtle details can appear again and become well observed. The result is an image with increased contrast and a higher tendency to distinguish tonal variations along the picture. Figure 28 (Gonzalez et al., 2011). An example of the above is shown in figure 28.

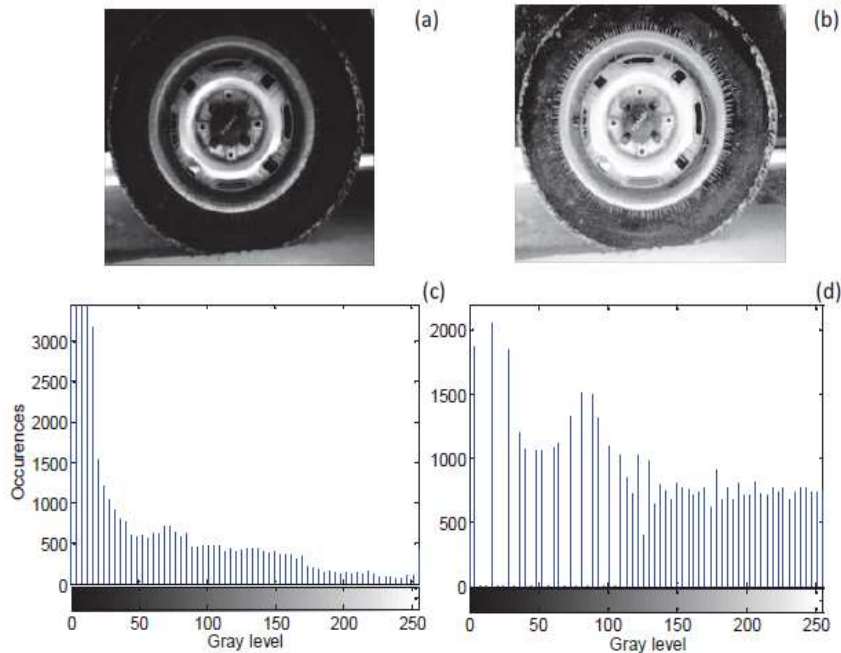


Figure 28: a) original image b) correspondent histogram c) Enhanced image d) correspondent histogram

Finally, the edge detection technique. This technique is widely used in IR-NDT methods to pinpoint and size the damaged area on an inspected surface. It is based on highlighting the contour of the zone of interest by removing the constant features in the background, leaving only the variation with respect to that constant. Thus, contours are defined as local discontinuities in luminance, i.e. areas in the image where there are "abrupt" changes in luminance. This procedure is applied through first and second derivatives since they are considered the simplest, the most common and hence the most exploited. In this method, thermal gradients across consecutive pixels are calculated. Hence abrupt changes in light intensity are spotted. Figure 29 (Ibarra-Castaneda et al., 2004) below illustrates first-order derivation for light intensity spike $f(x)$ in function to the spatial coordinate x , $f'(x) = \frac{df(x)}{dx}$.

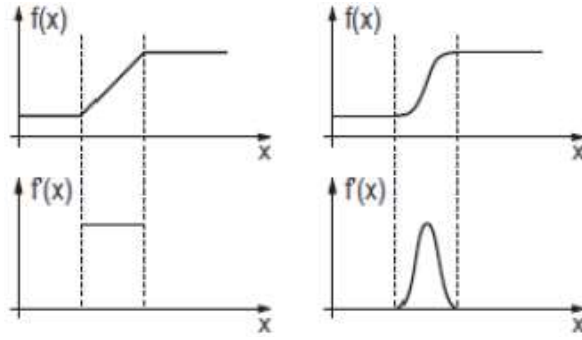


Figure 29: 1st derivative on intensity functions for 2 types of edges

Such a ramp indicates irregular changes in the luminance level, which leads to identifying a possible contour. However, some derivations can be generated due to noise intervention. Hence these maximum local values are not always related to “true” contours but to noise effect as well. For this reason, a threshold level is taken into consideration and peaks below this threshold are defined as “false” contours and ignored eventually. In a discrete, one-dimensional domain, the first derivation for a set of intensity values $x(n)$ is calculated as follow:

$$x'(n) = \sum_{k=-\infty, k \neq 0}^{\infty} \frac{(-1)^k}{k} x(n-k) \quad (11)$$

For instance, the first derivative of the 10th pixel is:

$$x'(10) = x(11) - x(9) + \frac{x(12)}{2} - \frac{x(8)}{2} + \frac{x(13)}{3} - \frac{x(7)}{3} + \dots \quad (12)$$

In practice, discrete domains are 2-dimensional, and instead, the gradient is considered, which is the first derivative with respect to x and y :

$$G(x, y) = \left(\frac{\delta}{\delta x}, \frac{\delta}{\delta y} \right) \quad (13)$$

Further identification of false contours is done using the second derivative (Laplacian operator), where only the zeros surrounded by maximum and minimum values are considered (Li et al., 2010).

$$G(x, y) = -\nabla^2 F(x, y) = \frac{\partial^2}{\partial x^2} F(x, y) + \frac{\partial^2}{\partial y^2} F(x, y) \quad (14)$$

Figure 30 (Ibarra-Castanedo et al., 2004) below helps visualize the concept.

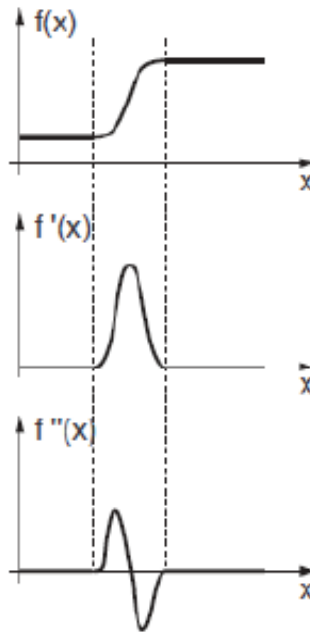


Figure 30: First and second derivatives over edge intensity function

2.7. RECENT RELATED WORK

The first application of ECPT in the steel industry was reported more than two decades ago (Netzelmann, 2016), where continuous inductive heating on moving steel bars was applied to detect longitudinal cracks. Furthermore, the technique has been applied using phase sensitive-detection and periodic heating for characterization of coating adhesion and using pulsed excitation for crack detection in turbine blades (Netzelmann et al., 2015). New applications were reported on steel components and carbon fiber reinforced polymers (Riegert et al., 2004). Also, there

was significant work on analytical and numerical modeling of the signal from cracks (Oswald-Tranta, 2004). In terms of corrosion, Foudazi experimented the use of Microwave thermography in the detection of corroded steel bars (Foudazi et al., 2015). Accordingly, 3 steel bars of 4.8 cm radius and smooth surface were used. As it can be seen from (fig. 31a) each piece held an approximative area of 1 cm² of corroded material with gradual severity. In (fig 31b), the corroded areas were glowing in comparison to the sound area due to 2 reasons: 1) Corroded materials hold low thermal conductivity; hence heat will dissipate in a slower rate with respect to intact area. 2) Increased corrosion severity tends to absorb a higher flux of microwave radiation which can help to improve not only the quantitative side but the qualitative aspect in corrosion severity level as well.

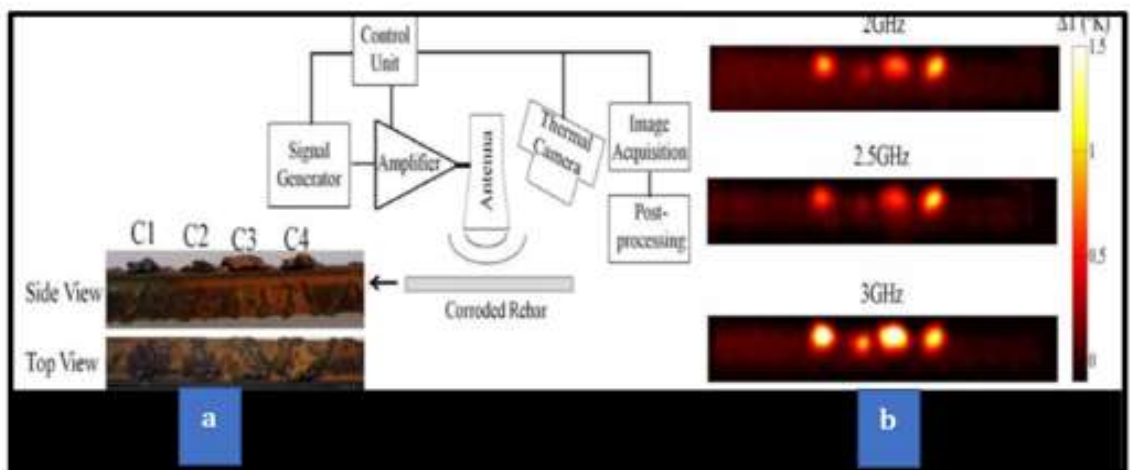


Figure 31: Temperature profile of corroded rebar after 10 s. of inductive heating

Pieper et al. (2014) went further in their experiment where they tried to observe the change in inspected temperature between when steel bars (AISI 1008 - L: 150 mm and R= 4.8 mm) are being inspected in air against when embedded inside cement-based structure. Accordingly, as it can be seen in (fig. 32a), 2 steel bars were inspected, one with localized severe corrosion (1 to 4 mm) on a portion of its length, and the other with lighter corrosion (on the order 0.2 mm or less) along half of its length. Later, both steel pieces have been heated by microwave energy for 15 s., and as illustrated in (fig 32b and 32c), the corroded areas were easily identified as

highlighted by the black circle, when inspected in free air. However, when applying the same inspection parameters with 2 other steel bars (fig. 32d clean to the left and completely corroded to the right) being embedded in a concrete block as shown in (fig. 32e), thermal imaging showed significant reduction in received infrared radiation due to the absorption of emitted energy by the concrete block.

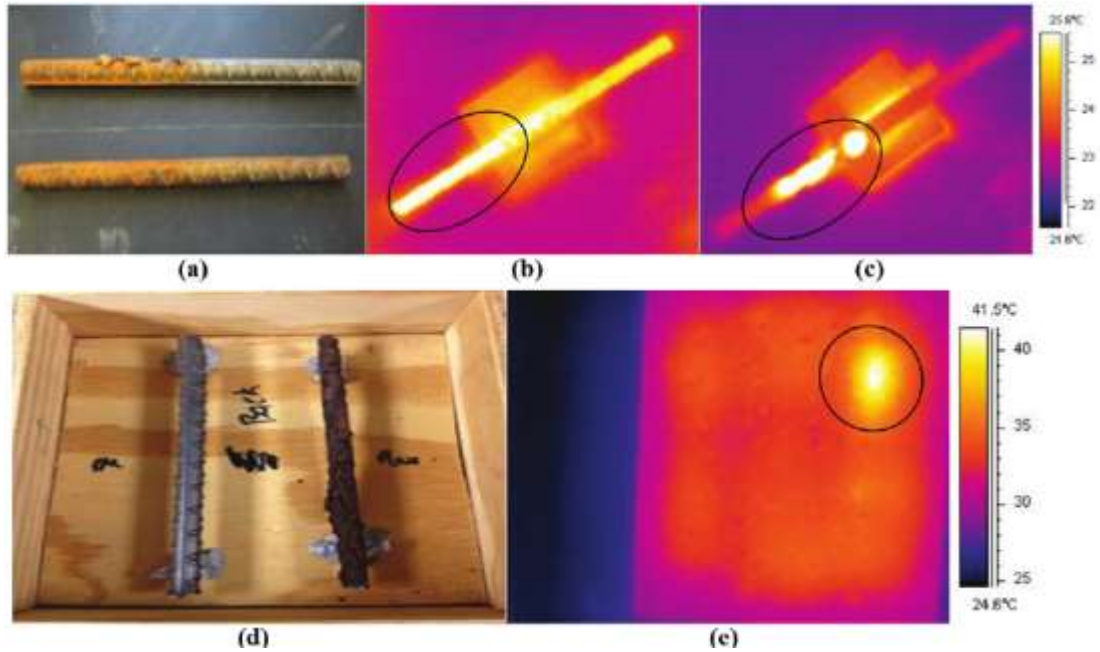


Figure 32: (a) Rebar with localized significant (top), and light corrosion (bottom). Thermal image of rebar with (b) light corrosion, and (c) localized corrosion

CHAPTER 3

METHODOLOGY

This chapter will present the various experimental procedures took place before to starting the inspection trials, such as images calibration, samples' design and preparation. Finally, relevant equipment, system setup and operating conditions were presented.

3.1. INFRARED IMAGE CALIBRATION

In order to optimize the procedure of image processing, we conducted a preliminary study to exploit the MATLAB software and, in particular, the image processing acquisition. Throughout this study, we aimed to acquire more awareness about the commands reported in the MATLAB algorithm. In other terms, it will lead to conscious management of the two-dimensional (2D) signals in the matrices that represent the thermal images.

Simulations for pulsed thermography

In this context, heat propagation was simulated over cooked rubber surface (3x3 cm.) when exposed to pulsed thermography testing. This simulation will be based on radial heat propagation from the central point to the extremes of the surface. Once snapshots and videos are taken, statistical and mathematical parameters to warn of the presence of damage. Then, the system will compute the thermal image's first and second derivative with two spatial filters to enhance image contrast, localize the defect and size its dimensions. Such an approach will enable us to apply partial automation in the inspection process, along with increased background isolation and higher color contrast. Further details and this image processing are reported below.

This preliminary study aimed to calibrate the image processing procedure through basic simulation. Accordingly, we reproduced five videos composed of 14 frames

each. These videos represented the heat flow that is propagating from a central point towards the extremes of the image. For instance, the first movie is associated with an damaged situation as a reference video (shown in figure 33).

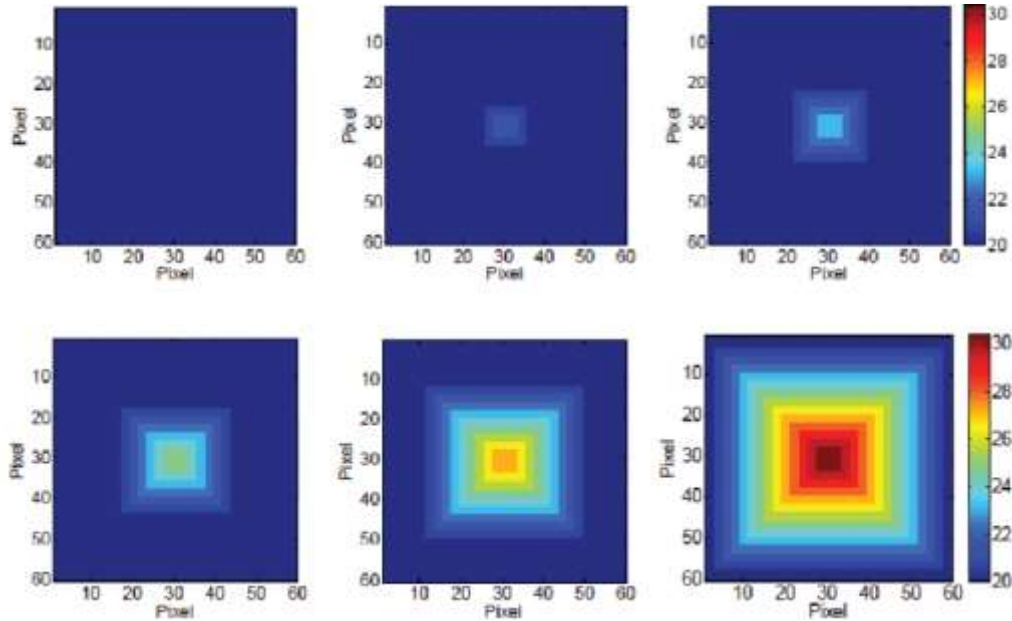


Figure 33: First simulation for the baseline sample

As it can be seen, the temperature is increasing according to a square pattern, and this increase was $\sim 0.8^{\circ}\text{C}$ at each step. The same procedure was also applied over the four corroded surfaces. The presentation of these defective surfaces is shown in figure 34.

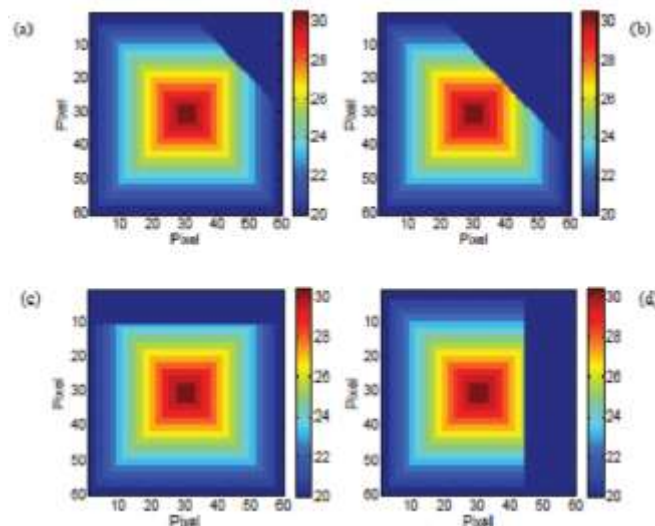


Figure 34: Calibrating Simulation: a) small 45° b) large 45° c) horizontal d) vertical

From each frame of these movies, the correlation coefficient was calculated. This parameter is used to establish adequate calibration for image processing. Accordingly, comparison and matching for testing images will be run with respect to baseline image as a reference. In this context, Pearson coefficient $\rho_{X,Y}$ is used to assess the linear relationship between the variables:

$$\rho_{X,Y} = \frac{\text{cov}(X,Y)}{\sigma_X \sigma_Y} = \frac{E[(X - \mu_X)(Y - \mu_Y)]}{\sigma_X \sigma_Y} \quad (15)$$

where μ and σ represents the mean and standard deviation for each variable and $\text{cov}()$ represents the covariance. The correlation value will be in the range of -1 and 1, a value closer to 1 represents linear positive relationship, -1 represents a negative relationship (anticorrelation) and 0 denotes the absence of a relationship. In case of two-dimensional comparison such as images, equation becomes:

$$r = \frac{\sum_m \sum_n (A_{mn} - \bar{A})(B_{mn} - \bar{B})}{\sqrt{(\sum_m \sum_n (A_{mn} - \bar{A})^2)(\sum_m \sum_n (B_{mn} - \bar{B})^2)}} \quad (16)$$

where A and B two matrices that represents the 2 images.

Figure 35 shows the correlation values, for the five simulated samples. As it can be seen, the correlation coefficient for each frame has been computed and compared to the correspondent frame of the baseline. The damage was readily detected for all the samples and the highest correlation referred to the 45° corrosion spot.

As the final step linear filtering was used. Two filters were applied for this calibration: the Roberts filter [R] that belongs to the directional filters category) and the Laplacian filter [L] which is more favorable to determine edges and contours.

$$R = \begin{bmatrix} 0 & 0 & 0 \\ 0 & -1 & 0 \\ 0 & 1 & 0 \end{bmatrix} \quad L = \begin{bmatrix} 0 & -1 & 0 \\ -1 & 4 & -1 \\ 0 & -1 & 0 \end{bmatrix}$$

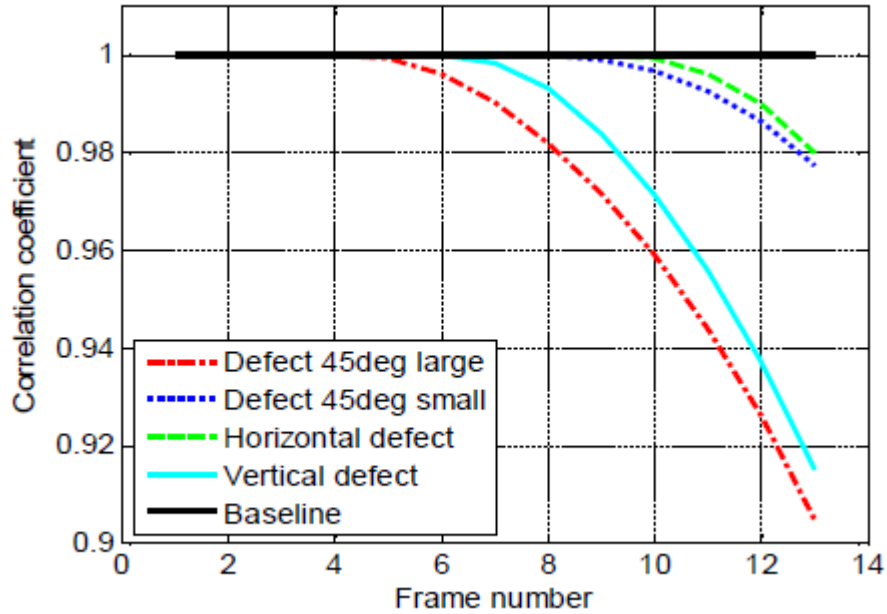


Figure 35: Calibration Simulation - Correlation Coefficient

Figure 36 below shows the reproduced images retrieved from the Laplacian and the Roberts filters. Both filters were able to identify the size and the location of the damage clearly.

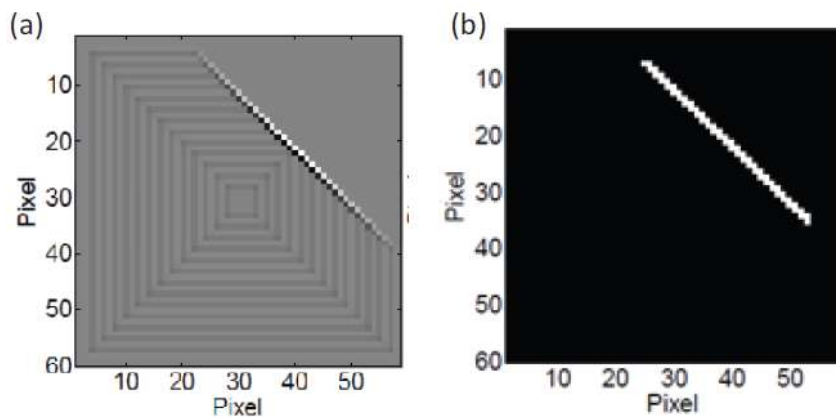


Figure 36: Calibrating simulation: a) Laplacian filter b) Robert's filter

3.2. SAMPLES' DESIGN

Accordingly, for the sake of studying the effectiveness of induction thermography technique in detecting corrosion defects inside automobile tires, our methodology relied on preparing samples of cured rubber (20 cm, 2cm, 1 cm.) wherein a corroded steel wire of 1.3 mm in diameter is located inside (Fig. 37).

This wire represents the outer surface of the **Tringle Tresse (TT), Cable Bead**. It is the steel wire that is tightly intertwined around a flexible heavy cord called core forming a cable bead (fig. 9). In this design, two wires are placed in the middle of cooked rubber. The first wire is pristine, playing the role of witness sample whereas the other is corroded with a known corrosion pattern. The wire and rubber compositions are shown in table 2 and 3 respectively (Kadhem, 2018). Once the preparation is done, samples were sent for inspection to assess the tool's effectiveness.

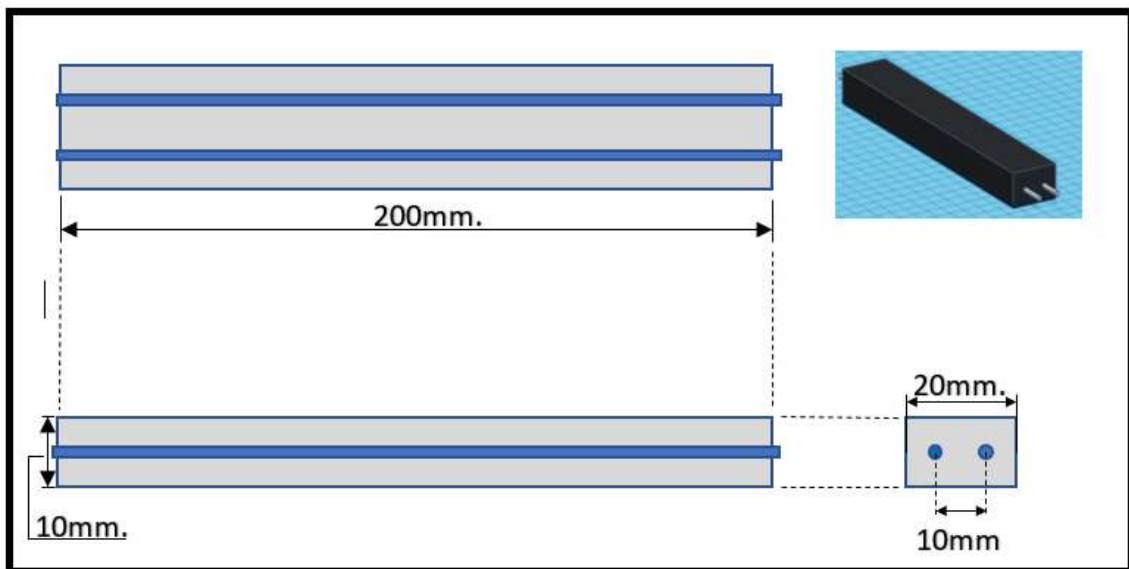


Figure 37: Isometric, top, front, and right side for the designed sample

Table 2: Bead wire chemical composition.

Elements	Percentage (%)
<i>C</i>	<i>0.72</i>
<i>Mn</i>	<i>0.6</i>
<i>Si</i>	<i>0.2</i>
<i>S</i>	<i>0.05</i>
<i>P</i>	<i>0.05</i>
<i>(S+P)</i>	<i>0.08</i>
<i>Ni</i>	<i>0.1</i>
<i>Cr</i>	<i>0.05</i>

Table 3: Raw materials of rubber compound

Compound	PPHR
<i>SMR 9720</i>	<i>72</i>
<i>SBR 1502</i>	<i>28</i>
<i>Whole Tyre Reclaim</i>	<i>0-70</i>
<i>PCTP-50</i>	<i>0.15</i>
<i>Zinc Oxide</i>	<i>5</i>
<i>Stearic Acid</i>	<i>4</i>
<i>Process Oil</i>	<i>12</i>
<i>Phenolic Tack Resin</i>	<i>6</i>
<i>N660 Black</i>	<i>140</i>
<i>6PPD</i>	<i>0.7</i>
<i>TMQ</i>	<i>0.6</i>
<i>Insol Sul:Oil (80:20)</i>	<i>0.1</i>
<i>MBS</i>	<i>6.27</i>
<i>CPT-100</i>	<i>1</i>
<i>Total</i>	<i>275-345</i>

The main challenge in such types of testing is the binary nature of results. It is either the corrosion is detected or not. Hence, to tackle the problem of direct negative

results when inspecting the complicated sample of bead section, three stages of testing conditions were introduced. The 1st level is the simplest, the 2nd is slightly more challenging, and the 3rd is the most complicated, which is an original part of real bead section. For further details, each level of complexity is described below:

1. **The Reference (level 1):** rectangular cured rubber wrapping two bead wires inside, the first is a clean intact wire and the other is a corroded one (all over the wire). The goal of this sample is to adjust the apparatuses' settings to develop the needed contrast between the corroded and intact wire, inevitably detecting corrosion.
2. **The Pattern (level 2):** rectangular cured rubber wrapping two bead wires as well, the first wire is clean intact, however, the other one is corroded in an alternative pattern. The goal of this sample is to assess the ability of the apparatuses to detect the given pattern of corrosion.
3. **The original (level 3):** which is nothing but an actual part of the tire bead. The most challenging sample due to its complex design and components (Future work).

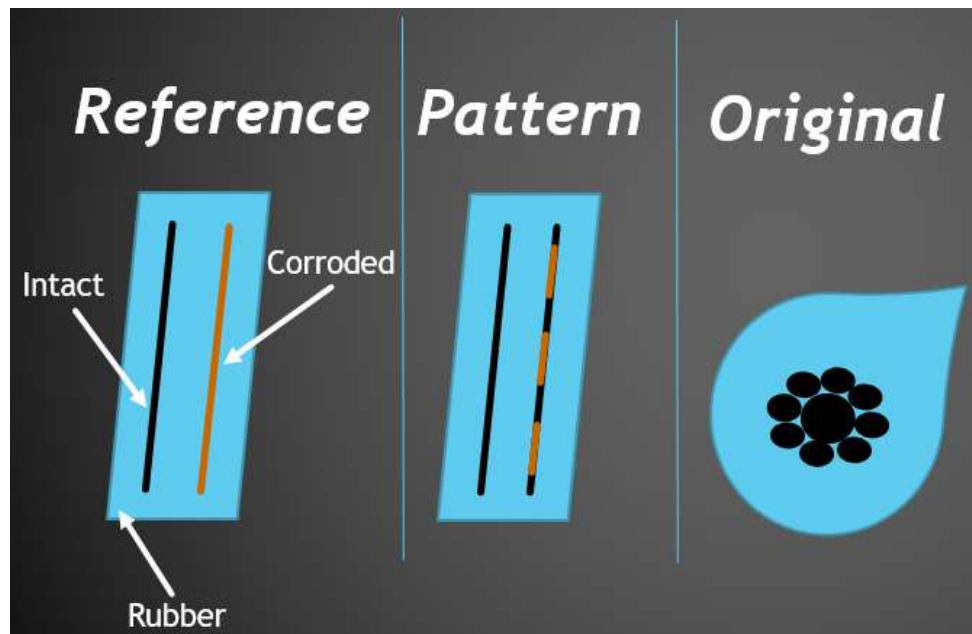


Figure 38: Animated sample types

3.3. EXPERIMENTAL PREPARATION

Type 1, Total corrosion: First trial included an attempt to test the wires susceptibility to corrosion. For this reason, wires were dipped in tap water for various periods of time (2, 5, 9, 12, 24 hours) as it can be seen in (fig. 39). After that, they were left to dry in a humid environment for 7 days. As a result, very thin layer of corrosion appeared on the surface, however, this layer was not stable or uniform, and it was easily flaking off.



Figure 39: Tringle wires dipped in water for various period.

For this reason, another corrosion procedure was adopted where tringle wire was wrapped in wet paper towel (salty water, 3.5%) and kept in a humid environment for 24 hours (~98% humidity environment) as it can be seen from figure 40. The corrosion surface in this procedure was more uniform, more stable and took only 24 hours for preparation.

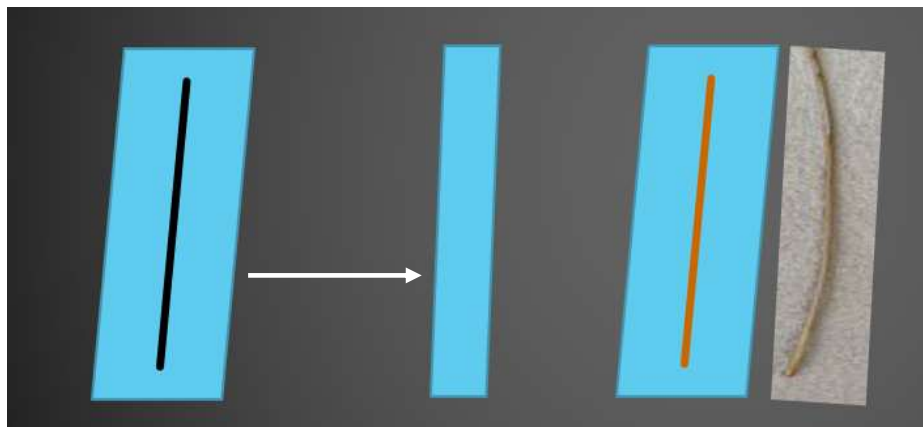


Figure 40: Full corrosion procedure

Type 2, Patterned corrosion: in this procedure, the 20 cm wire was prepared with 2cm of corroded surface and 3cm of clean surface, all over the length of the wire. Accordingly, some areas were sealed using Parafilm tape (blend of waxes and polyolefins) to protect it from corrosion, whereas the other areas were wrapped in wet paper towel (salty water, 3.5%) and kept in a humid environment for 24 hours (~98% humidity environment). Finally, the tape and the paper towel were removed, and the alternative corrosion was created as planned. The stages of this procedure can be seen in figure 41. For further elaboration for this type, another type of patterned corrosion was created. Mainly it has the same design in terms of dimensions and alternative corrosion over the length of the wire, however the corrosion quality is different. In the first type (type 2.0), the wire was directly wrapped in salty water after being sealed. In the newly created corrosion (type 2.1), the wire was dipped in HCl solution for 1 hour to remove the zinc from its surface. Such procedure will disable the sacrificial cathodic protection on the wire, hence severe corrosion will appear on its surface in comparison to type 2.0.

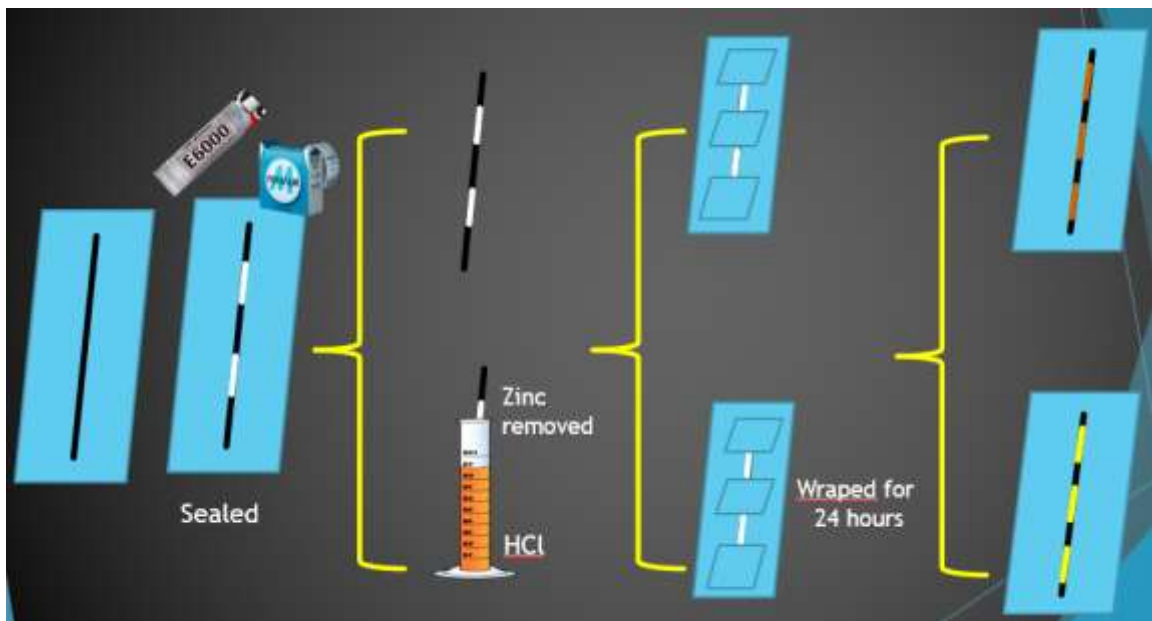


Figure 41: Full corrosion procedure

Figure 42 shows the actual procedure when corroding the wires. It starts by sealing some areas using parafilm tapes, then the wrapping towel and finally removing all the protective or corroded compounds from the wire.

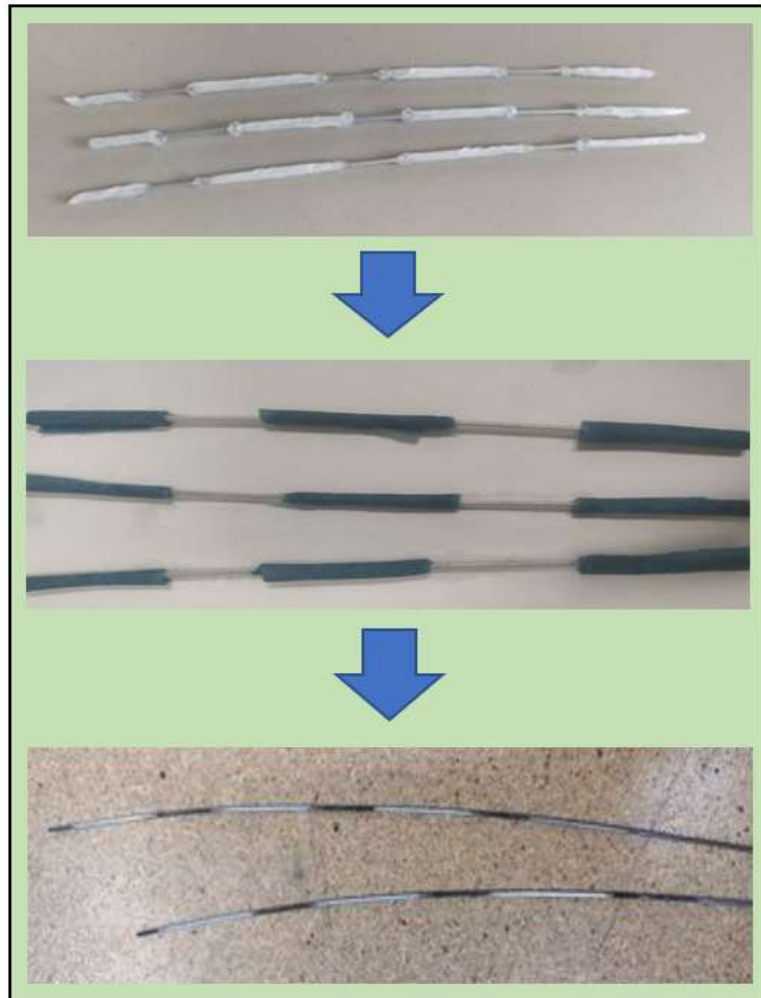


Figure 42: Pattern corrosion procedure

Once these two types of corrosion (total and pattern) are created, the corroded wire is cooked along with another pristine wire (witness sample) to eliminate any regularities that may rise due to cooking conditions or rubber thickness differences. Two rubber part are used to make each sample, thus wrapping the tringle wire from the upper and lower sides in the jig mold to produce a sample of 1 cm in total thickness (fig. 43).



Figure 43: Lower side strip of green rubber inside the jig mold before curing.

Samples were then cured for 10 minutes at 170 °C and the shape of type I/II (top and side views) after curing are shown in figure 44 and figure 45 respectively, whereas type III which is a bead section is shown in figure 46.



Figure 44: Sample top view



Figure 45: sample side view



Figure 46: Tire bead sample

For simplification, the diagram below depicts a briefing map to show the differences in these samples (fig. 47).

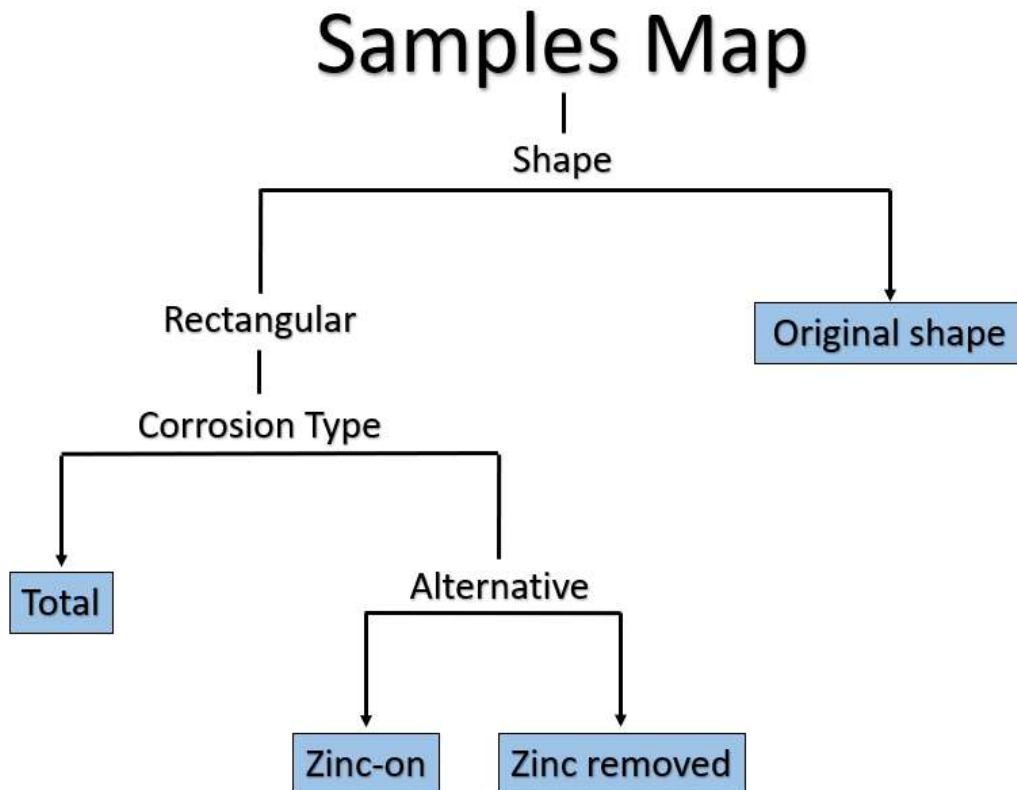






Figure 47: Samples flow chart according to shape and corrosion type.

To provide clearer idea on the difference between the 2 types of alternative samples, table 4 depicts the difference in corrosion severity on 2 cm corroded wire. It can be seen that for samples where zinc was completely removed, the surface was severely oxidised, whereas samples had had zinc left on still had some spots that are free corrosion. The second row in the table shows the area where clean and corroded regions meet.

Table 4: Corrosion severity between Zinc-on and Zinc-removed samples

	Zinc-on	Zinc removed
2cm. corroded area		
Corrosion-intact alternation edge		

Samples are as shown in figure 48: the code “R” represents the reference sample, number: 5 and 7 represents the zinc-on alternating sample (odd numbering), whereas number: 6 and 8 represents the zinc removed alternating samples (even numbering). Once the detection trials are successfully achieved on this basic level, we can proceed in the future work to the bead section of a tire- which has a wave shape (fig.49).



Figure 48: Prepared samples for testing



Figure 49: Bead section- wave shape

3.4. TESTING APPARATUSES

In order to provide higher successful outcomes during corrosion inspections, piloting experiment was conducted over the created samples. Then followed experiments were applied using planar induction coil, tesla coil and hand-made Helmholtz induction coil.

3.4.1. PLANAR INDUCTION COIL

It was composed of 3 main components (fig 50):

1. Eddy current generator (17- 18 kHz, resonant mode, 200 Watts).
2. IR camera: FLIR A655sc, Uncooled, 8-14 mm, 640 x 512 px.
3. Planar induction coil.

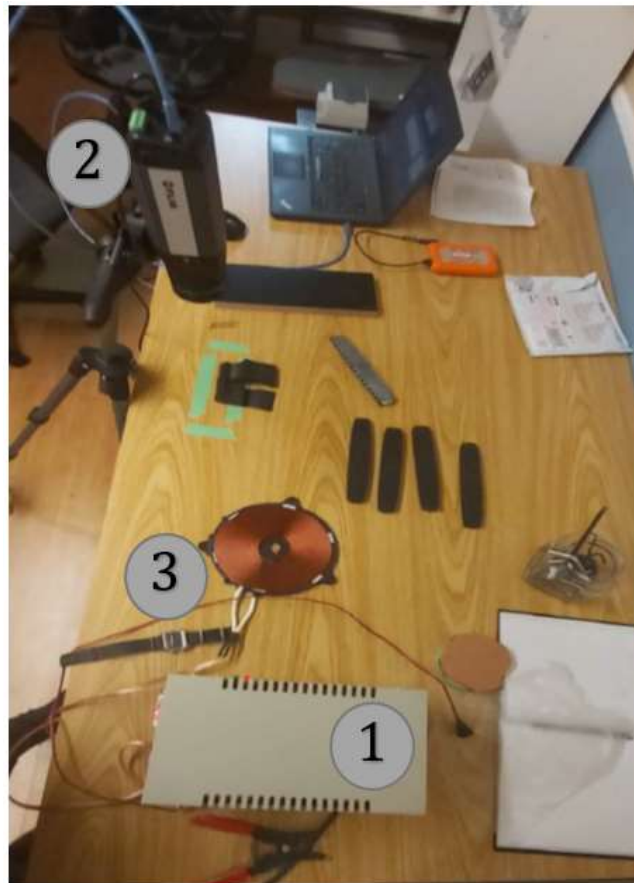


Figure 50: Planar Induction thermography basic setup

Samples were heated using the flat coil, for a period of 20 s; during this time the sample was moved continuously over the coil to ensure uniform heating as much as possible. Was power source was set to deliver 2000 W and the camera was placed 20 cm away from the sample to be inspected.

3.4.2. HELMHOLTZ COILS

In order to provide optimal uniformity of the magnetic field, handmade Helmholtz coils were used with the same power generator. The planar coil was substituted by two hand made smaller coils, in Helmholtz arrangement. Coils had a 6 cm diameter and five turns (fig. 51).

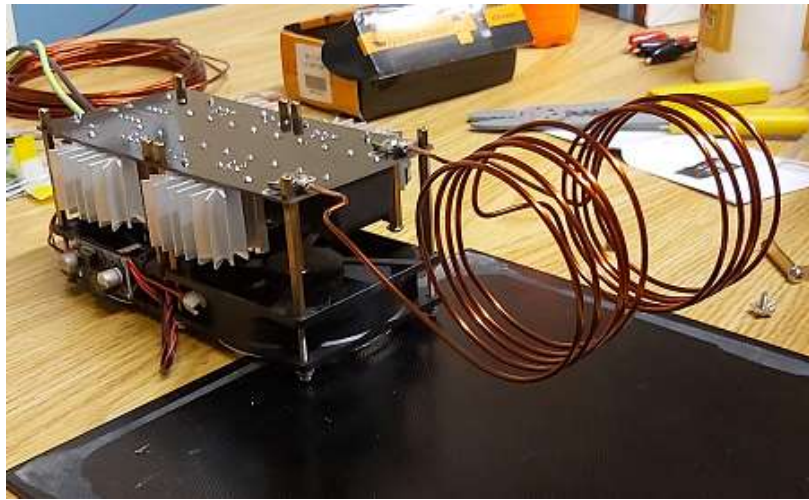


Figure 51: Hand-made Helmholtz induction coil.

3.4.3. TESLA COILS

Tesla coil was used as well (fig. 52), ih 1000 from SMITHERMA. Tesla coils offer many advantages over other setups, such as ease of use, safety and high output power. For example, it can operate with AC current using 110 V - 50 Hz with high output power with 1000 W.



Figure 52: SMITHERMA- ih 1000 tesla induction coil

3.5. SYSTEM SETUP

For each test, the specimen was fixed with plastic grips to ease the scan of the specimen. For each scanning point, few seconds sequences are recorded in order to capture enough information about the temperature distribution prior and after the release of the induction pulse. A 1000 w, 100 kHz Tesla coil was used to create a magnetic field necessary to heat the steel wires embedded in rubber. Heating was done in sections to allow for an increase in the scanning speed because the zone of interest associated with each scanning point is greater. The infrared images were recorded with a FLIR A655sc camera equipped with an amorphous silicon infrared detector and has a thermal sensitivity lower than 30 mK at room temperature. The full frame dimensions are 640 x 480 pixels, and the corresponding sampling frequency is 60 Hz. Thermal images were captured by FLIR Research Studio and sent to Matlab for analysis.

CHAPTER 4

RESULTS AND DISCUSSION

In this chapter, various experiments took place using different setup and apparatus. We started with piloting experiment to evaluate the reliability of the camera. Then results generated from planar coil were presented first followed by Helmholtz coil and finally by tesla coil.

4.1. PLANAR COIL

4.1.1. PILOTING RESULTS

To validate the effectiveness of the planar coil and the thermal camera, a piloting experiment was implemented. Two types of nails were used (thin and thick), and each type has two replicates, one was pristine and the other corroded. The chart below categorizes these four nails in terms of type and surface conditions. All nails were painted black to ensure the same thermal emissivity once subjected to the electromagnetic waves produced from the coil and the eddy current generator (fig. 53), (fig. 54).

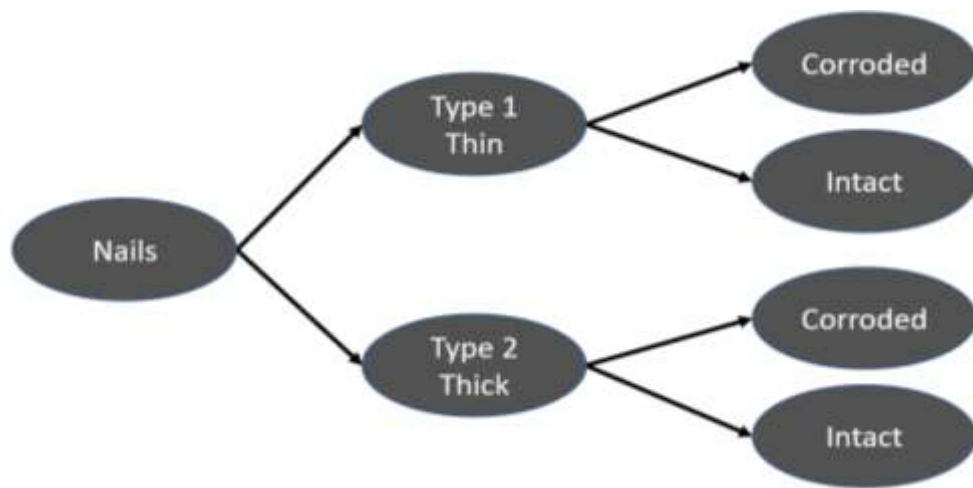


Figure 53: Piloting samples categorized based on type and surface conditions.

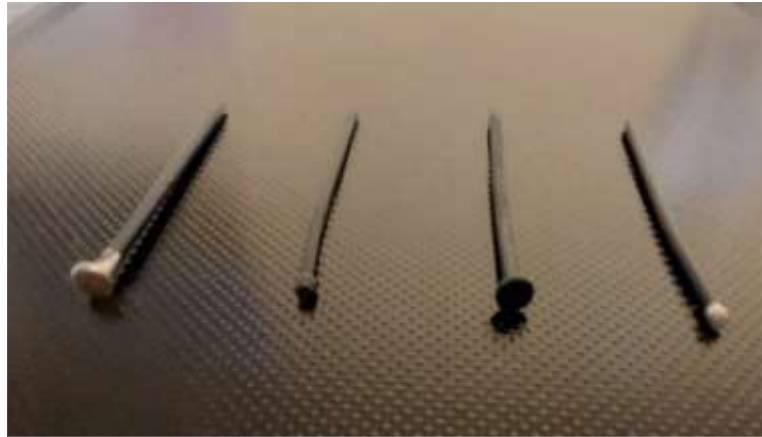


Figure 54: Thin and thick black painted nails.

Regardless of the shape, thin or thick, corroded nails assumed a higher temperature in comparison to clean nails. And this goes back most probably to the fact that intact surface can dissipate heat at higher rate than corroded surface. On the other hand, we can notice also that thinner nails heated up higher than thicker nails, which is expected due to the difference in volume between in the nails.

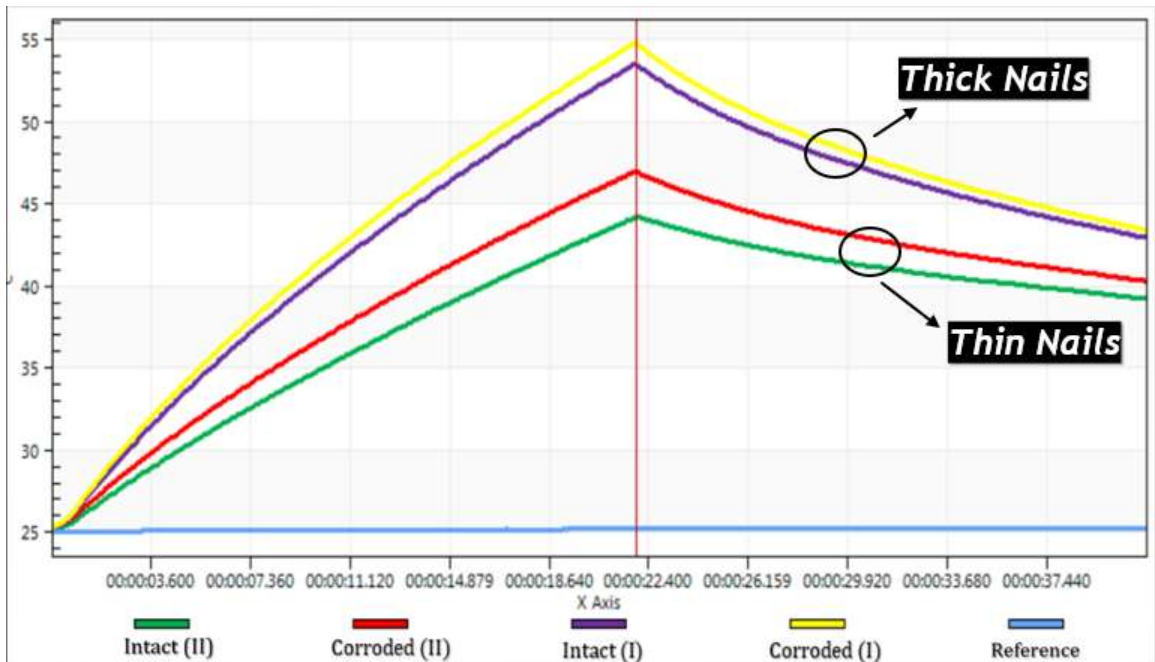


Figure 55: Nails surface temperature after being subjected to electromagnetic waves

4.1.2. SAMPLES' TESTING - HORIZONTAL DIRECTION

After validating, experiments were run over the 5 prepared samples (reference and 4 patterned samples). Accordingly, five thermographic images and charts were produced. Each one of them depicts the temperature evolution inside and the sample and illustrates the evolution of temperature -with respect to time- produced from the 2 inserted wires inside the sample, and from the rubber wire-free area.

Reference Sample

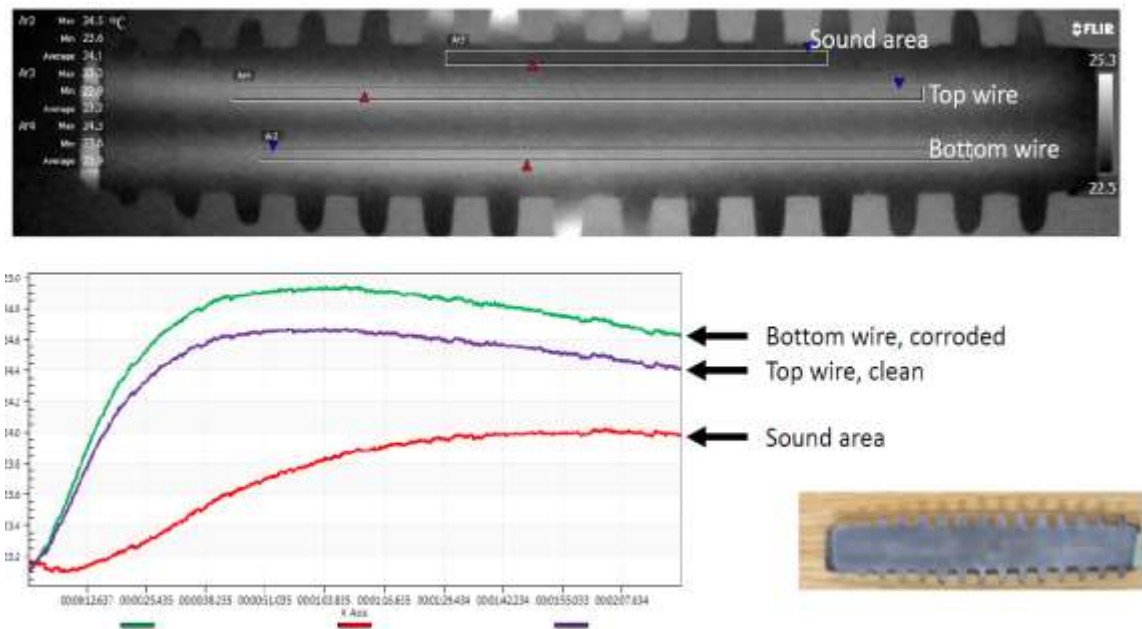


Figure 56: Reference Sample

Pattern Sample #5

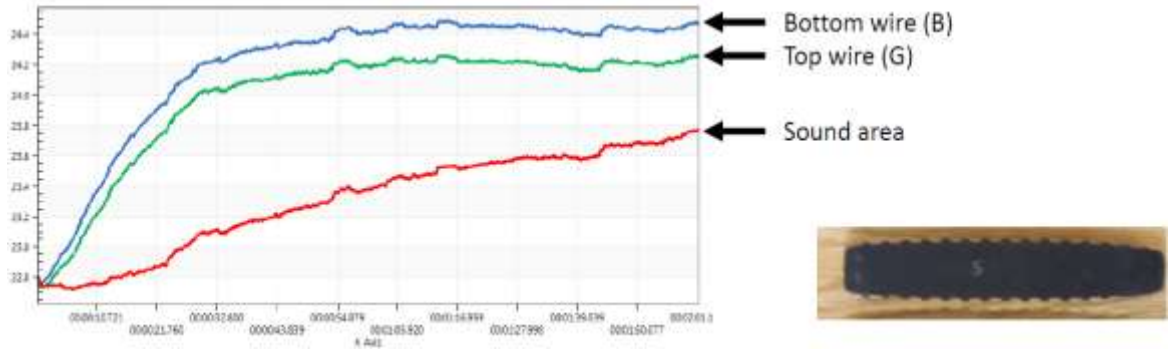
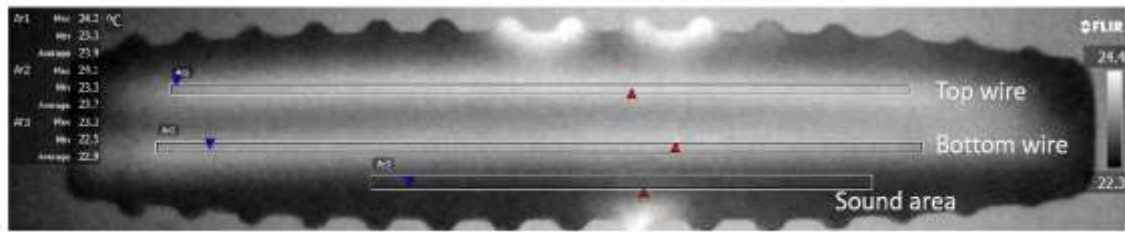


Figure 57: Pattern sample #5

Pattern Sample #6

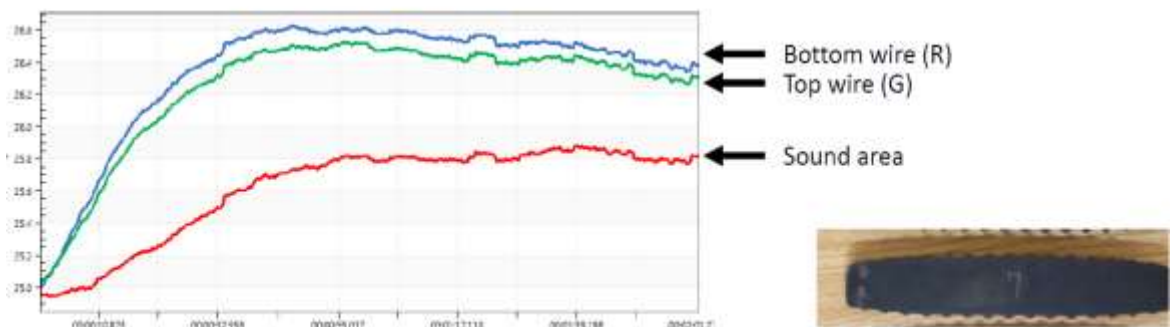
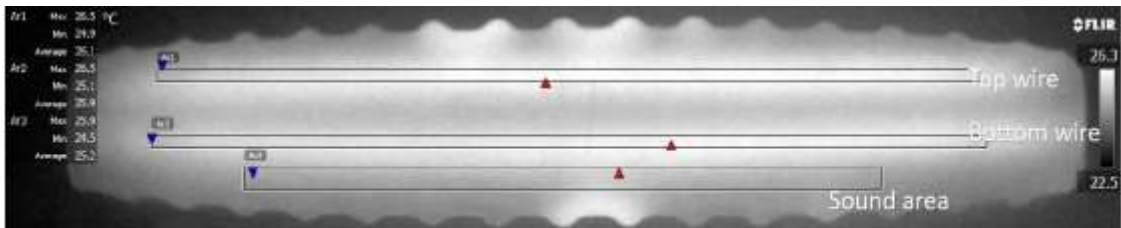


Figure 58: Pattern sample #6

Pattern Sample #7

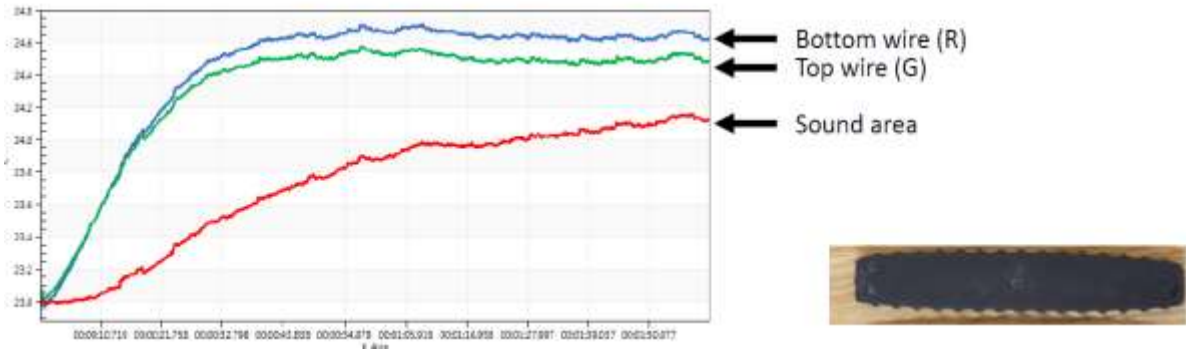
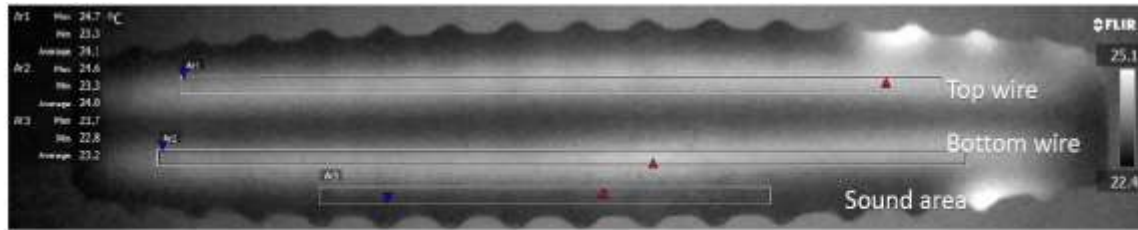


Figure 59: Pattern sample #7

Pattern Sample #8

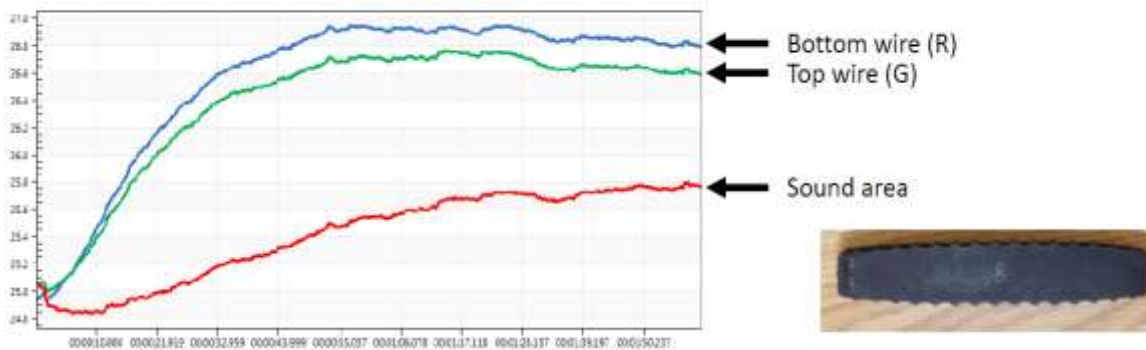
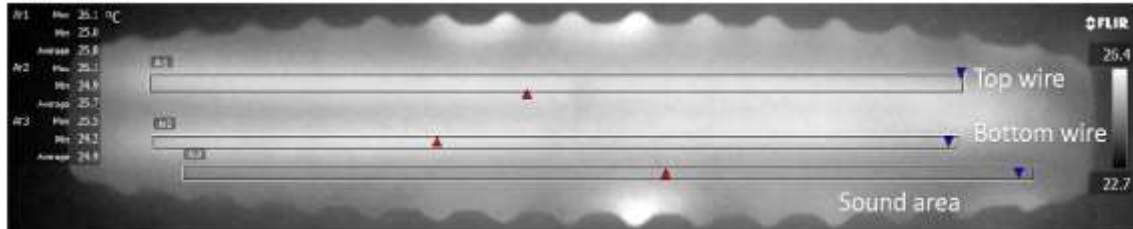


Figure 60: Pattern sample #8

The first observation made for the previous results (fig. 56, 57, 58, 59, 60), was that the temperature increased less than 2 °C in each case. This is at the surface of the sample; hence, we can safely assume that the temperature deep within the wires is way much higher. In practice, the thermographic images were not successful in detecting the corroded area, at least for the used implemented energy. Even on the level of the reference sample, there was no clear distinguishment between the corroded and pristine wire. On the other hand, the temperature evolution graphs were all consistent on showing approximately 0.5 degrees for the corroded wire with respect to the pristine wire, which is congruent with the fact of higher thermal reaction of the corroded surface with respect to the pristine surface. Such data can produce a preliminary beneficial result; however, it still lacks the ability to identify any localized corrosion or the pattern sequence of corrosion on the wire.

Vertical detection

In this attempt, we retried a few samples, and we retained the reference sample using the flat coil for 20 seconds of heating and moving the sample continuously over the coil to ensure the heating is as uniform as possible. As it can be seen from figure 61 below, the bottom wire (represented in Line 2) holds higher temperature when compared to the top wire (represented in Line 3).

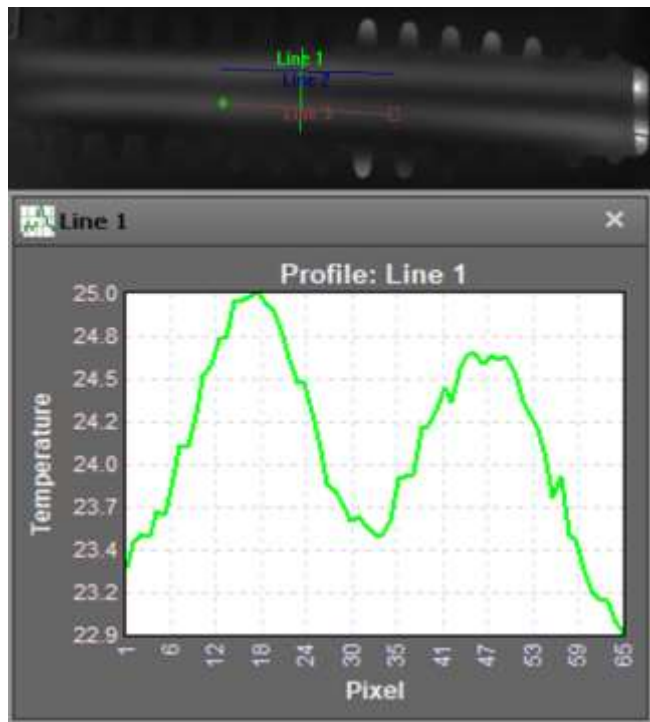


Figure 61: Side 1- top wire vs bottom wire.

4.3. HELMHOLTZ COIL

In order to have better control over the magnetic field and the ability to heat the sample more uniformly, a Helmholtz coil was employed. Testing with this setup was done on a piece of bead wire (fig. 62), 20 cm in length with 6.35 mm in diameter and 360° corroded circumference over 2 cm. Attempts to heat the sample and detect the corroded area was first done on the bare wire, and despite the size of the corroded area, results were disappointing as no contrast was seen between the corroded surface and the pristine one (fig. 63).



Figure 62: 2m of corroded circumference of bead wire

The temperature was raised up to 69.7°C, without successfully detecting the corroded region. This might be due to the number of turns and the rudimentary design and fabrication of this coil.

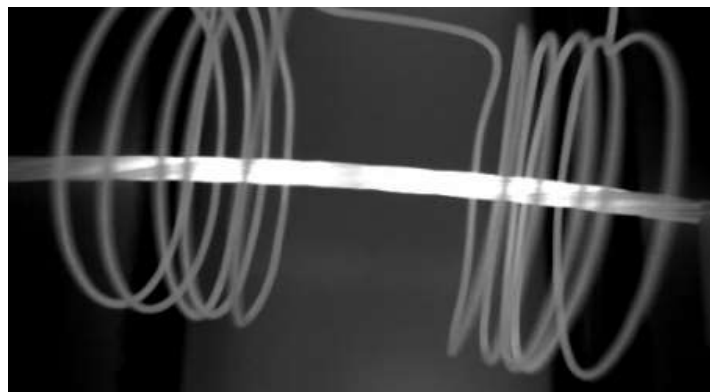


Figure 63: Corrosion detection using handmade Helmholtz setup

4.4. TESLA COIL

After a series of testing that did not net much in term of corrosion detection. A mini-inductor, with a Tesla coil was employed. A Tesla coil is inexpensive, can be made to accommodate samples of different shapes and sizes. However, one of its major shortcomings is the ability to cast a uniform magnetic field and that might render detection difficult, when it comes to heavily insulated wires. For this reason, employing an image processing algorithm becomes paramount if detection had to be successful.

4.4.1. THE ALGORITHM

The next two sections recall the principal steps computed by the algorithm for the image processing. Two work environments were used: the FLIR Research studio professional for the acquisition and exportation of the data and the Matlab software for the analysis.

FLIR Research Studio

Once the system setup is prepared, the camera must be connected to the computer through a firewire cable. The FLIR Research Studio must be opened and, before starting the data acquisitions, few object parameters must be set. Instructions for their evaluation are showed in Table 5

Table 5: Object parameters, setting instruction and unit of measurement

Parameters	Description
Reflected Temperature (°C)	<p>The reflected temperature is the apparent temperature recorded on the sample surface due to the reflection of some radiation coming from the surrounding. This radiation can alter and even invalidate the measurement. Thus, for a correct acquisition, it is necessary to take it into account. The FLIR User’s manual provides an easy method to estimate this reflected temperature. It briefly states:</p> <ul style="list-style-type: none"> • crumble up a large piece of aluminum foil • uncrumble it and put it in front of the sample facing the camera • set the emissivity to 1 and measure the temperature • Set this value as reflected temperature in the camera settings
Emissivity	<p>For accurate measurements, the emissivity is set according to the following:</p> <ul style="list-style-type: none"> • attach a piece of electrical tape of known emissivity (usually around 0.97) onto the specimen • set the emissivity mentioned above in the camera device, focus and write down the tape temperature assuming that the tape and the specimen are in condition of thermal equilibrium, point now to the sample surface and change the emissivity setting until the camera displays the same temperature as the one previously recorded.
Humidity	<p>The presence of water into the atmosphere has effect in the absorption of the radiation emitted by the specimen. Anyway, if no humidity instruments are available, it is possible to set the value at 50%.</p>
Distance from object (m)	<p>The distance between the specimen and the camera lens is doable easily by means of a ruler. See the technical data sheet for the camera lens in order to respect the minimum focal length.</p>
Atmosphere temperature (°C)	<p>The temperature of the atmosphere normally has not a big influence, assuming of working in standard conditions (-20 to 400 °C). The estimation is very simple and can be done using a common thermometer or reading the room thermostat display.</p>

Matlab environment

The data analysis and the image processing were performed using Matlab. This was done by first importing the data set from the video that was acquired from the thermal camera. Following this, four statistical parameters for each frame of the

video: average temperature of the entire frame, standard deviation, skewness, and kurtosis coefficient, were computed. Then a reference frame was created by computing the 2D mean of all the “cold” frames. A “cold frame” is a video frame before the heating starts. This is done with the aim of reducing the thermal noise and creating a reference frame representing the background temperature distribution in normal condition. Once the reference frame is created, the 2D mean between the different acquisitions for each frame there after is calculated and the correlation coefficient comparing each frame to the reference is computed.

4.4.2. TESTING USING TESLA COIL

For all experiments, the parameters were set according to the procedure mentioned earlier and are shown in in table 6.

Table 6: Tesla coil setup parameters

Parameters	Value
Reflected temperature (°C)	22
Emissivity	0.95
Humidity	50%
Distance (m)	0.2
Atmospheric temperature (°C)	22
Acquisition mode	Multi-frame
Frames per acquisition(x1000)	25
Frame rate	60
Frame resolution	640x480

4.4.3. DETECTION ON BARE WIRES

At first, two videos were created. One by averaging the acquisition associated with 20 pristine areas of a bare steel wire, free of corrosion, over three 10 s heating cycles (figure 64 and 65). The other was created by comparing the acquisition associated with a pristine area and a corroded one (figure 66 and 67). As can be seen from figure 64 and 65, the average temperature from the three heating cycles differs slightly. As rubber is not playing any role of slowing down the cooling of the wires, this is most likely due to the magnetic field not being completely uniform, the nature of the wire and the presence of impurities to name a few. Slight variations of that sort are not problematic when inspecting wires or pipes that are bare or covered with a thin layer of coating or paint. However, they could present a significant challenge when inspecting wires or pipes that are covered with thick insulation. Hence, another video was generated to compare the average heating and cooling rate between a pristine area and a corroded one. The results are presented in figures 66 and 67, where one can see that the temperature gradient for the corroded area is shallower than that of the pristine one indicating a slower cooling rate for the area covered by corrosion. This is expected as surface corrosion act as an insulator, trapping the heat and keeping the corroded area at a temperature higher than the rest of the wire. Relying on the temperature or cooling rate alone might be sufficient to yield true positives and pinpoint corroded areas in bare wires. However, if a wire is covered by a think layer of rubber, which is an excellent insulator, recording a true positive is not as straight forward and there is a need to compare more than temperatures or temperature gradients.



Figure 64: averaging the acquisition associated with 20 pristine areas of a bare steel wire

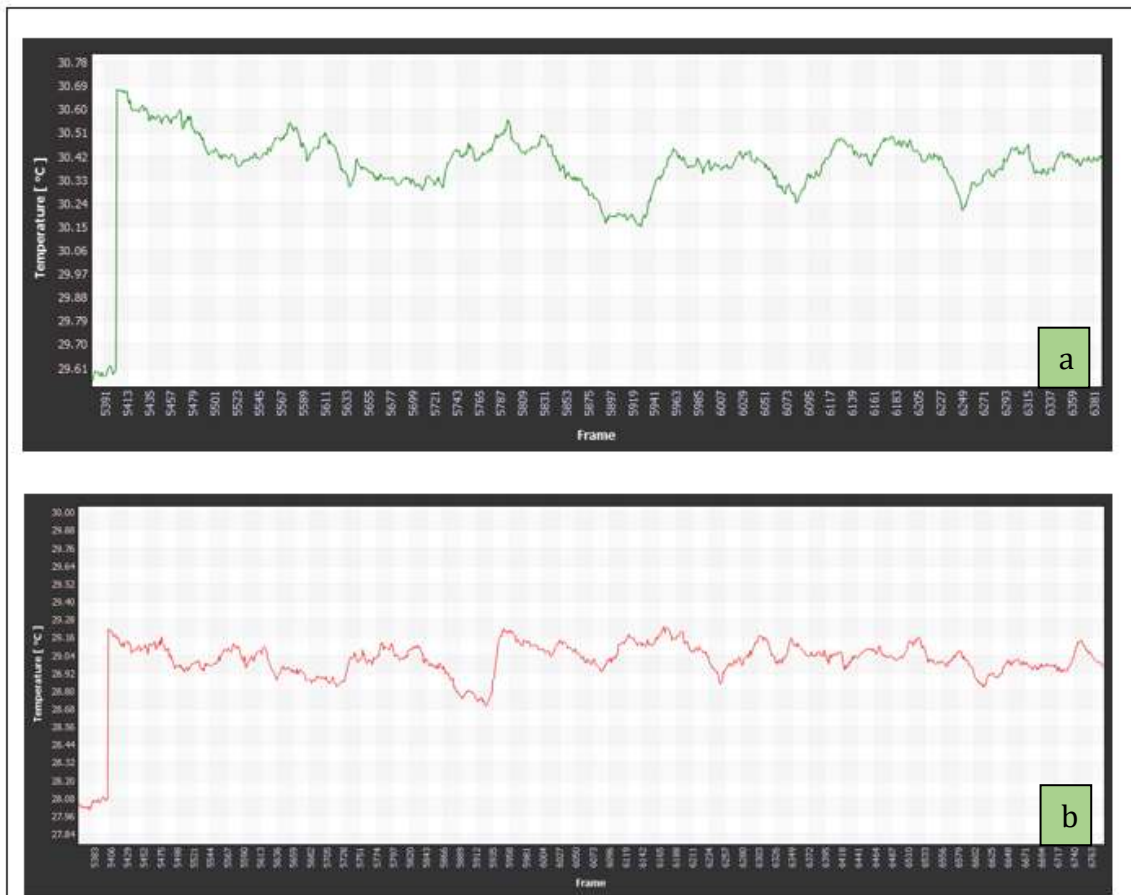


Figure 65: Temperature evolution with respect of time for a bare steel wire, free of corrosion: a) heating cycle #1; b) heating cycle #2.



Figure 66: Averaging the acquisition associated with a pristine and one steel wire

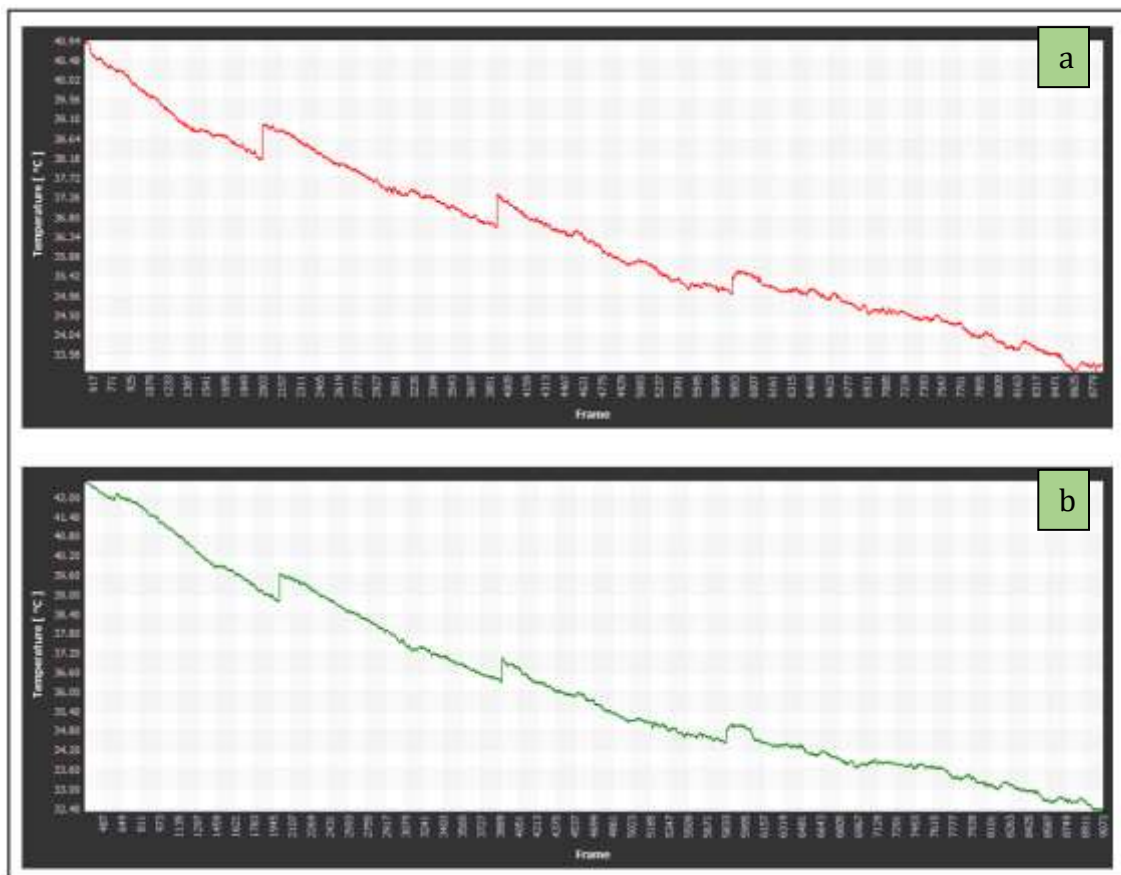


Figure 67: Temperature evolution with respect of time for a mix of pristine of corroded areas of a bare steel wire, free of corrosion: a) heating cycle #1; b) heating cycle #2

4.4.4. DETECTION ON EMBEDDED WIRES

For these experiments, the mini-induction heater was used to heat the embedded wires in the reference sample. The heating time was set to 10 s. The sampling frequency of IR camera was set to 60 Hz, and the sampling interval was set to 5 ms. Figure 68 (a) shows the thermal image of the reference sample right after heating is removed. Along with wire the increasing temperature reading between figure a and b, it's clear that the corroded wire reached a higher temperature than the pristine one. However, as time increases, the lateral blur effect and heat flow to the centre of the sample severely affect the detectability of corrosion. In Figure 69 the temperature started to decrease between (a) and (b), and the details of the corrosion area is polluted by non-uniform heating effect, most likely caused by coil shape, the uniformity of the magnetic field, the non uniform thickness of the rubber and the heat flow to the centre of the sample.

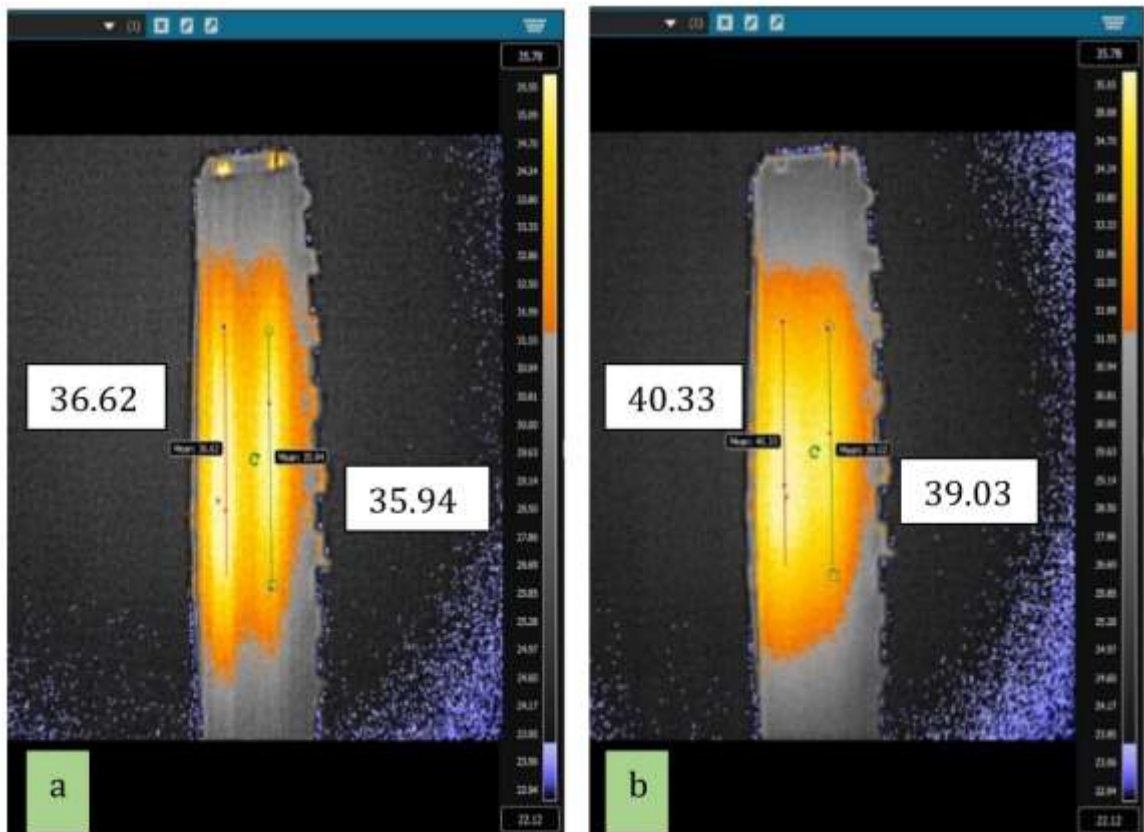


Figure 68: Thermal image sequence of the reference sample right after heating a) right after heating is removed, b

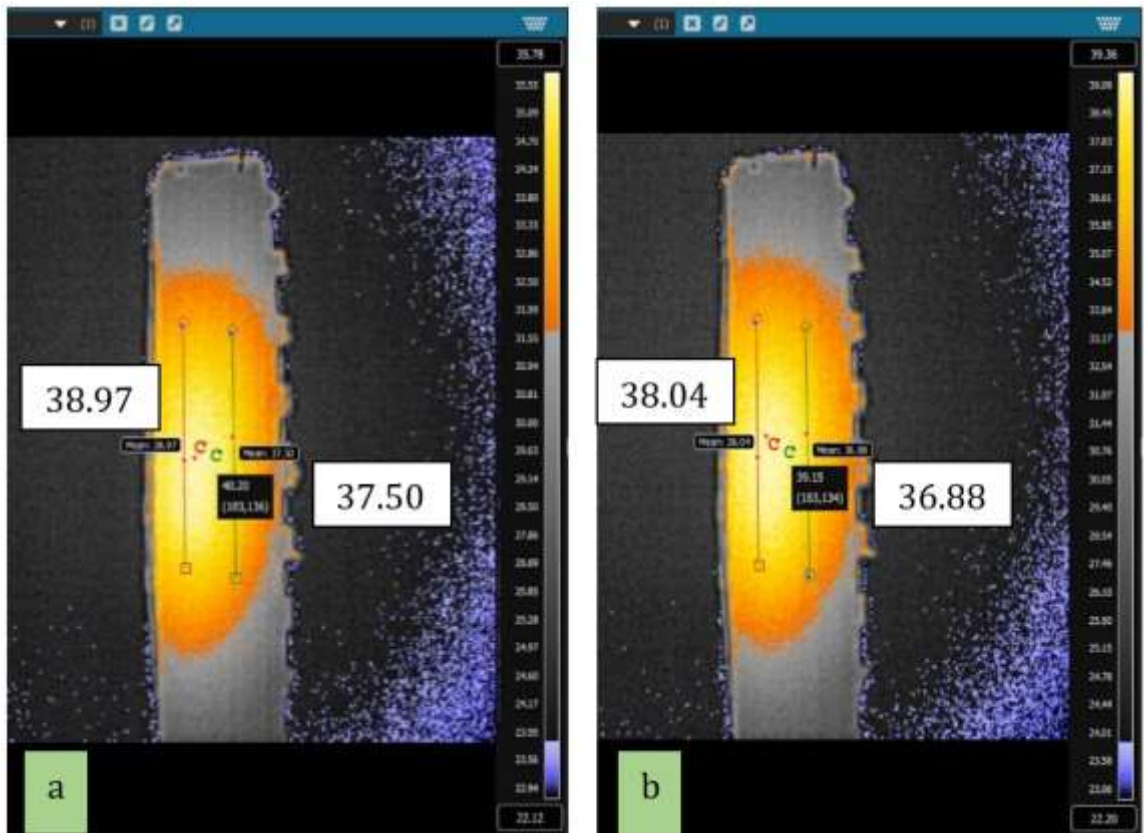


Figure 69: Thermal image sequence of the reference sample in cooling mode

Fig. 70 (a) shows the temperature for 20 points. Ten are located on the corroded embedded wire and ten on the embedded pristine wire. Figure 70(b) was taken with the camera behind the sample, thus the flipped location of the wires. All points have the same distance from the coil and their temperature increases for about 100s after heating is removed, then start decreasing. One would expect that the temperature of the corroded wire to be higher than that of the pristine one, but as can be seen from figure 70 (a) and (b) this is not the case and temperature of the points seem to have a mind of its own. This is difficult to explain but could be due the differences between physical parameters between the points, from the nature and thickness of the corrosion by product, the thickness of the rubber, the humidity, and the shape of the coil, even though all care was taken to ensure a uniform magnetic field.

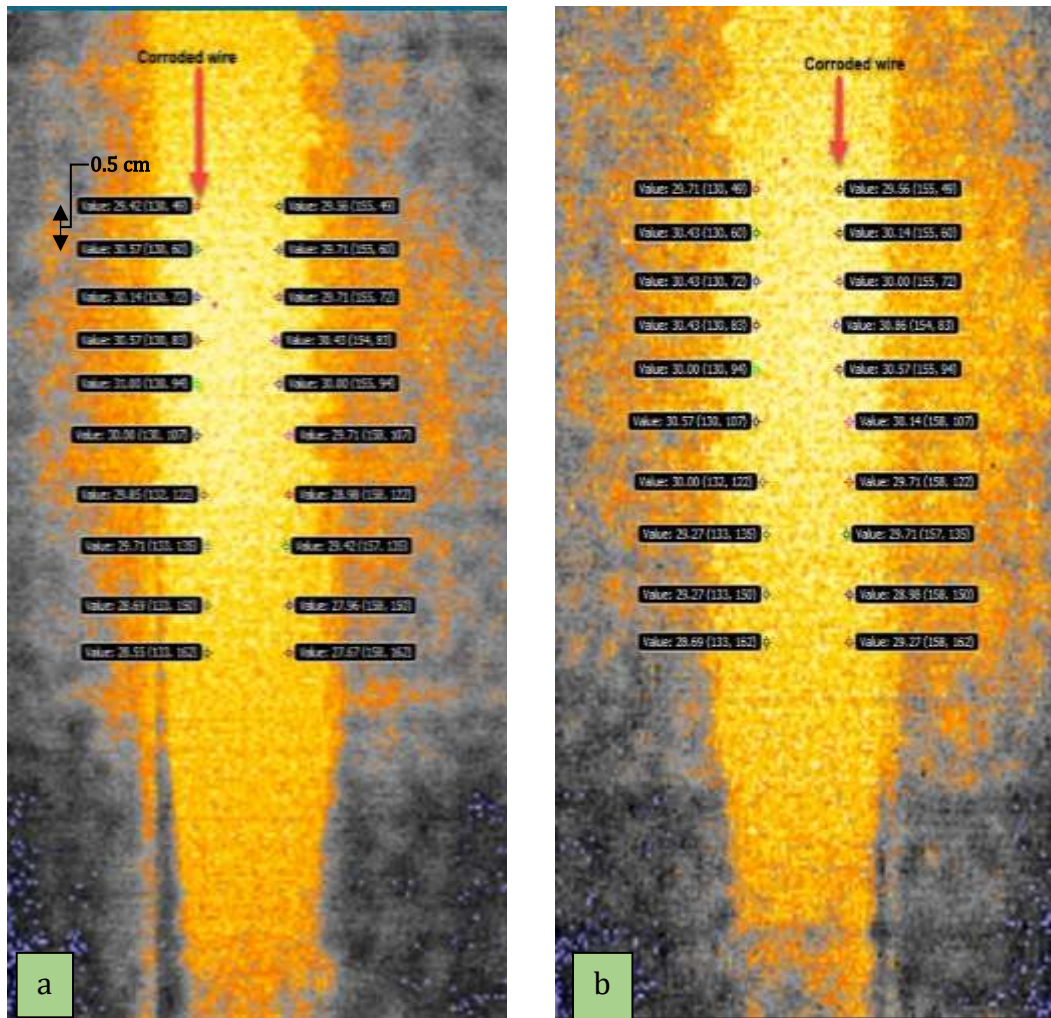


Figure 70: Respective comparative points of temperature: a) front; b) back

To overcome these challenges and be able to pinpoint the corroded regions, for each acquired point in the baseline video, which consisted of 105 frames, the mean temperature, variance, skewness, and kurtosis of the frames were computed.

Figures 71-74 shows these variations as a function of the frame number for an acquisition associated with a pristine zone. When compared to the average temperature, which is a parameter widely used in active and passive thermographic methods, the three statistical parameters denote a much sharper increase immediately after the application of the heat (frame 18). In particular, the skewness,

which measures the asymmetry of a data set around the data mean and is computed as:

$$\gamma = \frac{1}{N} \frac{\sum_{i=1}^N (x_i - \bar{x})^3}{\sigma^3}$$

where N is the number of elements of the distribution \bar{x} is the mean and σ the estimated standard deviation.

Negative values represent data that are skewed leftward with respect to the mean. Positive values represent data that are skewed rightward, as it happens in all the laser spot thermography tests for the local increase of temperature. The skewness coefficient of the normal distribution (or any perfectly symmetric distribution) is zero. Thus, positive skewness values are expected. The kurtosis is a measure of how outlier-prone a distribution is, and it is defined as:

$$K = \frac{1}{N} \frac{\sum_{i=1}^N (x_i - \bar{x})^4}{\sigma^4} - 3$$

The kurtosis of the normal distribution is equal to three. Distributions that are less outlier-prone have kurtosis lower than three. Conversely, distributions that are more outlier-prone than the normal distribution have kurtosis greater than three, as the present situation has. For each scanning point, the frame with the largest skewness and kurtosis is picked and processed by using the image processing toolbox in MatLab.

Figure 75 shows the correlation coefficient associated with the 40 acquisition points (All damage points are then compared to the points in the baseline frame. It shows a clear difference between pristine and corroded areas and there is a threshold level at 0.966. Correlation coefficients that fall below the threshold, warn about the possible presence of corrosion. Thus, an algorithm that compares a baseline image

or frame to a test one should not be impaired by the non-uniform heating, heat flow, heterogenous corrosion by product and inconsistent rubber thickness.

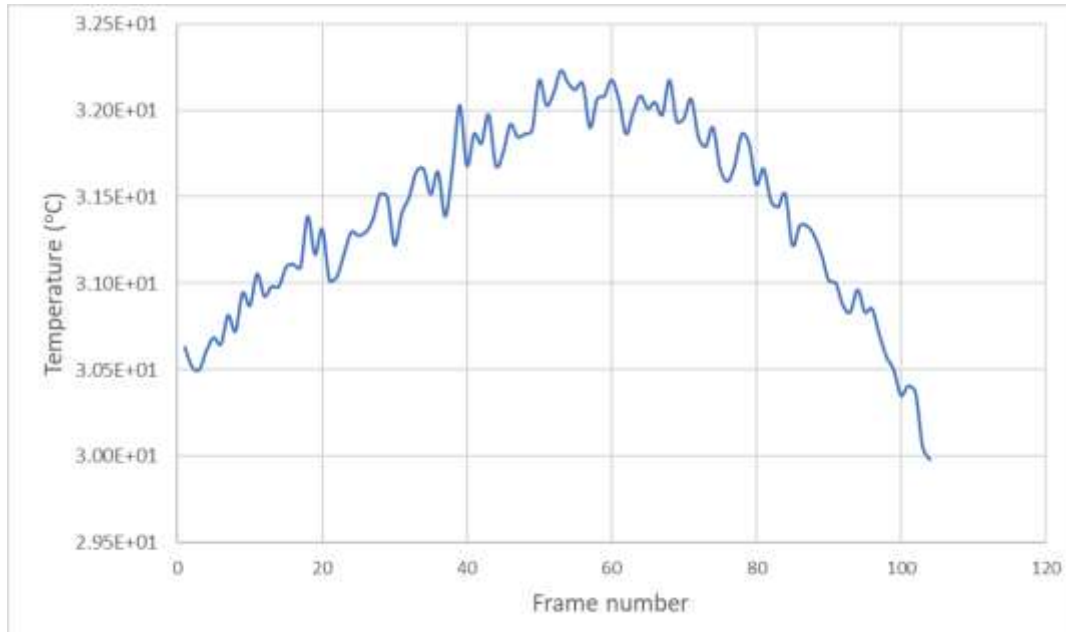


Figure 71: Average temperature

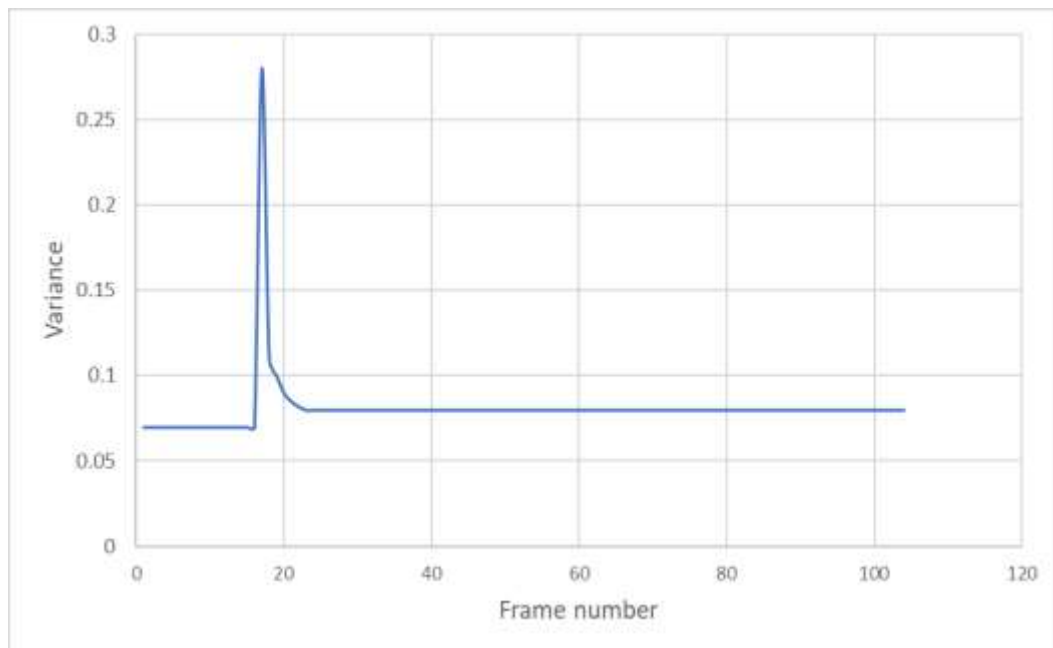


Figure 72: Variance

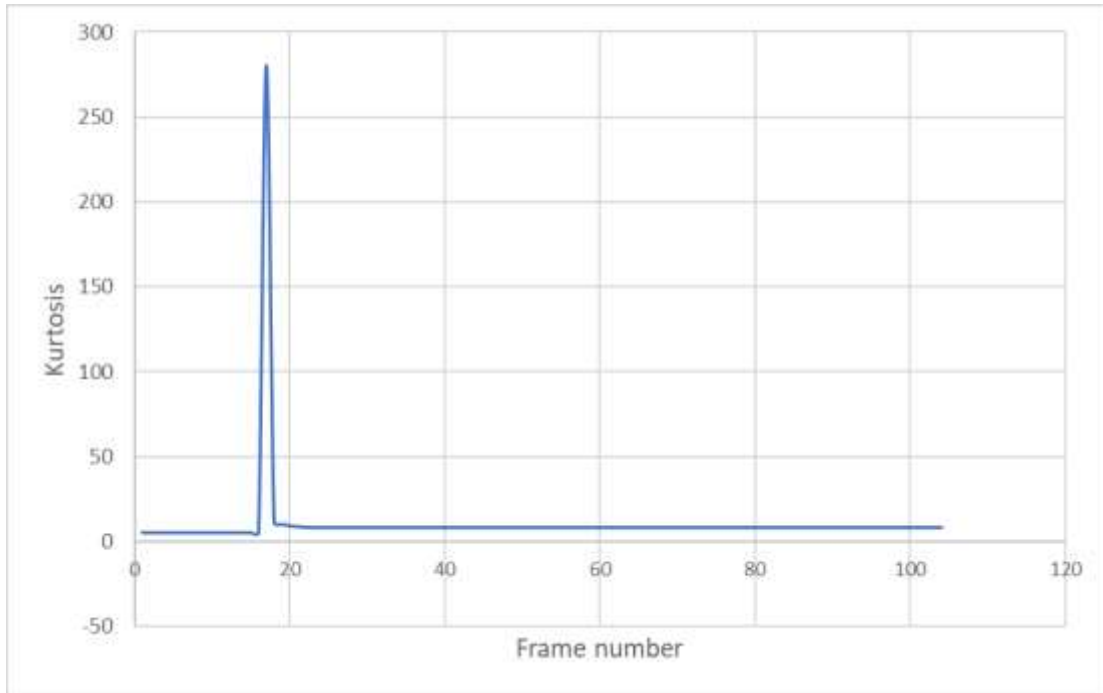


Figure 74: Kurtosis

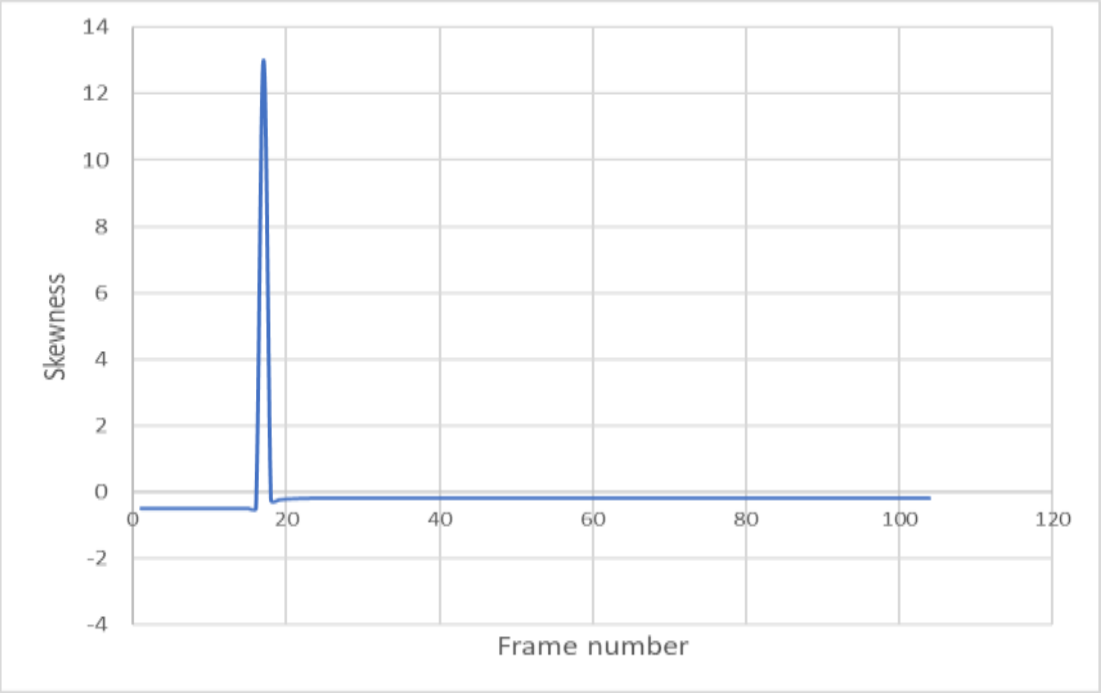


Figure 73: Skewness

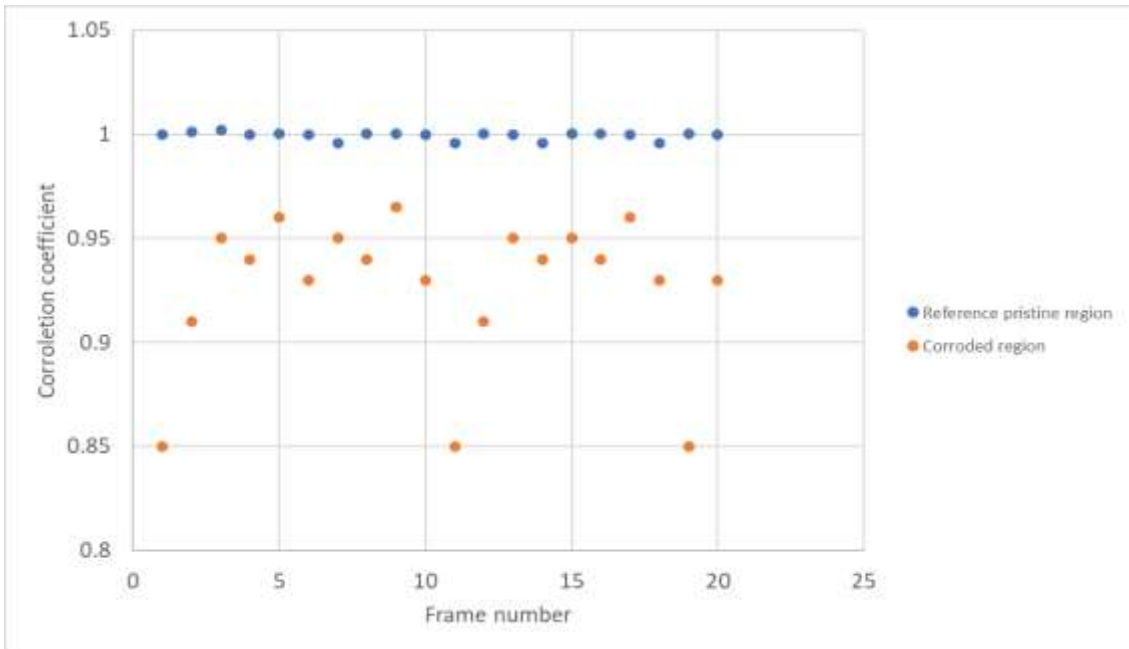


Figure 75: Correlation coefficient associated with the 40 acquisition points

Validation of the corrosion detection algorithm using plain steel wires embedded in rubber

In order to validate the corrosion detection algorithm eight points were used to acquire data from sample #7 (left wire has alternate corroded regions, right wire is pristine). Four acquisition points were placed on the corroded wire (a,b,c,d) and four on the pristine wire (e,f,g,h). Point “a” on the corroded wire is on a pristine region. Both wires were heated for 5 s, and data was acquired over 8000 frames. The data was then processed through a simple temperature analyzing algorithm and the results are shown in figure 76. Ideally, one would expect points b, c, d to be hotter than the rest of the acquisition points. This is simply due to the corrosion product trapping the heat, but as can be seen this is far from what was expected and most likely due to the shape of the coil, the nature of the corrosion product, manufacturing processes and the nature of the rubber and its thickness, to name a few.

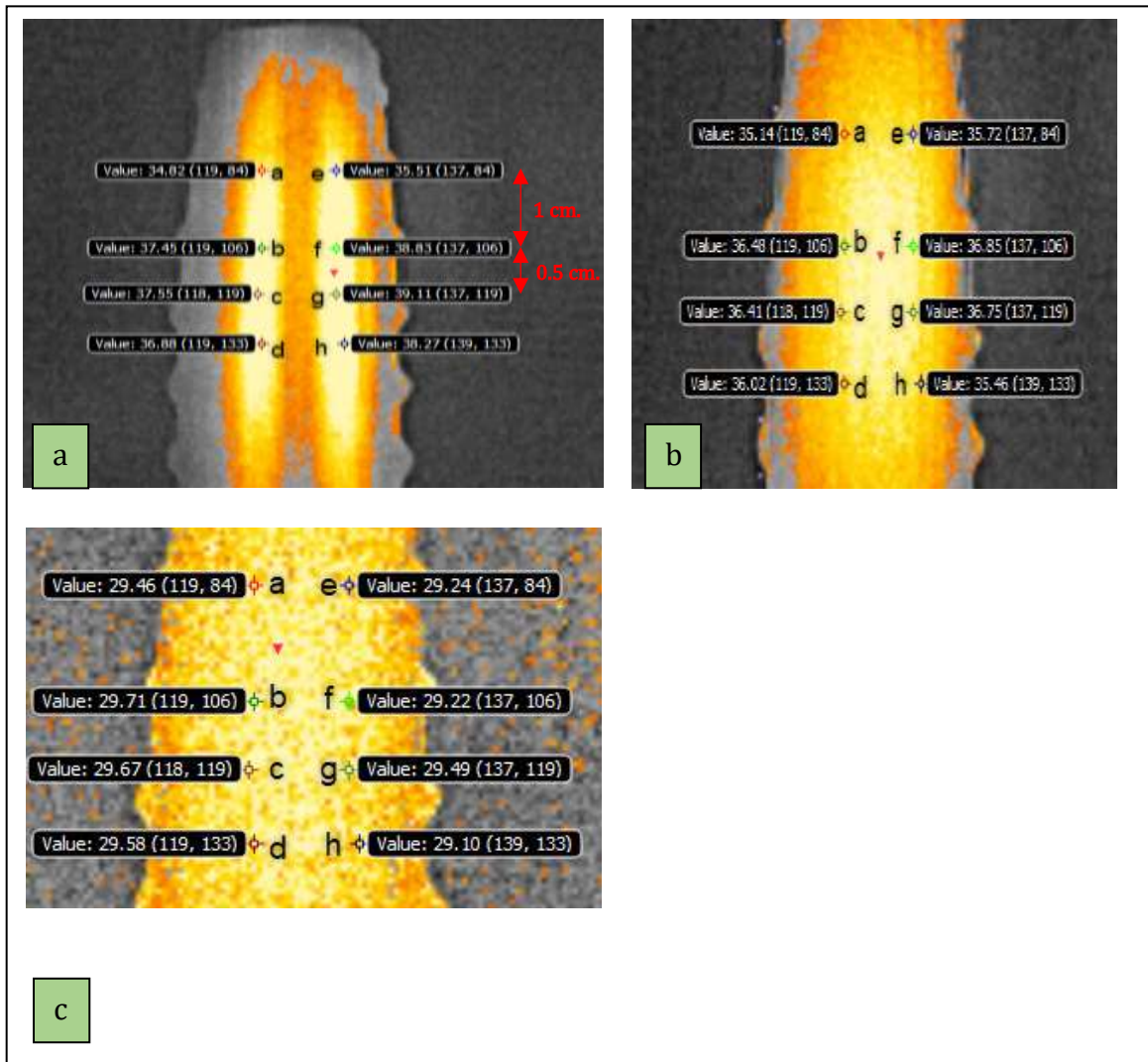


Figure 76: Thermal image of sample 7 processed using a simple temperature analyzing algorithm (a) right after heating, (b) 100 s after heating, (c) 300 s after heating (Corroded wire on the left)

However, processing the data using the proposed algorithm yield the expected results and that can be seen in figure 77. This was done by first calculating a correlation coefficient by comparing the three statistical parameters (skewness, kurtosis and variance) associated with the eight pixels in the “cold” reference frame to parameters of the same eight pixels in a sequence of frames right after heating is removes. From the correlation coefficient one can see that points b, c and d are suspect as their values fall below the threshold of 0.9776. Whereas all the other points, even “a” has a value very close to 1, as seen in figure 78. Once the suspected

pixels are pinpointed, the three statistical parameters in all subsequent frames are then subtracted from the parameters calculated in the reference frame. They are then converted to digital signals, which is, in turn, converted to radiance, then temperature using FLIR Research Studio.

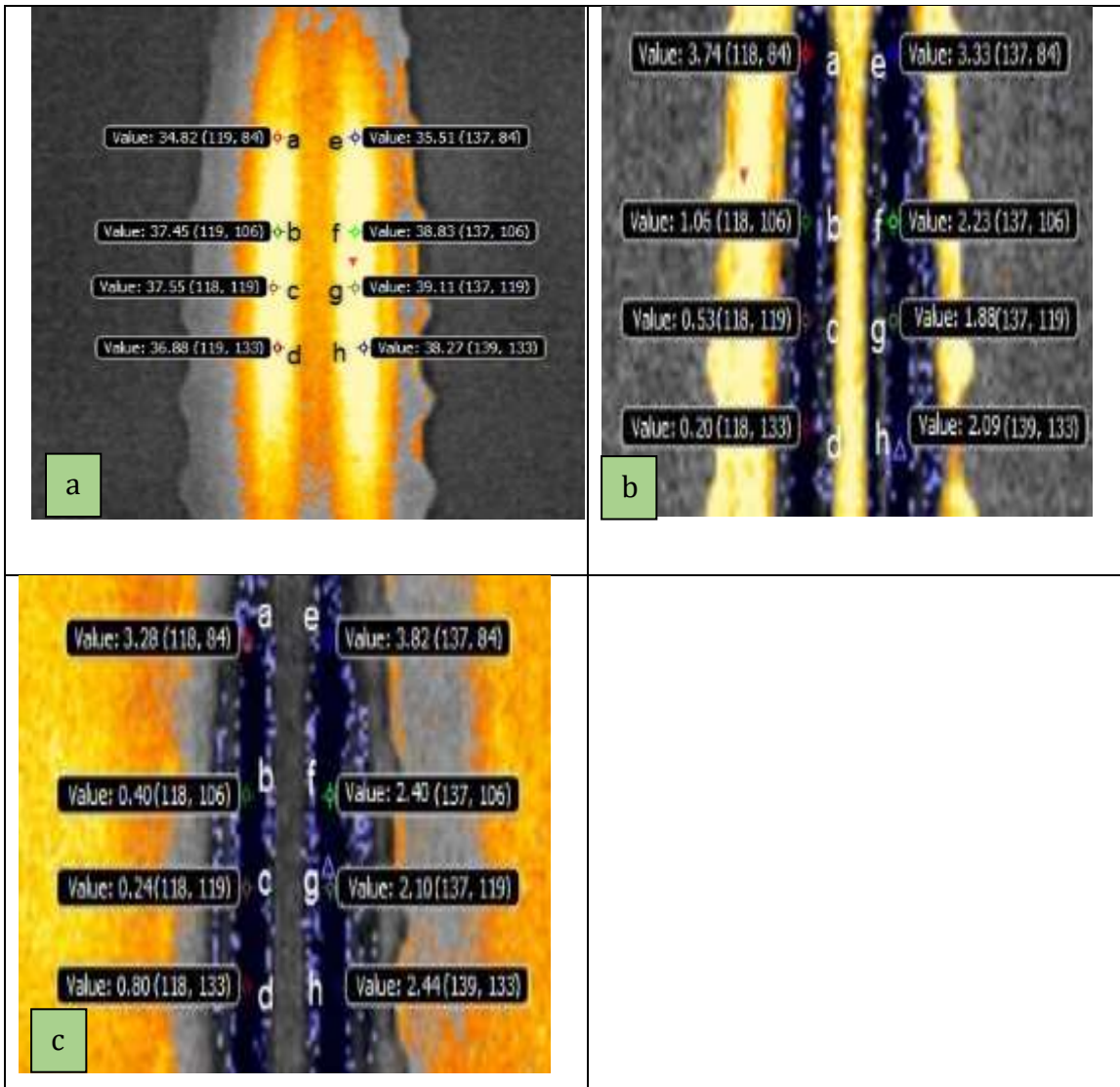


Figure 77: Processing the data using the proposed algorithm (corroded wire on the left)

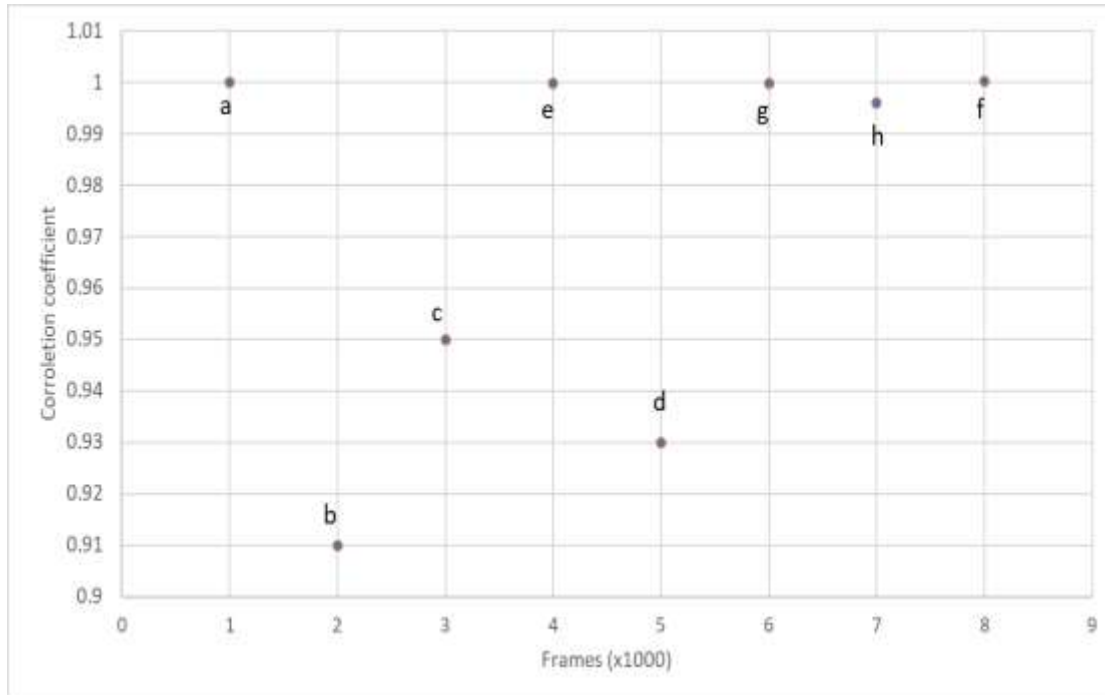


Figure 78: Correlation coefficient associated with the acquisition points on sample 7

Validation of the corrosion detection algorithm using galvanized steel wires embedded in rubber

As tringles embedded in tires are usually galvanized, there is also a need to validate the algorithm on samples containing galvanized steel wires, both corroded and pristine (i.e sample 8). For these experiments eight points were used to acquire data (left wire has alternate corroded regions, right wire is pristine). Four points on the corroded wire (a,b,c,d) and four on the pristine wire (e,f,g,h) Point “a” on the corroded wire is on a pristine galvanized region. Both wires were heated for 5 s, and data was acquired over 8000 frames. The data was then processed through a simple temperature analyzing algorithm and the results are shown in figure 79. Ideally, one would expect points b, c, d to be hotter than the rest of the acquisition points. This is simply due to the corrosion product trapping the heat, but as can be seen this is far from what was expected and most likely due to the shape of the coil, the nature of the

corrosion product, manufacturing processes and the nature of the rubber and its thickness, to name a few.

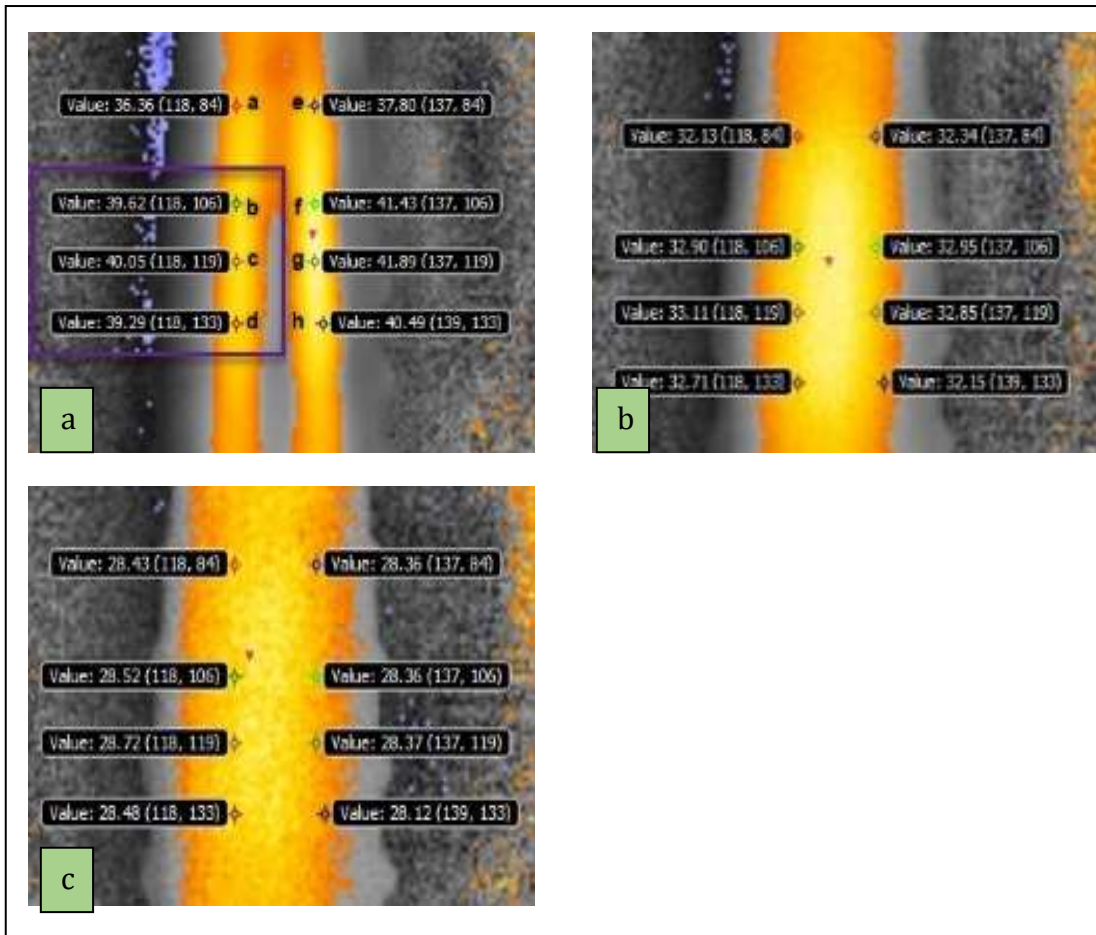


Figure 79: Thermal image of sample 8 processed using a simple temperature analyzing algorithm (a) right after heating, (b) 100 s after heating, (c) 300 s after heating (Corroded wire on the left)

However, processing the data using the algorithm mentioned previously yield the expected results and that can be seen in figure 80. For the correlation coefficient one can see that points b, c and d are suspect as their values fall below the threshold of 0.9777. Whereas all the other points, even “a” has a value very close to 1, as seen in figure 81.

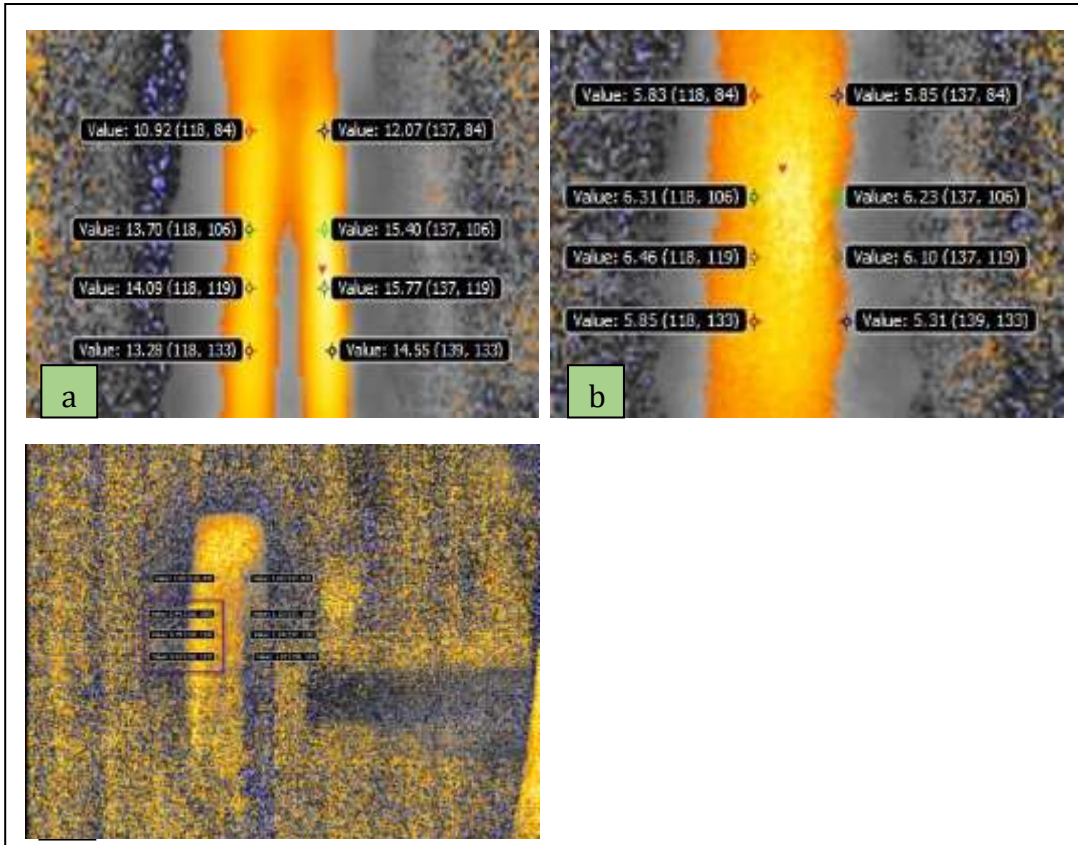


Figure 81: Processing the data using the proposed algorithm (corroded wire on the left)

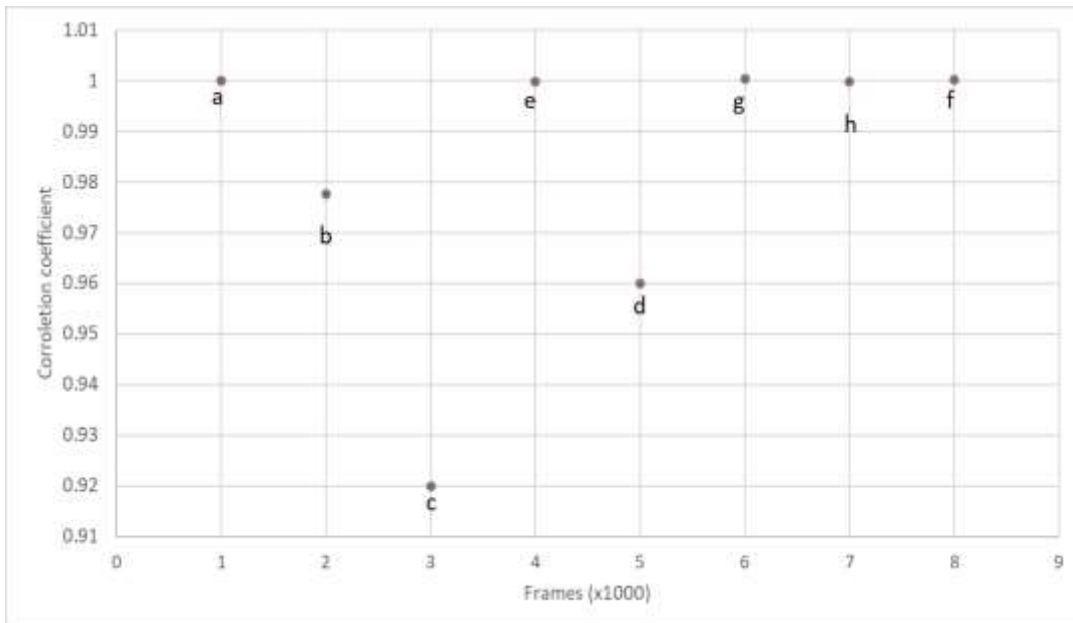


Figure 80: Correlation coefficient associated with the acquisition points on sample 8

4.4.5. DETECTION ON EMBEDDED TRINGLES

Tringles corroded in tap water

Detection of corrosion on tringles is a more complex task than the detection of corrosion on a single steel wire as tringles are formed by braiding 120 steel wires together. To add to the complexity of the task, is the thick layer of the rubber envelope above the tringles. For this set of experiments, the heating regimen mentioned previously was employed. The thermal camera parameters were kept the same. At first seven acquisition points were placed randomly on the embedded tringle and suspect points were identified according to the procedure mentioned earlier. Three points were identified and are marked with three red arrows. Figure 82 (a) and (b) show the sample being processed with a simple temperature algorithm. It can be seen that the temperature does not give any indication of where corrosion might be on the tringle. Using the algorithm that was developed for this work, we can see that the two of the suspected points assume the lowest temperatures indicating that corrosion is present in these areas. Unfortunately, the third point is a false positive and that might be due to the irregular shape of the tringles as some corrosion might be located between or underneath some wires. This is definitely problematic in this case, but might not be as problematic when it comes to inspecting tires in use as most corrosion on the tringles should be on the surface only.

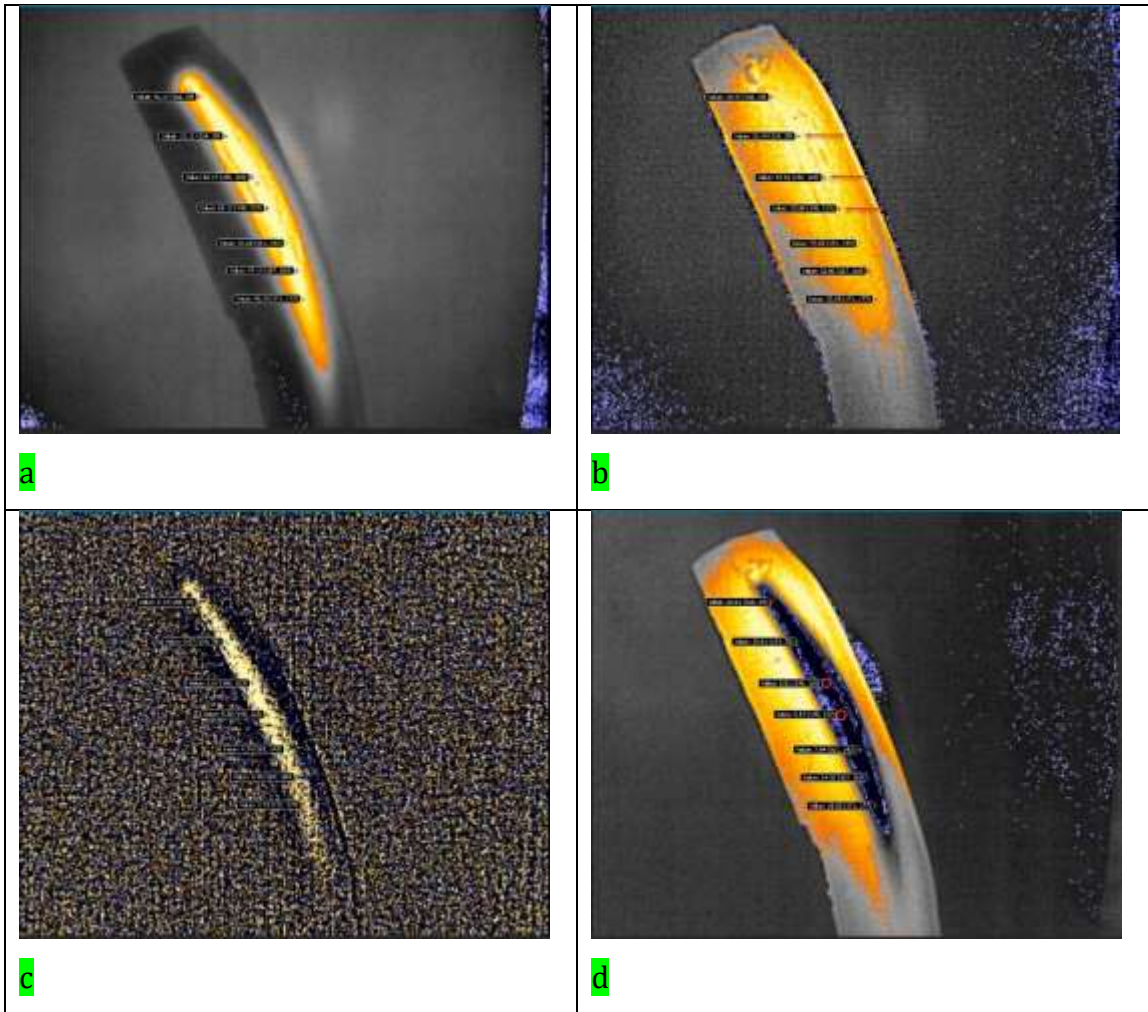


Figure 82: Embedded tringle, corroded in tap water (a) right after heating, (b) After 500s cooling processed with FLIR algorithm, (c) right after heating, (d) After 500s cooling processed by the in-house algorithm.

Tringle corroded in a saline solution

For this set of experiments, the heating regimen mentioned previously was employed. The thermal camera parameters were kept the same. At first seven acquisition points were placed randomly on the embedded tringle and suspect point were identified according to the procedure mentioned earlier. Three points were identified and are marked with three red arrows. Figure 83 (a) and (b) show the sample being processed with a simple temperature algorithm. It can be seen that the temperature does not give any indication of where corrosion might be on the tringle and the flagged points did not have the highest temperature overall. Using the

algorithm that was developed for this work, we can see that one point of the suspected points assume the lowest temperatures indicating that corrosion is present in this area. The false positives here might have been caused by some salt crystals precipitating between wires and absorbing some of the signal generated.

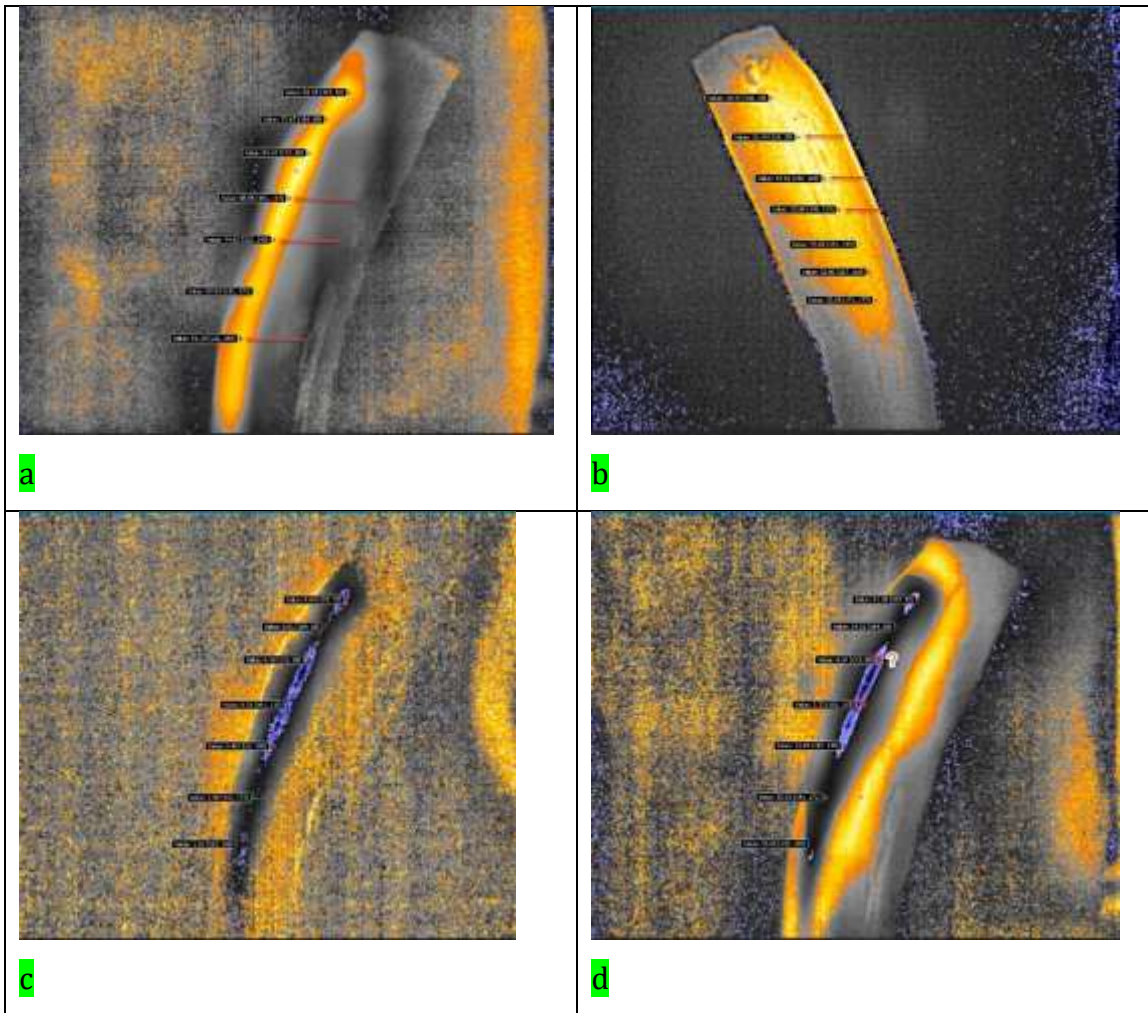


Figure 83: Embedded tringle, corroded in saline solution (a) right after heating, (b) After 500s cooling processed with FLIR algorithm, (c) right after heating, (d) After 500s cooling processed by the in-house algorithm.

CHAPTER 5

CONCLUSION

5.1. CONCLUSIONS

- Terahertz (far-infrared) radiation was not successful in detecting corrosion due to the radiation absorption from the black carbon material inside automobile tires (from introduction).
- Piloting experiment, using planar inductor on corroded nails proved partial efficiency during corrosion detection. Thermal camera was able to distinguish between the corroded and pristine wires when embedded inside cooked rubber. However, the thermographic images were not successful to localize the corroded area precisely, at least for the used implemented energy.
- Experiments using the handmade Helmholtz coil, were not successful as no contrast was observed between the corroded surfaces and the pristine ones.
- Although Tesla coil showed the best performance in providing higher induction energy, more uniform heating, and more temperature difference between the pristine and corroded wire, however, results showed that using simple temperature analyzing algorithms cannot be relied upon to produce accurate results when it comes to locating corrosion in metallic objects, specially if these were heavily coated or embedded in thick insulating materials. We also showed that depending on the complexity of the object being analysed, the in-house algorithm gave promising results at pinpointing areas where corrosion occurred. In general, the correlation coefficient was a good indicator of where corrosion might be present. However, the algorithm produced some false positives when the geometry of the object became more complex, or some precipitate might have formed. Nonetheless, the algorithm was able to show where corrosion

occurred in most cases. More studies must be conducted in order to better optimize the image processing step as well the amount of data acquired.

- Negligible to no difference was spotted between the zinc-on and zinc off pattern samples.

5.2. RECOMMENDATIONS

1. The use of a better thermal camera as the algorithm is as good as the data being analyzed.
2. The use of a multi resolution analysis technique that can obtain information from several domains (time and frequency combined).
3. The use of a standardized Helmholtz setup, able to provide uniform heating with higher power output.

5.3. FUTURE WORK

A pair of ring shaped-bobbin is already purchased: PASCO EM-6723A (fig. 84), and it will be used in our next experiments. We expect that this apparatus will solve heating irregularities that may occur over the sample during heating and enable the use to see the sample directly without blocking from the coil (like the case of Tesla coil). Each ring of this setup has 500-turn wire coil with a diameter of about 21 cm along with the following specifications:

Wire:	Copper, 22 AWG (0.64mm diameter)
Inner radius:	10.06 cm
Outer radius:	11.37 cm
Coil width:	1.5 cm
Body material:	Polycarbonate plastic

The coils are separated by a distance h equal to the radius R of the coil to minimize the non-uniformity of the field at the center of the coils (fig. 86). And according to Bio Savart's law, magnetic field (B) at the axis of the 2 circular coils will be:

$$B = \frac{\mu_0 N I R^2}{2} \left\{ \frac{1}{[R^2 + (z + R/2)^2]} + \frac{1}{[R^2 + (z - R/2)^2]} \right\} \quad (17)$$

Where μ_0 the free space permeability

N represents the number of loops,

I is the current intensity,

R is the bobbin diameter,

z is the distance from the midpoint of the circular coils,

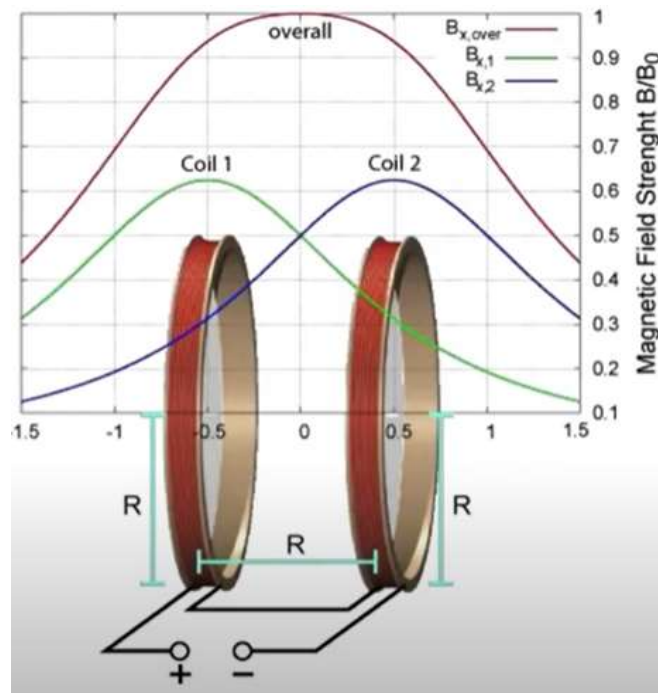


Figure 84: Magnetic field in Helmholtz setup

REFERENCES

- Ahmad, Z., 2006. Principles of corrosion engineering and corrosion control, 1st ed. ed. Elsevier/BH, Amsterdam ; Boston, Mass.
- Ashby, M.F., 2011. Material Property Charts, in: Materials Selection in Mechanical Design. Elsevier, pp. 57–96. <https://doi.org/10.1016/B978-1-85617-663-7.00004-7>
- Bagavathiappan, S., Lahiri, B.B., Saravanan, T., Philip, J., Jayakumar, T., 2013. Infrared thermography for condition monitoring – A review. *Infrared Phys. Technol.* 60, 35–55. <https://doi.org/10.1016/j.infrared.2013.03.006>
- Bertman, S., 2005. Handbook to life in ancient Mesopotamia. Oxford University Press, New York.
- Bolu, G., Gachagan, A., Pierce, G., Harvey, G., Choong, L., Thompson, D.O., Chimenti, D.E., 2010. MONITORING CRACK PROPAGATION IN TURBINE BLADES CAUSED BY THERMOSONICS. Presented at the REVIEW OF PROGRESS IN QUANTITATIVE NONDESTRUCTIVE EVALUATION VOLUME 29, Kingston (Rhode Island), pp. 1654–1661. <https://doi.org/10.1063/1.3362267>
- Burton, W., 1954. The story of tire beads and tires, First Edition. ed. McGraw-Hill.
- Carothers, W.H., 1931. Polymerization, in: *Chemical Reviews*, 8(3), Pp.353-426.
- Carlsaw, H.S., Jaeger, J.C., 1959. Conduction of heat in solids. Clarendon Press.
- de la Fuente, D., Díaz, I., Simancas, J., Chico, B., Morcillo, M., 2011. Long-term atmospheric corrosion of mild steel. *Corros. Sci.* 53, 604–617. <https://doi.org/10.1016/j.corosci.2010.10.007>
- Doshvarpassand, S., Wu, C., Wang, X., 2019. An overview of corrosion defect characterization using active infrared thermography. *Infrared Phys. Technol.* 96, 366–389. <https://doi.org/10.1016/j.infrared.2018.12.006>
- Du Cros, A., 1938. Story of the pneumatic tyre invention and industry. London, Chapman & Hall, ltd.
- Foudazi, A., Ghasr, M.T., Donnell, K.M., 2015. Characterization of Corroded Reinforced Steel Bars by Active Microwave Thermography. *IEEE Trans. Instrum. Meas.* 64, 2583–2585. <https://doi.org/10.1109/TIM.2015.2450353>
- Gent, A.N., Walter, J., 2005. The Pneumatic Tire.
- Gonzalez, R.C., Woods, R.E., Eddins, S.L., 2011. Digital image processing using MATLAB, 2. ed., 4. repr. ed. Tata McGraw Hill Education, New Delhi.
- Harris, J.R., Evans, L.R., Maclsaac Jr, J.D., 2013. Laboratory Tire Bead Unseating– Evaluation of New Equipment, Pressures and “A” Dimension From ASTM F-2663-07as. No DOT HS 811 735.
- He, Y., Tian, G.Y., Pan, M., Chen, D., Zhang, H., 2014. An investigation into eddy current pulsed thermography for detection of corrosion blister. *Corros. Sci.* 78, 1–6. <https://doi.org/10.1016/j.corosci.2013.09.001>

- Hirakawa, Y., Yasumoto, Y., Gondo, T., 2020. Evaluation of Rubber Products by Terahertz Time-domain Spectroscopy: Carbon Black Dispersion and Vulcanization State. *J. Infrared Millim. Terahertz Waves* 41, 414–429. <https://doi.org/10.1007/s10762-019-00637-6>
- Hodgins, D., 2017. Eliminate Wheel Corrosion [WWW Document]. rimex.com. URL <https://www.rimex.com/blog/wheels-rims/eliminate-wheel-corrosion>
- Ibarra-Castanedo, C., 2013. Nondestructive testing with thermography. *Eur. J. Phys.* 34(6), 91.
- Ibarra-Castanedo, C., González, D., Klein, M., Pilla, M., Vallerand, S., Maldague, X., 2004. Infrared image processing and data analysis. *Infrared Phys. Technol.* 46, 75–83. <https://doi.org/10.1016/j.infrared.2004.03.011>
- Ibarra-Castanedo, C., Piau, J.-M., Guilbert, S., Avdelidis, N.P., Genest, M., Bendada, A., Maldague, X.P.V., 2009. Comparative Study of Active Thermography Techniques for the Nondestructive Evaluation of Honeycomb Structures. *Res. Nondestruct. Eval.* 20, 1–31. <https://doi.org/10.1080/09349840802366617>
- Kadhem, A., 2018. Study the effect of steel wire pre-tension on the bending and adhesion properties of bead ply in rubber tires. *Kufa J. Eng.* 9, 52–65.
- Kovac, F.J., Rodgers, M.B., 1994. Tire Engineering, in: *Science and Technology of Rubber*. Elsevier, pp. 675–718. <https://doi.org/10.1016/B978-0-08-051667-7.50019-6>
- Lau, S.K., Almond, D.P., Milne, J.M., 1991. A quantitative analysis of pulsed video thermography. *NDT E Int.* 24, 195–202. [https://doi.org/10.1016/0963-8695\(91\)90267-7](https://doi.org/10.1016/0963-8695(91)90267-7)
- Li, T., Almond, D.P., Rees, D.A.S., Weekes, B., Pickering, S.G., Thompson, D.O., Chimenti, D.E., 2010. PULSED LASER SPOT IMAGING THERMOGRAPHY, MODELLING AND EXPERIMENTAL DATA. Presented at the REVIEW OF PROGRESS IN QUANTITATIVE NONDESTRUCTIVE EVALUATION VOLUME 29, Kingston (Rhode Island), pp. 435–442. <https://doi.org/10.1063/1.3362426>
- Liu, J., Ren, W., Tian, G.Y., Gao, B., Wang, Y., Zhang, J., Shaw, B., Yin, A., King-Alale, N.O., 2015. Nondestructive Evaluation of Early Contact Fatigue Using Eddy Current Pulsed Thermography. *IEEE Sens. J.* 15, 4409–4419. <https://doi.org/10.1109/JSEN.2015.2416394>
- Maldague, X., 2001. *Theory and practice of infrared technology for nondestructive testing*.
- Meinlschmidt, P., 2005. Meinlschmidt P. Thermographic detection of defects in wood and wood-based materials. Presented at the 14th international Symposium of non-destructive testing of wood., Hannover, Germany.
- Meinlschmidt, P., Aderhold, J., 2006. Thermographic Inspection of Rotor Blades. Fraunhofer-Inst. Wood Res. WKI.

- Meola, C., 2012. Infrared thermography recent advances and future trends. Bentham Science Publishers.
- Netzelmann, U., Walle, G., Ehlen, A., Lugin, S., Finckbohner, M., Bessert, S., 2016. NDT of railway components using induction thermography. Presented at the 42ND ANNUAL REVIEW OF PROGRESS IN QUANTITATIVE NONDESTRUCTIVE EVALUATION: Incorporating the 6th European-American Workshop on Reliability of NDE, Minneapolis, Minnesota, p. 150001. <https://doi.org/10.1063/1.4940613>
- Netzelmann, U., Walle, G., Lugin, S., Ehlen, A., Bessert, S., Valeske, B., 2015. Induction thermography: principle, applications and first steps towards standardization, in: Proceedings of the 2015 Asia International Conference on Quantitative InfraRed Thermography. Presented at the Quantitative InfraRed Thermography Asia 2015, QIRT Council. <https://doi.org/10.21611/qirt.2015.0152>
- Oswald-Tranta, B., 2004. Thermoinductive investigations of magnetic materials for surface cracks. *Quant. InfraRed Thermogr. J.* 1, 33–46. <https://doi.org/10.3166/qirt.1.33-46>
- Parker, W.J., Jenkins, R.J., Butler, C.P., Abbott, G.L., 1961. Flash Method of Determining Thermal Diffusivity, Heat Capacity, and Thermal Conductivity. *J. Appl. Phys.* 32, 1679–1684. <https://doi.org/10.1063/1.1728417>
- Pieper, D., Donnell, K.M., Ghasr, M.T., Kinzel, E.C., 2014. Integration of microwave and thermographic NDT methods for corrosion detection. Presented at the 40TH ANNUAL REVIEW OF PROGRESS IN QUANTITATIVE NONDESTRUCTIVE EVALUATION: Incorporating the 10th International Conference on Barkhausen Noise and Micromagnetic Testing, Baltimore, Maryland, USA, pp. 1560–1567. <https://doi.org/10.1063/1.4865009>
- Riegert, G., Zweschper, T., Busse, G., 2004. Lockin thermography with eddy current excitation. *Quant. InfraRed Thermogr. J.* 1, 21–32. <https://doi.org/10.3166/qirt.1.21-32>
- Russ, J.C., Neal. Brent F, 2017. The image processing handbook.
- Shuohan, M., Qishuang, M., Xinbo, L., 2013. Applications of chirp z transform and multiple modulation zoom spectrum to pulse phase thermography inspection. *NDT E Int.* 54, 1–8. <https://doi.org/10.1016/j.ndteint.2012.11.006>
- Sziraki, L., 2001. Study of the initial stage of white rust formation on zinc single crystal by EIS, STM/AFM and SEM/EDS techniques. *Electrochimica Acta* 46, 3743–3754. [https://doi.org/10.1016/S0013-4686\(01\)00656-9](https://doi.org/10.1016/S0013-4686(01)00656-9)
- Tian, G., Gao, Y., Li, K., Wang, Y., Gao, B., He, Y., 2016. Eddy Current Pulsed Thermography with Different Excitation Configurations for Metallic Material and Defect Characterization. *Sensors* 16, 843. <https://doi.org/10.3390/s16060843>

- Usamentiaga, R., Venegas, P., Guerediaga, J., Vega, L., Molleda, J., Bulnes, F., 2014. Infrared Thermography for Temperature Measurement and Non-Destructive Testing. *Sensors* 14, 12305–12348. <https://doi.org/10.3390/s140712305>
- Vavilov, V., Grinzato, E., Bison, P.G., Marinetti, S., Bales, M.J., 1996. Surface transient temperature inversion for hidden corrosion characterisation: theory and applications. *Int. J. Heat Mass Transf.* 39, 355–371. [https://doi.org/10.1016/0017-9310\(95\)00126-T](https://doi.org/10.1016/0017-9310(95)00126-T)
- Wilson, J., Tian, G., Mukriz, I., Almond, D., 2011. PEC thermography for imaging multiple cracks from rolling contact fatigue. *NDT E Int.* 44, 505–512. <https://doi.org/10.1016/j.ndteint.2011.05.004>
- Wu, J., Zhou, D., Wang, J., 2014. Surface Crack Detection for Carbon Fiber Reinforced Plastic Materials Using Pulsed Eddy Current Based on Rectangular Differential Probe. *J. Sens.* 2014, 1–8. <https://doi.org/10.1155/2014/727269>
- Xu, Z., Zhu, Y., Ma, H., Duan, Y., Yang, C., Song, D., 2020. Research on the Technology of Conductor Corrosion Detection based on Eddy Current Testing. *IOP Conf. Ser. Earth Environ. Sci.* 446, 022073. <https://doi.org/10.1088/1755-1315/446/2/022073>
- Zenzinger, G., 2007. Thermographic crack detection by eddy current excitation. *Nondestruct. Test. Eval.* 22, 2007, 101–111.
- Zhang, X.G., Xing, A., 2004. Galvanic action of zinc-coated steel-fundamentals and practical applications. *Galvatech* 4.

APPENDIX B

Matlab codes for image processing

Image segmentation and clustering:

```
clear,clc,close all
%%%%%%%%%%%%%%%%%%%%%%%%%%%%%%%%%%%%%%%%%%%%%%%%%%%%%%%%%%%%%%%%%%%%%%%%
K = 8; % Number of clusters %%
%%%%%%%%%%%%%%%%%%%%%%%%%%%%%%%%%%%%%%%%%%%%%%%%%%%%%%%%%%%%%%%%%%%%%%%%

CH = menu('Choose the region of analysis','ALL image','Bounding box');
% Obtain an input image.
[filename,pathname] = uigetfile('*.');
im = imread([pathname,filename]);

% set the image size to suitable value
scale = 600/(max(size(im)));
im = imresize(im,scale*size(im(:,:,1)));

% set region of interest
if CH==1
    rect=[1,1,size(im,2)-1,size(im,1)-1];
elseif CH==2
    figure(),imshow(im)
    rect = ceil(getrect());
    close
end

% Make ROI mask
ROI = false(size(im(:,:,1)));
ROI(rect(2):rect(2)+rect(4),...
    rect(1):rect(1)+rect(3)) = true;

% Apply K-means clustering
[L,C_RGB] = Kmeans_img_clust(im,K,ROI);

% Show results
figure('Position',[168,182,1625,744])
subplot(1,2,1),imshow(im)
title('Original image')

% Show each cluster color
leg = {}; hold on
for i=1:K
    Col = (C_RGB(i,:))./255;
    leg(i,:)={'Cluster ',num2str(i)};
    plot(1,1,'LineWidth',12,'Color',Col)
end
legend(leg,'FontSize',12);hold off

subplot(1,2,2),imshow(L,[])
```

```
title('Segmentation clusters')
```

```
function [L,C_RGB] = Kmeans_img_clust(img,K,mask)
% This function cluster the image using Kmeans clustering
% to K+1 clusters where the pixels outside the mask
% are set to zeros and rest are clustered from 1 to K
```

```
if length(size(img))==3
    X = [reshape(img(:,:,1),[],1),...
         reshape(img(:,:,2),[],1),...
         reshape(img(:,:,3),[],1)];
```

```
else
    X = reshape(img(:,:,1),[],1);
end
```

```
mask = reshape(mask,[],1); X2 = X(mask,:);
[Clust,C] = kmeans(double(X2),K,'Replicates',5);
C_RGB = round(C);
idx = double(mask); idx2 = find(idx);
```

```
for i=1:length(idx2)
    idx(idx2(i)) = Clust(i);
end
```

```
L = reshape(idx,size(img,1),size(img,2));
```

Image analysis and processing:

```
function varargout = Thermal_image(varargin)
% Initialization code - DO NOT EDIT
gui_Singleton = 1;
gui_State = struct('gui_Name',       mfilename, ...
                  'gui_Singleton',  gui_Singleton, ...
                  'gui_OpeningFcn', @Thermal_image_OpeningFcn, ...
                  'gui_OutputFcn',  @Thermal_image_OutputFcn, ...
                  'gui_LayoutFcn',  [], ...
                  'gui_Callback',   []);
```

```
if nargin && ischar(varargin{1})
    gui_State.gui_Callback = str2func(varargin{1});
end
```

```
if nargin
    [varargout{1:nargout}] = gui_mainfcn(gui_State, varargin{:});
else
    gui_mainfcn(gui_State, varargin{:});
end
```

```
% End initialization code - DO NOT EDIT
```

```
% --- Executes just before Thermal_image is made visible.
```

```
function Thermal_image_OpeningFcn(hObject, eventdata, handles, varargin)
```

```
handles.output = hObject;
```

```
guidata(hObject, handles);
```

```
function varargout = Thermal_image_OutputFcn(hObject, eventdata, handles)
```

```

varargout{1} = handles.output;

% --- Executes on button press in pushbutton1 (Load thermal image)
function pushbutton1_Callback(hObject, eventdata, handles)
global R G B range img unit
% Ask user to load input image. The input
% image must contain thermal image to analyse
% and a colormap to map temprature range
[File,Path] = uigetfile({'*.jpg;*.tif;*.png;*.gif'},...
    'Select image to analyse');
img = imread([Path File]);
f = figure() ;imshow(img); %Showing loaded image
set(f,'Position',[60 60 1200 600]); % Zooming image
title('Select the colormap','FontSize',15)
rect = getrect; %Select the color map in image
Cmap=imcrop(img,rect); % Saving color map in another image
title('Select the analysis area','FontSize',15)
rect = getrect; %Select the area to analyse in image
img=imcrop(img,rect); % Cropping image to analysis area

% Ask user for temp range
prompt = {'Colormap Max end:','Colormap Min end:','Unit:'};
answer = inputdlg(prompt,'Input',[1 50]);
range(1) = str2double(cell2mat(answer(1)));
range(2) = str2double(cell2mat(answer(2)));
unit = cell2mat(answer(3));
close(f);axes(handles.axes1)
imshow(img); %Updating loaded image

% Extract data from images
idx = fix(size(Cmap,2)/2);
R = Cmap(2:end-1,idx,1); %Range of red color
G = Cmap(2:end-1,idx,2); %Range of green color
B = Cmap(2:end-1,idx,3); %Range of blue color

% --- Executes on button press in pushbutton2 (Get temp at point)
function pushbutton2_Callback(hObject, eventdata, handles)
global R G B range img unit
[col,row] = ginput(1); % Get point position from user
col = fix(col); row = fix(row);
% Create temperature as function in RGB
T = linspace(range(1),range(2),length(R)); T = T';
r = img(row,col,1); % Red component of selected point
g = img(row,col,2); % Green component of selected point
b = img(row,col,3); % Blue component of selected point
%Looking for the closest point on the colormap
for tol = 1:length(R);
idx=((R<r+tol)&(R>r-tol))&((G<g+tol)&(G>g-tol))&((B<b+tol)&(B>b-tol));
t = T(idx);
if ~isempty(t),break,end
end
t=mean(t); % Calculated temperature
imshow(img),hold on,plot(col,row,'*b'),hold off %Show point
title(['Temperature = ',num2str(t),' ^o',unit],'FontSize',15); %show result

```

```

% --- Executes on button press in pushbutton3 (Get HotSpot)
function pushbutton3_Callback(hObject, eventdata, handles)
global R G B range img unit
S = size(img); n = S(1)*S(2);
t=zeros(S(1),S(2)); %Preallocation teperature matrix
% Create temperature as function in RGB
T = linspace(range(1),range(2),length(R)); T = T';
WB = waitbar(0,'Processing image ....');
count = 0;
for row=1:S(1)% Scan point position
    for col=1:S(2)
        r = img(row,col,1); % Red component of selected point
        g = img(row,col,2); % Green component of selected point
        b = img(row,col,3); % Blue component of selected point
        %Looking for the closest point on the colormap
        for tol = 1:length(R);
            idx=((R<r+tol)&(R>r-tol))&((G<g+tol)&(G>g-tol))&((B<b+tol)&(B>b-
tol));
            tmp = T(idx);
            if ~isempty(tmp),break,end
        end
        t(row,col)=mean(tmp); % Calculated temperature
        count=count+1; waitbar(count/n,WB);
    end
end
th = 0.95*max(T); %Threhold temp for a part to be hotspot
[row,col] = find(t>th); temp=mean(mean(t(row,col)));
close(WB); % End of analysis
imshow(img),hold on %Show hotspot area
plot(col,row,'g.'),hold off
title(['Temperature = ',num2str(temp),' ^o',unit],'FontSize',15); %show result

```